THE UNIVERSITY OF CALGARY

G55.0+0.3 – An Ancient Supernova Remnant?

by

Brenda C. Matthews

A THESIS

SUBMITTED TO THE FACULTY OF GRADUATE STUDIES

IN PARTIAL FULFILLMENT OF THE REQUIREMENTS FOR THE

DEGREE OF MASTER OF SCIENCE

DEPARTMENT OF PHYSICS AND ASTRONOMY

CALGARY, ALBERTA

August, 1996

THE UNIVERSITY OF CALGARY
FACULTY OF GRADUATE STUDIES

The undersigned certify that they have read, and recommend to the Faculty of Graduate Studies for acceptance, a thesis entitled, "G55.0+0.3 – An Ancient Supernova Remnant?" submitted by Brenda C. Matthews in partial fulfillment of the requirements for the degree of Master of Science.

Chairman, Dr. A. R. Taylor
Department of Physics and Astronomy

Dr. D. Leahy
Department of Physics and Astronomy

Dr. R. B. Hicks
Department of Physics and Astronomy

Dr. G. Lachapelle
Department of Geomatics Engineering

Date ______________________

Abstract

In order to determine the nature of an object identified as a potential supernova remnant in a 327MHz survey of the Galactic plane, continuum data have been taken at 1420MHz with identical resolution to that of the survey. Additionally, HI spectral line data have been taken in order to determine the distance to the object.

Multifrequency analysis shows that a shell feature in the southern part of this object is nonthermal and confirms earlier studies that identified the northern portion as an HII region. The nonthermal nature of the shell and the absence of infrared flux density confirms the speculation of Taylor *et al.* (1992) that this object, G55.0+0.3, is a supernova remnant (SNR). From analysis of atomic hydrogen, its estimated distance is 14kpc, yielding a radius of 62pc. This makes it one of the largest known of this class of objects. Additionally, an age estimate of one million years exceeds the conventional limits in the literature by a factor of five. There also exists compelling evidence that the remnant could in fact be associated with the nearby pulsar, J1932+2020.

The discovery of G55.0+0.3 implies that the radiative lifetimes of SNR could be much longer than previously suggested. The proposed pulsar/SNR association is older than any previously documented by an order of magnitude. If valid, it suggests that searches for associations should not be restricted to the regions about young pulsars.

Acknowledgements

Credit for the final form of this thesis must be shared with several people. My supervisor, Russ Taylor, is owed immense gratitude, both for helpful guidance in the research process and for providing a calming influence when things became somewhat overwhelming. Brad Wallace, my "pseudo-supervisor", has provided invaluable input and feedback throughout the stages of the project; as well as being the speediest reference guide in the West!

More to the point of the actual production of this document, thanks go to Glen Young, who efficiently handled software glitches before and during the writing process, and Leah Hannis, who produced some of the lovely drawings within these pages.

Finally, thanks go to J. Caswell and J. Crovisier for the use of their images, to C. Heiles and H. Wendker for their helpful insight into stellar wind bubbles and to S. Tereby for her assistance with HiRes information.

Dedication

To my parents, Bill and Dolores, for their help and encouragement and their belief in the immeasurable value of education.

Also to my grandparents, Elmer and Lucienne Matthews and William O'Connor, for their friendship, wisdom and support,

and to the memory of Colleen O'Connor.

Contents

List of Tables

List of Figures

Chapter 1

On the Nature and Identification of Supernova Remnants

1.1 The Milky Way

Almost everyone is familiar with the bright band of emission which reaches across the northern sky in the summer months. Today we know that bright nebula is the light of the billions of stars which comprise our Galaxy, the Milky Way. Our Sun is located in one of the spiral arms of the Milky Way and, at 8.5 kiloparsecs (1 parsec (pc) = 3×10^{18}cm), is quite distant from the centre of the Galaxy. The features of our Galaxy are revealed by the distribution of stars: its central bulge and the flattened disk in which the spiral arms reside. The basic structure of a spiral galaxy is shown in Figure 1.1.

The emission we see as we look up at night is limited to the frequencies of electromagnetic (EM) radiation to which our eyes are sensitive. In fact these wavelengths (400nm to 700nm) are a very narrow window of the EM spectrum (referred to as the visual or, more commonly, the optical by astronomers). Were we able to see in other regimes of the spectrum, some of the objects with which we are so familiar would cease to be apparent, but would be replaced with others of different, yet equally fascinating composition.

Let us imagine that we have a powerful telescope which is capable of detecting

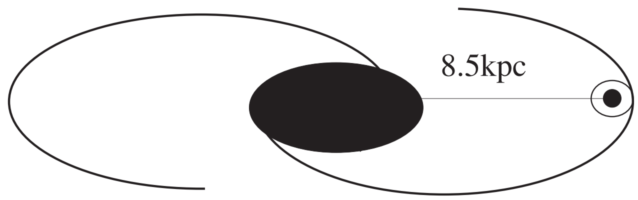

Figure 1.1: **Schematic of the Components of our Galaxy**
Our galaxy is a typical spiral with a central bulge and spiral arms which lie in a plane. It has a radius of ~25kpc from the centre to the edge of its optical emission. The symbol ⊙ indicates the Sun on the Local Arm, 8.5kpc from the Galactic centre. There are spiral arm structures at greater radii than the Local Arm; they are not shown here for simplicity. Galactic latitudes and longitudes are measured with respect to the plane of the Galaxy and the line of sight from the Sun to the Galactic centre, respectively.

radiation at any wavelength. We set our telescope on the moon to get above the Earth's atmosphere and avoid EM emission from the Earth.

Our telescope is set to observe the optical regime as a default, so as we first look toward the Galactic plane, we are able to distinguish stars as well as brilliantly coloured nebulae composed primarily of hydrogen gas. These nebulae may contain young stars which ionize their atomic surroundings (creating HII regions) and dissociate molecular surroundings due to their emission of UV photons.

These diffuse clouds are a component of the *interstellar medium* (ISM) which is the collective term for the medium between the stars. This medium contains regions of different temperature, density and composition which are thought to be in rough pressure equilibrium (McKee and Ostriker, 1977). There are five basic material components of the ISM: *molecular, neutral atomic, ionized, dust* and *relativistic plasma.*

The bright emission of the Galactic plane is partially obscured by dark bands which stretch across it. These lanes indicate the presence of dust, particulate matter which is intermixed with gaseous ISM and acts to absorb any emission generated behind it. The dust has total mass of only 1% that of the gas.

As we enter the next regime, the infrared (IR), the emission we see is primarily from the dust distributed throughout space. The concentrations of dust which were absorbing in the optical become emitting, and thus the emission from the direction of the Galactic plane remains pronounced. Dust may be heated by ionizing photons of various energies, but typically radiates the energy away in the IR. Therefore, HII regions may still appear bright due to the heating of surrounding dust by many hot stars within.

Next, we set our telescope to receive wavelengths within the radio regime. Since the radio extends over a broad wavelength range, from centimetre to several metre wavelengths (or GHz to MHz frequencies), the objects visible within its boundaries will not typically be visible over the whole range of wavelengths. The emission from material within the Galactic plane is still strong. At 21cm, radiation from the spin transition of the hydrogen atom's electron is visible, giving a measure of the neutral atomic medium. Classes of objects which populate the ISM in the radio include HII regions, stellar wind bubbles, and the remnants of stellar explosions, called supernovae.

Finally, we decide to alter our telescope from the detection of the low energy radio photons to that of much higher energy photons–those of the X-ray regime. This radical change leaves us a little disoriented, though not as much as we expect despite the increase in energy of roughly a billion times between the two regimes. In fact, some of the supernova remnants (SNR) which were visible in the radio, such as Cassiopeia A, one of the brightest radio sources in the sky about 1GHz, is also extremely bright in the X-ray and has virtually the same morphology. The photons received from X-ray sources are high in energy but few in number and essentially tell us about the "hot spots" in the Galaxy. Thus, as we gaze into the X-ray sky, we see emission surrounding suspected black holes (via the hot gas within their accretion disks), the centres of other galaxies and the shocked gas created in the aftermath of supernovae.

1.2 The Birth of Supernova Remnants and Pulsars

Two types of radio objects are created by the same event: the cataclysmic disruption of a star. Pulsars and SNR are the remains of such events and can be observable (at least in the case of pulsars) for millions of years (Taylor and Stinebring, 1986; Backer, 1988). The explosive events that create these objects are called supernovae (SNe).

1.2.1 Supernovae

Our contemporary concept of SNe as the end of life of massive stars was not put forth until 1934 when Baade and Zwicky assembled the ideas of various astronomers, even speculating that a superdense stellar core could be created by such a phenomenon (1934a,b).

As more SNe are observed, their mechanics are becoming better understood. It became apparent very early in their study that spectral signatures (presence or absence of hydrogen lines) indicated that there are several classes of supernovae (Minkowski, 1941). These are generally divisible into three basic groups:

- **Type Ia** These contain no hydrogen lines in their spectra, but strong lines of silicon are present. These are observed in both spiral and elliptical galaxies, which has led to the speculation that these SNe are associated with old, low mass stars found in both galaxy types.
- **Type 1b** The spectra contain no hydrogen lines, but strong lines of helium are present. These are believed to result from the explosion of massive stars which have had their hydrogen envelopes depleted.
- **Type II** Hydrogen lines are present in the spectra. These SNe are observed in spiral and irregular galaxies, which implies that they are related to the young, bright stars known to reside there.

Despite early notions about SNe, Type Ia SNe do not result from the explosions of massive stars. Instead, they occur in binary systems containing one normal star and a stellar remnant called a white dwarf. A white dwarf is a remnant of a star which had insufficient mass to produce a SN.

A white dwarf is supported by the pressure of a degenerate electron gas. However, there is a theoretical mass limit beyond which it is impossible for a white dwarf to maintain itself against collapse under its own gravity. This is called the Chandrasekhar limit and is equal to $1.4 M_{\odot}$ (many astronomical quantities are expressed in solar units; any references with the symbol $\odot$ denote solar values). In a binary system, accretion of material from the second star onto the white dwarf can increase its mass beyond the Chandrasekhar limit, resulting in a SN which destroys the star.

Type Ib and II SNe are the deaths of massive stars ($> 8M_\odot$). These stars are able to sustain fusion in their cores to elements of higher atomic number than stars which create white dwarfs. However, no star can sustain fusion indefinitely since the process is endothermic for elements of atomic numbers greater than that of iron. Whenever the point is reached at which the star can no longer produce energy by fusion within its core, then the star will collapse under gravitational pressure. Its high mass (since the core mass $> 1.4M_\odot$) means that the collapse will not be halted by the pressure of degenerate electrons. The collapse is aided by the fact that protons in the core "capture" electrons, converting to neutrons and allowing the collapse to continue unhindered. Thus, the core becomes a *neutron star*.

It is through the electron capturing process that a large flux of neutrinos is released (Lang, 1980). It is believed that the neutrinos carry away most of the binding energy of the core, leading to the release of $\sim 10^{53}$ erg of energy (Helfand and Becker, 1984). About 1% of the energy is converted to kinetic energy in the form of ejection of the outer envelope of the star at speeds on the order of thousands of kilometres per second. This leaves the stellar remnant (a neutron star of mass $1.4\mathrm{M}_\odot$ or perhaps a black hole) surrounded by a rapidly expanding envelope of ejecta.

1.2.2 Pulsars

Pulsars are neutron stars which are born with initial spin periods and magnetic fields such that the radiation they emit is detectable to us. The term *pulsar* stands for *pulsating radio source*. Their emission takes the form of extremely regular pulses.

The source of the radiation from pulsars is synchrotron radiation (see §1.2.4) emitted from charged particles which are accelerated along the powerful magnetic field lines of the star (typical surface fields are $\sim 10^{12}$ Gauss (Backer, 1988)). The radiation is beamed along the particles' direction of motion meaning that only pulsars which have magnetic poles directed toward Earth are visible to us.

Since the magnetic and rotation poles are offset from one another, the beam of radiation sweeps out a cone as the star rotates, resulting in pulsation in the received radiation. This phenomenon is often described as the "lighthouse" model of pulsars.

Pulsar periods can range from milliseconds to seconds, and it is believed that their periods increase over time. This "spindown" occurs through the loss of kinetic energy via low-frequency EM waves or high-energy particles and radiation (Lyne, 1995). The pulsar slowdown will be discussed in some detail, as it is relevant to how pulsar ages are calculated.

For a general gradual slowdown, it is assumed that the braking torque obeys a power law in n such that

$$\dot{\Omega} = -q\Omega^n \tag{1.1}$$

where Ω is the rotational frequency of the pulsar at some time t, q is a constant and n is called the *braking index* and is positive and greater than unity. Switching from rotational frequency to periods, equation 1.1 becomes

$$\dot{P} = q' P^{2-n} \tag{1.2}$$

where q' is a new constant and P is the period of rotation, $P = 2\pi/\Omega$. Integration of equation 1.2 yields a time of

$$t = \frac{P}{(n-1)\dot{P}}\left[1 - \left(\frac{P_0}{P}\right)^{n-1}\right] \tag{1.3}$$

for the time interval since the pulsar had an initial period P_0. Equation 1.3 is used to define a *characteristic age* for the pulsar under the assumptions that $P_0 \ll P$ and

$n = 3$. The characteristic age is given by

$$t_c = \frac{P}{2\dot{P}}. \tag{1.4}$$

Selecting a value of n to be 3 is not completely arbitrary, since it is the value for magnetic braking in a dipole field (Lyne, 1995), and it is also that which would be expected for a completely aligned rotator (Goldreich and Julian, 1969). Of greater concern is the assumption that $P_0 \ll P$. Acknowledging this assumption, the characteristic age can be regarded as an upper limit to a pulsar's age. The degree of overestimation decreases as the pulsar ages. Also, equation 1.4 tacitly assumes that the magnetic field of the pulsar remains constant. If there is decay in the field, this would also serve to overestimate the true age of the pulsar (Lyne, 1995).

The value of n can be independently measured if the second derivative of the period can be measured. This has been done for only three pulsars and has yielded values between 2 (PSR 0540-69) and 2.84 (PSR 1509-58) with uncertainties of no greater than 1%. The discrepancy between these values and the theoretical value of 3 is attributed either to the fact that the magnetic field is not a true dipole or to the presence of particles in the magnetosphere (Lyne, 1995).

The best method of determining the distance to most pulsars is via their *dispersion measure*, DM, typically measured in pc cm^{-3}. This is a measure of how much delay there is between the arrival times of pulses at different wavelengths due to dispersive electrons in the ISM. It makes pulsars an effective tool for the probing of the structure of the ISM, since the DM is related to the column density of electrons, $n_e(l)$, in cm^{-3} between the pulsar and the observer, such that:

$$DM = \int_0^d n_e(l)dl \tag{1.5}$$

where dl is a unit length along the line of sight, and the pulsar is at the distance d in parsecs.

Thus, *if* the mean electron density, $< n_e >$, is known, then the distance to the pulsar can be calculated:

$$d = \frac{DM}{< n_e >}. \tag{1.6}$$

or vice versa. There are, however, a variety of estimates as to the mean density distributions of electrons in the Galaxy (Taylor and Cordes, 1993; Cordes, 1986), and distances derived in this fashion have large uncertainty.

1.2.3 Supernova Remnants

The death throes of massive stars leave gaseous remains of the envelope of the progenitor star which expand outward at high velocity. As the ejecta expands and interacts with the ISM, radiation is produced which makes the *supernova remnant* observable. SNR are important since it is through them that the energy of a SN is transferred to the ISM. Indeed, aside from the energy input of the stellar winds of hot O type stars, SNe are the fundamental source of energization of the ISM (Kulkarni and Heiles, 1988).

There are three basic categories of radio SNR. These are:

- **filled-centre remnants (plerions)** which have a centrally brightened structure. The prototype is the Crab Nebula. It is assumed that these amorphous objects are powered by a central pulsar, even if it is not visible;

- **shell-type remnants** which do not show a central brightening, although a pulsar may be present. These SNRs have a limb-brightened, ring-shaped appearance, although they can be deformed by interactions with the ISM; and

- **composite remnants** which show a dual structure as their name suggests, and exhibit features of both plerionic and shell-type remnants.

X-ray and optical properties lead to different classifications. For example, shell-type SNR in the radio can be centrally enhanced X-ray emitters.

Plerions comprise only about 5% of established SNR (Green, 1995). By far, the vast majority of SNR are shell-type (~75%), while the composites represent ~10%. The remainder are uncategorized.

The identification of an object as an SNR has typically been based on its radio properties. Generally, it has sufficed that an object have a nonthermal spectrum (described in §1.2.4), show a significant degree of polarization and show a shell-like or centrally brightened shape to be classified as an SNR. Typically, the radiation from shell-type remnants exhibits degrees of polarization between 5 and 15%, although higher values are common in plerionic remnants (Reynolds, 1988). However, in categorizing radio sources in the Galaxy, one must be cautious since an object that meets only some of these observational criteria need not be an SNR (Woltjer, 1972). Massive stars with powerful winds can blow holes in the ISM, creating shell-like structures similar to those expected for SNR. Also, HII regions may appear as extended objects in the radio and can have ring-like structure. However, they do not generally emit polarized radiation and their spectra reveal them to be thermal objects. Additionally, infrared data from the IRAS satellite have revealed that mean IR to radio flux density ratios differ between HII regions and SNR, with values for shell-type SNR typically less than 100 while HII regions can have ratios as high as 1000 (Fürst *et al.*, 1987; Wallace, 1991).

The presence of nonthermal emission as a distinguishing characteristic of SNR has been mentioned without explaining what is meant by nonthermal. The next two sections discuss both the origin of this emission and how it is detected observationally.

1.2.4 Synchrotron Radiation

Synchrotron radiation is the name given to radiation emitted by relativistic charged particles when they encounter a magnetic field. The particles spiral along the magnetic field lines, radiating energy which can span the EM spectrum, from X-ray to radio regimes. If the field in which the particles exist is uniform then all the radiation is emitted in a similar plane of polarization and the total flux density has a net polarization. An astronomical source that emits synchrotron radiation is referred to as a “nonthermal” source.

The first SNR speculated to be emitting synchrotron radiation was the Crab nebula. The optical radiation was proposed to be nonthermal and polarized (Ginzburg, 1953; Shkovski, 1953; Gordon, 1954). The observational confirmation by Dombrovski (1954) in the optical and then Oört and Walraven (1956) in the radio clearly indicated that astrophysical sources could emit synchrotron radiation. The source powering the Crab's synchrotron emission, the pulsar 0531+21, was not discovered until 1968 (Staelin and Reifenstein, 1968).

Models of synchrotron emission from astrophysical sources generally consider only electrons (and positrons). This assumption is reasonable since electrons reach relativistic speeds at lower energies than protons and for a given energy will always be more relativistic. Also, since the power emitted at a synchrotron source is inversely proportional to the fourth power of the mass of the emitting particle, the received power from electrons will exceed that of protons by a factor of order 10^{16}! The emitted power per charged particle has the form:

$$P = \frac{2e^4}{3c^7 m_e^4} E^2 \beta^2 (B \sin\theta)^2 \tag{1.7}$$

which shows the dependence on the particle's total relativistic energy, E, the magnetic field magnitude, B, and the angle θ between the velocity vector of the particle and the direction of the magnetic field. β is the ratio of the particle's speed to the speed of light, and e and m_e are the charge and mass of an electron.

Since the radiation received from astrophysical sources must come from an ensemble of particles, it is essential to develop a model which accounts for this. It is almost universally assumed (Shu, 1991; Kellerman and Owen, 1988; Lang, 1980; Rybicki and Lightman, 1979: Pacholzyck, 1970) that within astrophysical sources the number density of electrons of energy E observed obeys a power law distribution, such that:

$$N(E) = N_0 E^{-p} \tag{1.8}$$

where p is called the *particle index* of the power law and N_0 is the total number of electrons. Shu points out that this approximation is not without some justification, since the high-energy cosmic ray protons received on Earth do obey a power law distribution.

The assumption yields a *volume emission coefficient*, the power per unit frequency released per unit volume in the source, which has the following dependence on frequency, ν:

$$j_\nu \propto N_0 \nu^{(1-p)/2} (B \sin\theta)^{(1+p)/2}. \tag{1.9}$$

(Pacholczyck, 1970).

1.2.5 Spectral Indices from Thermal and Nonthermal Sources

The *spectral index* of a source is α, where

$$S_\nu \propto \nu^\alpha. \tag{1.10}$$

This of course assumes that the source's flux density[1], S_ν, can be modelled as a power law. This is not the case over the entire EM spectrum but can often be true over localized regimes.

The radiative transfer equation for the flux density of an isothermal astrophysical source assuming no background emission and no absorption between us and the source is:

$$S_\nu = B_\nu (1 - e^{-\tau_\nu}) \Omega \tag{1.11}$$

where B_ν is called the *source function*, τ_ν is the optical depth of the source material along the line of sight, ν is frequency and Ω is the solid angle of the source.

Thermal sources, such as HII regions, radiate as a result of electron-ion interactions within a Maxwellian plasma. For these sources, the source function is simply the Planck blackbody function which at radio wavelengths can be approximated as:

$$B_\nu = \frac{2k\nu^2}{c^2} T. \tag{1.12}$$

[1]The flux density is a measure of the power received per unit area *per unit frequency (or wavelength)*. The term *density* refers not to a dependence per unit volume but to spectral density. In the radio, the power received is extremely low, and the standard unit of flux density is the Jansky, 1 Jy= 10^{-26} W m^{-2} Hz^{-1} = 10^{-23} erg cm^{-2} s^{-1} Hz^{-1}.

where k is Boltzmann's constant, c is the speed of light and T is the source temperature. The extremes of spectral index values from thermal sources can be determined by examining the cases of an optically-thin and an optically-thick source. If a source is optically-thin, then $\tau_\nu \ll 1$ and the source flux density can be approximated as

$$S_\nu = B_\nu \tau_\nu \Omega. \tag{1.13}$$

The optical depth of an optically-thin emission nebula of uniform electron temperature, T_e, obeys the relation[2]

$$\tau_\nu \propto T_e^{-1.35} \nu^{-2.1} em, \tag{1.14}$$

where em is the emission measure,

$$em = \int_0^s n_e n_i ds \tag{1.15}$$

with ds an increment of length within the object along the line of sight and n_e and n_i the number densities of electrons and ions respectively. The total length of the source object is s. Based on equations 1.12, 1.13 and 1.14, the source flux density thus has the frequency dependence

$$S_\nu \propto \nu^{-0.1}. \tag{1.16}$$

The other extreme is that of an optically-thick source for which $\tau_\nu \gg 1$ and the flux density of equation 1.11 becomes

$$S_\nu = B_\nu \Omega. \tag{1.17}$$

[2]This approximation of Altenhoff *et al.* (1960) is a standard: Kulkarni and Heiles, 1988; Rohlfs, 1986; Lang, 1980.

which, for Ω independent of ν, implies that,

$$S_\nu \propto \nu^2. \tag{1.18}$$

Optical depth is a strong function of wavelength (see equation 1.14), decreasing with increasing ν. Also, equations 1.16 and 1.18 imply that there will characteristically be a turnover in spectral index at some frequency. The important conclusion is that thermal sources will have spectral indices in the range $-0.1 < \alpha < 2$.

Spectral indices are also occasionally defined in terms of *brightness temperature* instead of flux density. Brightness temperature is the temperature needed by a blackbody to produce the flux density seen at a given frequency. Its determination is accomplished by replacement of the observed flux density for the source function in equation 1.12 such that

$$T_b = \frac{S_\nu c^2}{2k\nu^2\Omega} \tag{1.19}$$

The flux density dependence of an optically-thin source as given in equation 1.16 thus implies a brightness temperature spectral index of -2.1. Similarly, a flux density dependence of +2 as given by equation 1.18 for an optically-thick source will give a brightness temperature independent of ν (as long as Ω is independent of ν). In this case, the blackbody temperature is the kinetic temperature of the source.

A similar analysis can be done for nonthermal, synchrotron emitting sources. For an optically-thin source, the luminosity is just the volume emission coefficient multiplied by the volume of the source. Therefore, the flux density obeys the relation:

$$S_\nu \propto j_\nu V/D^2. \tag{1.20}$$

where D is the distance to the source. Substituting the synchrotron emission coeffi-

Table 1.1: **Typical Spectral Indices for Astrophysical Objects**

Object Class	Typical α	Reference
radio galaxies	-0.8	Kellermann and Owen, 1988
pulsars	-2	Lorimer *et al.*, 1995
quasars	> -0.5	Kellermann and Owen, 1988
filled centre SNR	-0.2	Wallace, 1991
shell type SNR	-0.5	Wallace, 1991
HII regions	$-0.1 \rightarrow 2$	Altenhoff *et al.*, 1960

cient of equation 1.9 yields the relation:

$$S_\nu \propto \nu^{(1-p)/2} \tag{1.21}$$

for the dependence of the flux density on the particle index of a nonthermal source. The spectral index is thus $\alpha = (1-p)/2$.

Empirically, nonthermal sources typically have negative spectral indices (although no theoretical limit is implied on their value by equation 1.21, or more specifically equation 1.9). Thus, the particle index should typically be positive. Lang (1980) lists 383 radio galaxies and quasars which have spectral indices ranging roughly from -1.5 to 0.5. This implies a typical range of particle indices, p, of between 2 and 4 in these sources. Table 1.1 compiles typical values of spectral indices for astrophysical objects prominent in the radio. The value for pulsars is based on a distribution of 343 pulsars.

Thus, the spectral index is an unambiguous indicator of nonthermal emission if $\alpha < -0.1$.

1.3 Evolution of Shell-like SNR

As fundamental as the identification of a source of emission as an SNR is the understanding how such objects evolve. Their importance as suppliers of energy to the ISM has already been mentioned, but it is equally important to understand how the ISM affects the appearance and physics of these objects. Indeed, it is the interaction of the ejecta with the ambient medium which is the supernova remnant.

The dynamics of an explosion in a uniform medium is governed by the shock wave produced between the ejecta and the surrounding medium (Spitzer, 1978; Sedov, 1959). As the shocked gas cools, shell-type SNR pass through four evolutionary phases before disappearing into the ISM. Each of these will be discussed in turn.

Phase I: Free Expansion

This phase is dominated by the mass of the ejecta. The mass of swept-up material of the ISM is negligible. The radius of the blastwave increases linearly with time, such that

$$R_s = v_0 t \tag{1.22}$$

where v_0 is the velocity of the ejecta imparted by the SN. The ejecta is considered to be expanding without hinderance into the medium which surrounded the star.

Phase II: Adiabatic (Sedov-Taylor) Expansion

This phase begins when enough of the ISM has been swept up (several stellar masses) that significant deceleration has occurred. This phase is modelled as the result of an instantaneous injection of energy into the ISM (Sedov, 1959). The gas is heated and begins an adiabatic expansion outwards. In the adiabatic phase, cooling times are much longer than the age of the remnant, meaning that radiative losses remain negligible and energy is conserved. The heating mechanism is the compression of the ISM by the shock front. The gas left in the wake of the shock is very hot ($\sim 10^6$K) and has a density lower (~ 0.01cm^{-3}) than the assumed average value for the ISM, (~ 1cm^{-3}). It is this heated gas which is the source of the strong X-ray emission observable from some SNR (Kulkarni and Heiles, 1988; Reynolds, 1988). Behind the shock, the gas and magnetic field are compressed, and the synchrotron emission from relativistic electrons rises.

The radius of the shell in this phase is given by

$$R_s(t) = 31.5(E_{51}/n_0)^{1/5} t_5^{2/5} \quad \text{(pc)} \tag{1.23}$$

where E_{51} is the initial kinetic energy of the ejecta in units of 10^{51}erg, n_0 is the interstellar hydrogen density in cm^{-3}, and t_5 is the SNR age in units of 10^5yr (Shull *et al.*, 1989, hereafter S89).

Phase III: Radiative (Snowplow) Expansion

This phase is entered when the remnant's age is comparable to the radiative cooling time, so energy is no longer conserved. This occurs when approximately half the thermal energy is lost. The shock begins to decelerate appreciably and the remnant expands so as to conserve momentum as it continues to sweep up the mass of the ISM.

The time at which the transition from Phase II to Phase III occurs is

$$t_{rad} = (1.33 \times 10^4) E_{51}^{3/14} n_0^{-4/7} \xi_m^{-5/14} \quad \text{(yr)} \tag{1.24}$$

where ξ_m is a metallicity factor[3] and is unity for solar abundances (Cioffi *et al.*, 1988).

[3] The metallicity is commonly measured by the ratio of iron abundance to that of hydrogen.

For times much greater than the onset of the radiative phase, the radius of the shell is given by

$$R_s(t) \approx 27.9 E_{51}^{0.221} n_0^{-0.257} \xi_m^{-0.0357} t_5^{0.3} \quad \text{(pc)} \tag{1.25}$$

(Cioffi *et al.*, 1988).

Phase IV: Dissipation

The shock disappears when its speed drops below the local ISM sound speed (~1km/s). However, the SNR will be disrupted earlier by the turbulent motions of the ISM, which are macroscopic and have speeds estimated to be 8km/s (Spitzer, 1978). A range of speeds from 10km/s to 30km/s has more recently been suggested (Reynolds, 1988). This stage is thought to occur between 10^5 and 10^6yr after the SN, depending greatly on the structure of the ISM where the SN occurred.

1.4 Pulsar/SNR Associations

Due to the fact that pulsars and SNR are expected to be born in the same cataclysmic event, a SN, the earliest discoveries of pulsars were closely followed by searches for associations with extended radio sources which were expected to be the related SNR. However, following the discovery of the Crab pulsar in 1968 (Staelin and Reifenstein, 1968) and the subsequent discovery of the pulsar associated with the Vela SNR (Large *et al.*, 1968), surprisingly few SNR and pulsars were found together, despite targeted searches about known pulsars and SNR.

The absence of SNR about pulsars was not completely unexpected, since pulsars are expected to live and remain observable for much longer periods than SNR. More alarming was the lack of initial detections of pulsars within observed remnants, even those believed to be young.

1.4.1 Established Pulsar/SNR Associations

Crab-like and composite remnants, even those for which the pulsar is not directly observable, are assumed to contain a central pulsar. The pulsar is believed to be the source of both the magnetic fields which power the synchrotron radiation and the relativistic particles accelerated by the fields (Helfand and Becker, 1987; Srinivasan *et al*, 1984). Those remnants for which the pulsar is not directly observed, however, are not classified as associations. A reliable association requires both similarity in age and distance, as well as the more obvious spatial coincidence.

Throughout the 1980's only five associations were known, while that number is now quoted as between 13 (Caraveo, 1995) and 18 (Gaensler and Johnston, 1995b). The discovery of many of the newer associations followed the launch of the Einstein X-ray Observatory which was successful at detecting pulsating sources, such as PSR 1509-58 (Seward and Harnden, 1982) and PSR 0540-69 (Seward *et al.*, 1984), within known SNR. Additionally, deeper radio searches around young pulsars have been particularly successful in detecting faint SNR shells (Caswell *et al.*, 1987; Caswell *et al.*, 1992; Frail *et al.*, 1994a, hereafter F94).

Caraveo (1995) points out that the ten youngest pulsars have all been associated with SNR. However, not all these associations are universally accepted, as several require very high pulsar velocities (eg. 1700km/s for PSR 1800-21 and 1600km/s for PSR 1757-24 and PSR 1610-50). Proper motion measurements have shown that pulsars are high-velocity objects (Lyne *et al.*, 1982). However, the average transverse velocity has been measured to be 100km/s (Cordes, 1986). More recent estimates of Lyne and Lorimer suggest that the rms birth velocities are on the order of 450 ± 90km/s (1994). There is some question as to whether or not velocities much greater than 500km/s are physically achievable, even accounting for powerful kicks which can be conferred on the pulsar in the SNe (F94; Janka and Müller, 1994; Lyne and Lorimer, 1994).

Whether or not these associations are valid, it is evident that ~15 associations among almost 200 known SNR (Green, 1995) and 558 pulsars (Taylor *et al.*, 1986) seems a very small number.

1.4.2 Questioning the Establishment

Observations of SNe imply that ~17% should be Type Ia and leave no pulsar (van den Bergh *et al.*, 1987). Additionally, selection effects associated with their detection such as directional beaming, low luminosity, high dispersion and short periodicity (Narayan and Schaudt, 1988) should lead to an underestimate of pulsar birthrates.

However, these factors do not account for the lack of observed associations, since the birthrates of SNe, pulsars and SNR seem to be comparable. Recent estimates predict that our Galaxy should produce 1 SN every 40 years (Taummann *et al.*, 1994), one SNR every 40 years (Leahy and Wu, 1989) and a pulsar anywhere from one per 15 years (Wakatsuki *et al.*, 1992) to one per 125-250 years (Lorimer *et al.*, 1993).

In a recent publication, Gaensler and Johnston (1995b) have attempted to predict how many associations one might expect to see based on some broad assumptions. They have simulated a Galactic population of pulsars and SNR by seeding their galaxy with 35,000 SNe. They have assumed that all the SNe are Type II and create a shell-type SNR and a pulsar (i.e. that all three birthrates are equivalent, but the actual value of the rate was left as a free parameter in their model). They estimate that ignoring the contribution of Type Ia SNe should cause them to overestimate the number of associations by about 15%.

They assigned the pulsars characteristics according to the work of Lorimer *et al.* (1993). Additionally, the luminosity evolution of the SNR was modeled after the spherically symmetric evolutionary model of Gull (1973) with the assumption that a shell evolves independently of any plerionic component that may be present (Helfand and Becker, 1987). The maximum pulsar characteristic age was constrained to 3Myr.

Gaensler and Johnston used the parameter β to identify possible associations, where β is the ratio of the angular distance of the pulsar from the SNR centre to the mean angular size of the SNR (after S89). To be considered an association, β had to be less than 2. Additionally, the pulsar had to be younger than 10^5yr. For young associations, they note that the likelihood of $\beta < 1$ should be high. However, they do note that for old associations ($> 10^5$yr), the likelihood of $\beta > 1$ is of course greater.

The subsequent mock survey performed on the artificial galactic population revealed that 2/3 of the associations detected were in fact geometric coincidences, and that only five genuine associations were to be expected from such a population.

The implication of Gaensler and Johnston's work is that one does not expect to see a large number of young ($< 10^5$yr) pulsar/SNR associations. However, depending on the radiative lifetime of SNR and the distribution of pulsar velocities, one may expect to see more older associations (Gaensler and Johnston, 1995a).

1.4.3 The Radiative Lifetimes of SNR

Whether or not SNR live long enough to interact with pulsars is a fundamental question. Although the results of Gaensler and Johnston's work has addressed the absence of associations with some success, those that are known can still provide information about the dynamics of SNR, pulsars and the ISM. Additionally, their results depend critically on the radiative lifetimes of SNR. Obviously, the longer their lifetimes, the more associations that ought to be observed. Thus, a discussion of some recent arguments about how long SNR may be able to survive is relevant.

Based on their observations at 20cm with the VLA about three young pulsars ($\sim$20,000yr) which resulted in no detections of extended emission which could represent associated SNR, Braun *et al.* (1989) suggested that a mean observable SNR lifetime of less than 20,000yr was likely for both pulsar and blast-wave powered remnants. They attribute the rapid luminosity decline of both pulsars and remnants to many massive supernovae occurring within regions of low density ($\sim$0.01cm^{-3}) created by the strong stellar winds of the progenitor stars.

F94 reject these age limitations, noting that later VLA images at 90cm of one of the pulsars studied by Braun *et al.* (1989) in fact revealed a previously unknown 45$'$ SNR, W30 (Frail *et al.*, 1994b; Kassim and Weiler, 1990). Also, F94 estimated that the typical density into which the SNR are evolving is 0.2cm^{-3}, not the low density of 0.01cm^{-3} calculated from the earlier studies (Braun *et al.*, 1989; Bhattacharya, 1990).

If the shell lives long enough, then the pulsar should be able to catch up to and eventually overtake the expanding shell. G341.2+0.9[4] is an SNR which has been

[4]The designation of radio sources is based on Galactic coordinates: G(longitude) $\pm$ (latitude).

noted to show brightening near the location of its pulsar. The pulsar is therefore thought to be interacting with the shell (F94).

The Interaction Model of Shull *et al.*

S89 have asked the question: what fraction of active pulsars can catch up with their parent shells? The answer must take into account the lifetime of the shell and the velocity distribution of pulsars.

Based on equation 1.23, a pulsar with velocity 100km/s (V_{100}) would be expected to catch up to a shell in the adiabatic phase at a time

$$t_{cu}^{II} = (6.5 \times 10^5) E_{51}^{1/3} n_0^{-1/3} V_{100}^{-5/3} \quad (\mathrm{yr}). \tag{1.26}$$

Similarly, for a remnant in the radiative phase, the catch up time from equation 1.25 is

$$t_{cu}^{III} = (4.2 \times 10^5) E_{51}^{0.116} n_0^{-0.144} \xi_m^{-0.0086} V_{100}^{-1.43} \quad (\mathrm{yr}). \tag{1.27}$$

S89 speculate that where a pulsar is interacting with a shell, a nonthermal nebula should result. The expected number of such interactions would be dependent on four factors:

1. the duration of the interaction, Δt;
2. the fraction of SNR shells which remain intact to time τ, $f_s(\tau)$;
3. the fraction of pulsars with space velocity sufficient to catch the shell, $f_p(\tau)$;
4. the fraction of all pulsars that are beamed toward Earth (this dependence is weak since observing the interaction does not require that the pulsar itself be observable), f_b.

The lifetime of pulsar-shell interactions is

$$\Delta t \approx (2 \times 10^4) r_{pc} V_{100}^{-1} \quad \text{(yr)} \tag{1.28}$$

where r_{pc} is the distance of the pulsar from the shell in parsecs necessary to produce the observable radio emission. Taking the number of pulsars in the Galaxy to be ∼500 (S89) and assuming that a pulsar remains active for 2×10^6yr (Lyne, Manchester and Taylor, 1985) then the number of visible shell interactions would be

$$N_{int} \approx 5 r_{pc} V_{100}^{-1} f_p(\tau) f_s(\tau) f_b^{-1} \left(\frac{N_p}{500}\right). \tag{1.29}$$

From equation 1.27, the pulsar velocity needed to catch a shell of age τ is

$$V_p = 170 \left(\frac{\tau}{2 \times 10^5 \text{yr}}\right)^{-0.7} E_{51}^{0.08} n_0^{-0.1} \xi_m^{0.006} \quad \text{km/s.} \tag{1.30}$$

Using $f_p \approx 0.1$ (Lyne, Anderson and Salter, 1982; Cordes, 1986) and using a beaming factor of $f_b = 0.2$ (S89), then

$$N_{int} \approx 1.5 r_{pc} f_s(\tau) \left(\frac{N_p}{500}\right). \tag{1.31}$$

The authors take r_{pc} equal to 4 based on their observations of CTB 80, a remnant which the authors claim is a prime example of rejuvenation of a shell in the snowplow phase by the passing pulsar 1951+22 (S89). With the additional assumption that all shells live to be at least 2×10^5yr old (i.e. $f_s(\tau) \approx 1$), then 6 pulsar-shell interactions should be seen. In the same paper, the authors put forth the case for three other examples of such interactions: G5.4-1.2; G6.4-0.2; and G27.4+0.0.

These results imply that some SNR shells can remain intact for more than 10^5yr. Based on this conclusion, S89 examine how many expected interactions should be

Table 1.2: **Number of Expected Interactions for Three Shell Lifetimes**

Shell lifetime (yr)	Minimum Pulsar Catch-up Velocity (km s^{-1})	f_p	N_int
2×10^5	170	0.10	$6f_s$
5×10^5	88	0.34	$39f_s$
1×10^6	55	0.53	$96f_s$

visible with even older shells. Table 1.2 shows how many interactions might be expected for three shell lifetimes. The velocity required by the pulsar of course decreases as the shell lifetime is increased, but so does f_s. Even if only 1% of shells reach ages of 10^6yr, then at least one should statistically be observable given the number of shell-type SNR known.

1.5 The Casper Region

For this thesis, Casper is the designation given to the collection of features within a region of the sky centred on the J2000 coordinates RA $19^h32^m00^s$ and Dec $+20°6'0''$. This region is a mere half a degree from the Galactic plane; therefore, there is a great deal of emission present at most wavelengths which can lead to confusion of sources. Several components of Casper have been studied previously; however, no investigation of the possible relation between the objects has ever been attempted (since poor resolution has prevented distinction or detection of some components in past studies). Thus, the nature of the emission features remains unclear.

Figure 1.2 contains all the features that have been analyzed in the past: the radio source G55.6+0.7 north of the map centre (Casper's eyes); the pulsar which is contained within the "left-eye" of G55.6+0.7 (marked by a cross); and G55.2+0.5 which is made up of both G55.6+0.7 and the half-shell of emission south of the map centre (Casper's smile).

The primary goal of this thesis is to determine the natures of Casper's components –specifically, whether Casper contains an SNR, or more than one, as might be concluded from the historical analysis of the region discussed below. The unscientific designation was arrived at due to the appearance of the collection of objects, which includes the two identified regions of extended radio emission and a pulsar as well as numerous point sources. The historical analysis of this intriguing region follows.

1.5.1 The Pulsar J1932+2020 (B1929+20)

Casper's pulsar was discovered in 1974 following a pulsar survey by Hulse and Taylor (1974,1975). Its first designation was B1930+20, but more accurate measurements of its position led to its renaming as B1929+20. This position is unique to coordinates in the epoch of 1950. Pulsars are named according to their positions on the sky in the coordinate system of right ascension (RA) and declination (Dec or δ). These coordinates vary depending on the epoch of observation, thus the designations of pulsars also vary. Its designation in J2000 coordinates is J1932+2020, and this is the nomenclature which will be used hereafter.

J1932+2020 has not been the object of specific study but it has been observed in a number of surveys since its discovery (Gullahorn and Rankin, 1978; Manchester and Taylor, 1981; Hankins, 1987; Frail and Weisberg, 1990; Frail *et al.*, 1991; Arzoumanian *et al.*, 1994; Lorimer *et al.*, 1995). Arzoumanian *et al.* made measurements of 96 radio pulsars over a four year period from 1989 to 1993. Their data for

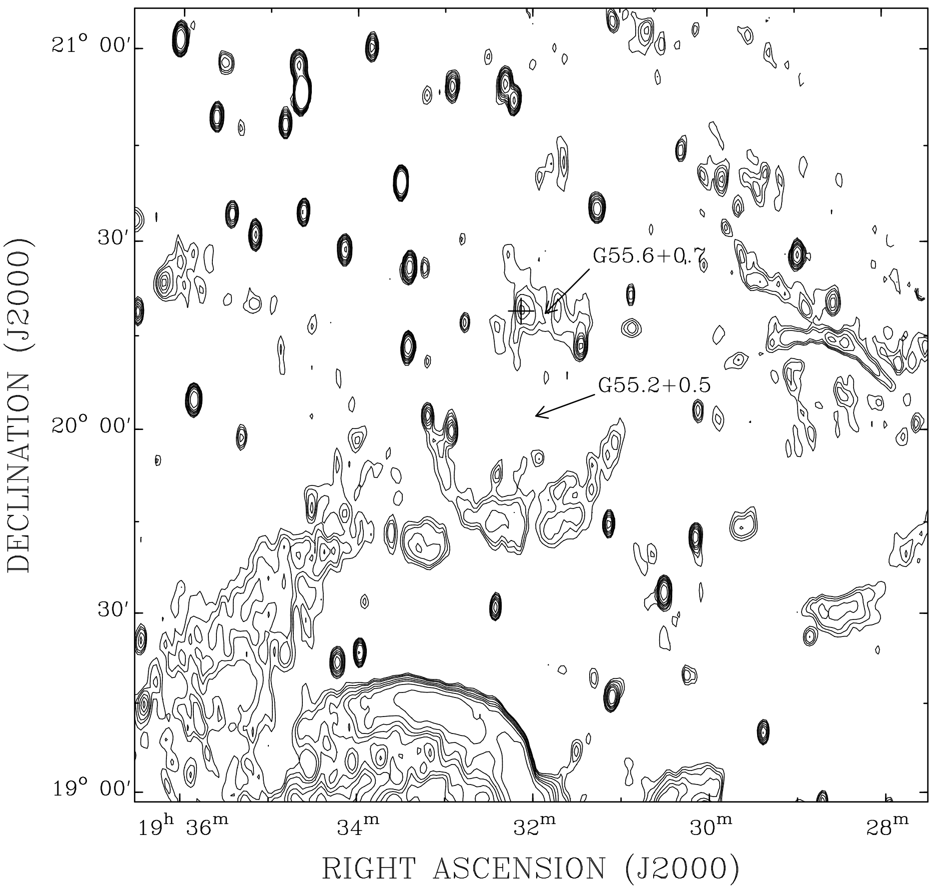

Figure 1.2: **1992 327MHz Image of Casper**

This image illustrates the various features of which "Casper" is comprised. The pulsar J1932+2020 is located at the position of the cross; the radio source G55.6+0.7 consists of all the heightened flux density surrounding the pulsar; and G55.2+0.5 is comprised of the source G55.6+0.7 as well as the pronounced shell to the south. These coordinates, as marked on the image, denote the centres of the radio emission.

Table 1.3: **Established Parameters of J1932+2020**

		1σ
RA	$19^h32^m8.30^s$	3
Dec	$20°20'46.30''$	6
Period, P	0.268216854361s	3
$\dot{P}(\times 10^{-15})$	4.21630	18
dispersion measure	$211.007\mathrm{cm}^{-3}\mathrm{pc}$	17

J1932+2020 are assembled in Table 1.3. The errors quoted are based on random and systematic errors and are on the last significant digits of the values.

J1932+2020 has been noted to have an excessively broad profile. This has been interpreted as evidence for a great deal of interstellar scattering along the line of sight to the pulsar (Lorimer *et al.*, 1995).

Frail and Weisberg (1990) measured the distance to the pulsar using absorption features in neutral hydrogen. Based on these data, the pulsar is at a distance of at least 4.8 ± 1.8kpc but no greater than 14.9 ± 0.9kpc. The technique used to measure distances in this manner will be discussed in Chapter 5. The distance estimate from the dispersion measure is $\sim$9kpc based on the electron density model of Taylor and Cordes (1986), for which the authors estimate a 25% uncertainty.

Based on the spindown measure, the pulsar's age can be estimated via equation 1.4 and the data of Table 1.3 to be just over one million years.

As recorded in Table 1.1, pulsars typically have very negative spectral indices. Lorimer *et al.* (1995) measured the flux densities of J1932+2020 over a period of three years using the 76m Lovell telescope at Jodrell Bank. Based on data at 408MHz, 606MHz and 1408MHz, its spectral index was measured to be -2.5 ± 0.2.

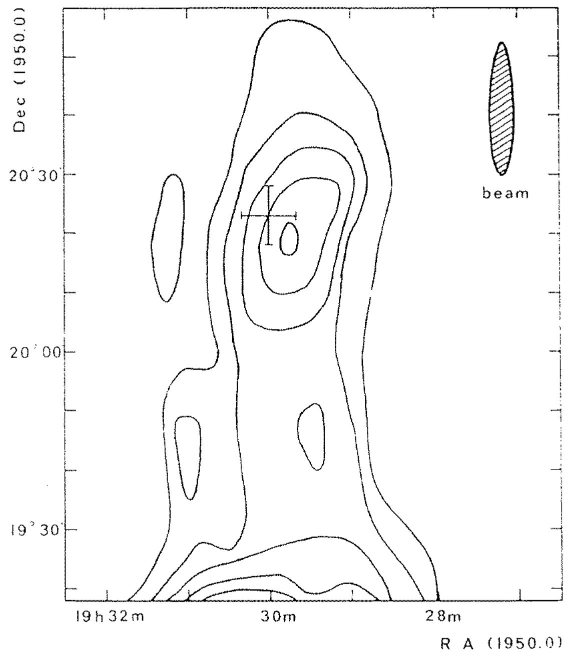

Figure 1.3: **1974 1420MHz Image of G55.6+0.7**
The size of the beam (resolution) of this image is given by the shaded ellipse. Its size is $4' \times 22.5'$. The pulsar is located by the position of the cross. Coordinates are B1950. *(reproduced from Astron. Astrophys. with permission from Crovisier)*

1.5.2 The First Mention of a Possible SNR

Shortly after the detection of the pulsar in 1974, a possible association was noted between the pulsar and the extended radio source G55.6+0.7 (Crovisier, 1974). Figure 1.3 shows Crovisier's data and the position of the pulsar as known at the time.

The radio source G55.6+0.7 had been detected at 610.5MHz with very poor resolution (Wendker, 1968) and 2695MHz (Altenhoff *et al.*, 1970). To these measurements, Crovisier added a 1420MHz detection using the Nancay Radio Telescope. The data compiled for G55.6+0.7 up to and including Crovisier's work are reproduced in

Table 1.4: **Detections of G55.6+0.7 as of 1974**

Frequency (MHz)	Resolution	Integrated Flux Density (Jy)
610.5	$20' \times 30'$	13.1 ± 3.4
1420	$4' \times 22.5'$	5 ± 2
2695	$11 \times 11'$	4

Table 1.4.

Crovisier determined that the estimated pulsar position lay within the beamwidth of the radio source, although the size of the beam meant that the region was poorly resolved (compare the 327MHz image of 18 years later shown in Figure 1.2). His search of the Palomar Sky Survey prints revealed no optical counterpart to the radio emission. Both the 610.5MHz and the 1420MHz flux densities of G55.6+0.7 were poorly determined due to confusion with Galactic background because of the low angular resolution. The spectral index based on these two frequencies was $-2.0 < \alpha < -0.4$. Crovisier noted that this result was consistent with the measured 11cm (2695MHz) flux density of Altenhoff *et al.* (1970).

A recalculation of the spectral index has been done using all three frequencies of Table 1.4 from which $\alpha = -0.8 \pm 0.3$ was obtained. As the uncertainty in the 2695MHz was not provided by the authors, it was assumed to be 25%. Clearly, this result suggests, as the two frequency calculation does, that G55.6+0.7 is a nonthermal radio source which could be related to the nearby pulsar. Crovisier further speculated that, based on its circular appearance (diameter $\sim 20'$) and the presence of the pulsar, the source could be a new SNR. However, this result relied heavily on the 610.5MHz data point, without which the spectrum would be flat.

Table 1.5: **Detections of G55.6+0.7 as of 1986**

Frequency (MHz)	Resolution	Integrated Flux Density (Jy)	Telescope
1420	$9.3' \times 9.3'$	2.2 ± 0.3	Effelsberg 100m
2695	$4.27' \times 4.27'$	1.8 ± 0.2	Effelsberg 100m
4750	$2.4' \times 2.4'$	1.8 ± 0.2	Effelsberg 100m
10000	$2.7' \times 2.7'$	1.8 ± 0.3	Nobeyama 45m

Since those data also have the poorest resolution, other verification was obviously needed.

In 1986, following two Galactic plane surveys with the Effelsberg 100m single dish telescope, new data were published regarding the radio source G55.6+0.7. Table 1.5 contains the data of Reich *et al.* (1986). Angular resolution of these data was much improved. Using these data, the spectral index of G55.6+0.7 was determined to be flat, with a value of $\alpha = 0.0$ (Reich *et al.*, 1986). This, coupled with the fact that there was no significant polarization detected above the sensitivity limit of 5% at 4750MHz, led the authors to conclude that the radio source was most probably an HII region.

This analysis ignored the measured flux density at 610.5MHz, perhaps because of the poor quality of the resolution. The spectral index of G55.6+0.7 was recalculated using the data of Reich *et al.*, yet including the measurement of 610.5MHz from Wendker (1968). This of course skews the spectral index considerably. Including these data, a value of -0.4 ± 0.3 with a large scatter was obtained. This result is consistent with the conclusion that the region is thermal, but just barely.

1.5.3 The Second Proposed SNR

In 1992, following a 327MHz survey of the Galactic plane using the Westerbork Radio Synthesis Telescope (WRST) in Holland (Taylor *et al.*, 1996), a case was put forth for the presence of an SNR including Crovisier's proposed SNR of 1974 plus a shell now visible to the south (see Figure 1.2). The object was designated G55.2+0.5. The authors speculated that both features were part of a single shell-type SNR. It is this overall feature which is referred to herein as Casper. Its mean spectral index from 327MHz (Taylor *et al.*, 1992) and 4850MHz (Condon *et al.*, 1989) data was $\alpha = -1.46 \pm 0.49$. The object was estimated to have a diameter of $\sim 30'$. The fact that these were the highest resolution and lowest frequency data taken of this region made the detection of the southern shell possible.

The initial identification as an SNR was tentative for several reasons:

- The flux density scale was not known well when the preliminary estimates of the 327MHz flux were done. Later corrections were on the order of 10%.
- The overall spectral index is not well-defined due to the faintness of the southern shell (smile).
- At least one background point source was included in the calculation of the flux density of the extended emission which could affect the value of the spectral index.
- Attempts to investigate the infrared nature of the source with the 60μ data were unsuccessful due to confusion in the images.

The conclusion reached was that higher frequency observations of comparable resolution to the 327MHz data were needed at high sensitivity to obtain a more accurate spectral index determination in order to conclusively confirm the nature of the object.

1.6 The Present Problem

This thesis will attempt to settle the question of the nature of the various sources of radio emission within the object Casper. Regions within Casper have been labelled as possible SNR and as HII regions in the past, but these data are far from conclusive. The focus of this study was to obtain higher radio frequency data (1420MHz) of comparable resolution to that of the 327MHz WSRT data already discussed. This enabled a comparison of low frequency to high frequency radio morphology which, it was hoped, would permit clearer interpretations of the nature and history of the object (and the objects within) Casper. Additionally, an HI spectrum was obtained in order to examine the neutral gas in the region for evidence of interaction with the ISM and possibly determine the distance to the object(s).

To obtain high angular resolution at higher frequency, aperture synthesis observations were carried out. Chapter 2 deals with the method of aperture synthesis. Chapter 3 explains the data reduction and summarizes all the data used in our analyses. Chapter 4 establishes which components of Casper are nonthermal by analysis of the continuum data while Chapter 5 discusses the physics of the nonthermal component, making use of the HI line data. Finally, Chapter 6 summarizes the conclusions of this thesis and presents possible research directions which could build upon the work presented here.

Chapter 2

Radio Interferometers

2.1 Aperture Synthesis

Aperture synthesis is the technique used to extract images from data taken by arrays of radio (or other wavelength ranges in the future) antennae. It was developed in the 1970s to help remedy confusion caused by limited angular resolution. It has the advantage of allowing one to extract data of superior resolution and sensitivity to that which can be achieved by any single dish of the array on its own. The term synthesis refers to the fact that the array functions to synthesize the aperture of a very large single antenna using several smaller antennae; such telescopes are called *synthesis telescopes*.

2.1.1 Radio Antennae

Since the goal of this analysis is informative and not rigorous, the following discussion will initially be restricted to one angular dimension. Imagine a radio source which has an intensity distribution $I(\theta)$ on the sky, where θ is an angular sky coordinate. A single radio antenna has a power pattern $A(\theta)$ which measures the response of the antenna as a function of the direction from the antenna's pointing axis. This function is also called the *primary beam* of the antenna and is typically normalized such that $A(0) = 1$. Figure 2.1 defines angular directions based on a single radio antenna pointing in the direction θ_0. The object of observation can be an angular

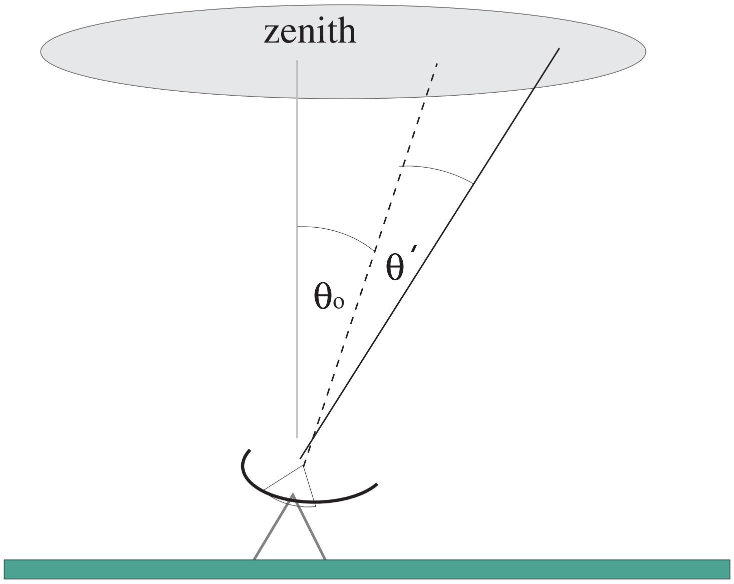

Figure 2.1: **A Typical Radio Antenna**
This diagram depicts a single radio antenna observing along the θ_0 direction (called the pointing axis). It can measure sky intensities offset from the pointing axis at angles θ'. The oval represents the sky intensity distribution observed by the antenna.

distance θ' from θ_0.

The telescope's response to a differential element of the source contained within the angle $d\theta$ will be

$$dV(\theta_0) = I(\theta)A(\theta - \theta_0)d\theta \tag{2.1}$$

where $V(\theta_0)$ is the signal received when the antenna is pointed in the direction of (θ_0) and $A(\theta - \theta_0)$ is the power pattern in the direction θ (where $\theta = \theta_0 - \theta'$). Integration over the entire source yields

$$V(\theta_0) = \int I(\theta)A(\theta - \theta_0)d\theta \tag{2.2}$$

for the measured signal. Thus, the response of the telescope is a convolution of the primary beam with the sky intensity distribution. The angular dimension of $A(\theta)$ therefore determines the resolution of the image of the sky.

The resolution of an antenna is a function of its diameter, a. In units of wavelengths, the diameter is $a_\lambda = a/\lambda$. Then the angular resolution of the antenna obeys the relation:

$$\theta_r \propto 1/a_\lambda. \tag{2.3}$$

Thus, larger telescopes have better resolution [i.e. a narrower $A(\theta)$].

The largest steerable radio telescope is 100m in diameter (Effelsberg in Germany). This size approaches the weight limit for which the antenna can be supported and moved. The largest single dish telescope is at Arecibo and is 300m in diameter but not steerable (although limited pointing is possible through motion of the focus). Luckily, radio arrays exist which eliminate the need for still larger single dish telescopes.

An interferometer of two antennae of equal diameter separated by a distance (called a *baseline*) L_λ as shown in Figure 2.2 has a resolution of

$$\theta_r \propto 1/L_\lambda \tag{2.4}$$

which is superior to the single dish relation since the baselines can be made arbitrarily long.

2.1.2 Interferometers and the Visibility Function

In order to obtain the form of the signal received by an interferometer (an array consisting of two antennae, each with a response function given by equation 2.2), it is often useful to make use of the reciprocity theorem which states that the power

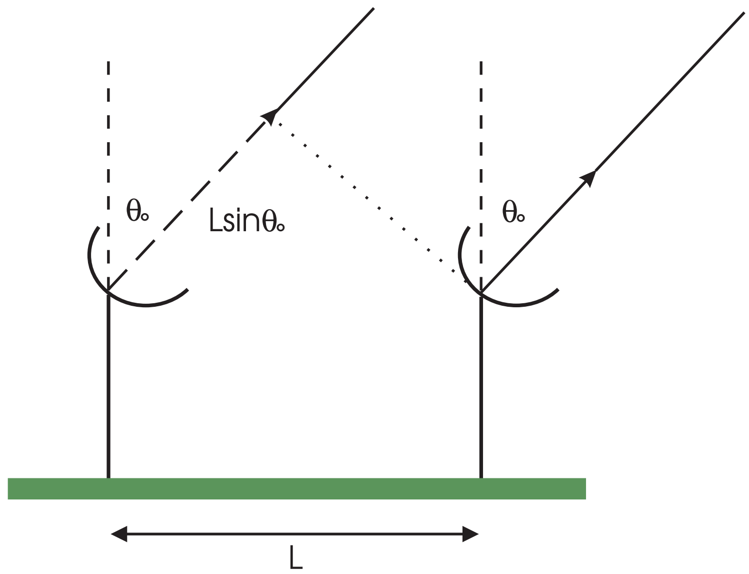

Figure 2.2: **A Two-Element Emitting Interferometer**
The antennae are separated by a distance L, called a baseline. The separation introduces a phase delay between the signals emitted by the antennae equivalent to (Lsin θ_0)/λ. The time delay to remove the phase delay is given by the expression $\tau_D = (L \sin\theta_0)/c$. Compensation for the phase delay ensures that the interferometer's emitted signals are in phase at infinity.

pattern is the same whether the antenna is receiving or transmitting. The power pattern of an antenna is given by the square of the far-field electric field pattern $A(\theta) = E^2(\theta)$, where $E(\theta)$ is the electric field at infinity from an emitting antenna. Thus, two similar *emitting* antennae can be considered to determine the form of the field generated infinitely far from the telescope.

The two emitters are separated by a distance L, which may be expressed in units of the wavelength of the transmitted signal, so that $L_\lambda = L/\lambda$. Figure 2.2 illustrates the two emitters directed at the same pointing centre. If the halfway point between the antennae is taken as a reference point, then the signal emitted at angle θ at either antenna will be out of phase with the reference point by a length $(L_\lambda \sin\theta_0)/2$. The field observed at a far-field position from the telescope would then be given by the combination of two plane waves such that:

$$E(\theta) = E_1(\theta)e^{i\psi/2} + E_2(\theta)e^{-i\psi/2} \tag{2.5}$$

where E_1 and E_2 denote the far-field patterns of individual antennae and the phase term is

$$\psi = 2\pi L_\lambda \sin\theta - 2\pi c\tau_D/\lambda \tag{2.6}$$

where τ_D is a time delay between the transmitted signals that can be introduced as defined by Figure 2.2.

If the emitters are identical, then $E_1(\theta) = E_2(\theta) = E_0(\theta)$, and equation 2.5 becomes

$$E(\theta) = 2E_0(\theta)\cos(\psi/2) \tag{2.7}$$

Note that by adding a factor of $\pi/2$ to the phase of equation 2.6 the far-field pattern becomes

$$E'(\theta) = 2E_0(\theta)\sin(\psi/2). \tag{2.8}$$

Therefore, by introducing this phase shift in the transmitting signal, one can produce either cosine or sine far-field patterns.

The power pattern of an interferometer, $P(\theta)$, will be proportional to the square of equation 2.7, such that

$$P(\theta) = 4E_0^2(\theta)\cos^2(\psi/2) \tag{2.9}$$

which when normalized so that for $\theta = 0$, $\psi = 0$, yields:

$$P(\theta) = \frac{1}{2}A(\theta) + \frac{1}{2}A(\theta)\cos\psi. \tag{2.10}$$

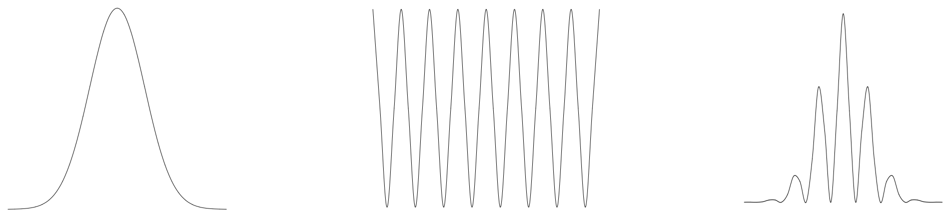

Figure 2.3: **Power Patterns**
The power patterns shown are those of (left to right) a single antenna, an interferometer and an interferometer comprised of two directional antennae, each with power patterns like that the single antenna on the left. Note the presence of sidelobes in the synthesized response pattern.

The first term of equation 2.10 is independent of baseline, since it dependent on only the single antenna response of equation 2.2. Therefore, it will not vary over the sky and is simply a removable constant. The factor $(1 + \cos\psi)/2$ is called the "array factor", so $P(\theta)$ is the product of the single antenna pattern and the array factor. Replacing the power pattern of a single dish with that of our interferometer in equation 2.2 yields an expression for the source signal received when the synthesis telescope is pointed at θ_0:

$$V(\theta_0)_{cos} = \int I(\theta)A(\theta - \theta_0)\cos(2\pi L_\lambda \sin\theta - 2\pi c\tau_D/\lambda)d\theta. \tag{2.11}$$

Figure 2.1 shows that $\theta = \theta_0 + \theta'$. Expanding $\sin\theta$ in equation 2.11 yields

$$V(\theta_0)_{cos} = \int I(\theta_0 + \theta')A(\theta')\cos[2\pi L_\lambda(\sin\theta' \cos\theta_0 + \cos\theta' \sin\theta_0) - 2\pi c\tau_D/\lambda]d\theta'. \tag{2.12}$$

For the remainder of our analysis, the source which the telescope is observing is assumed to be close to the pointing axis, so that $\cos\theta' \approx 1$ and $\sin\theta' \approx \theta'$. Using these approximations and substituting for τ_D as defined in the text accompanying Figure 2.2, the cosine signal is given by

$$V(\theta_0)_{cos} = \int I(\theta_0 + \theta')A(\theta')\cos(2\pi L_\lambda \theta' \cos\theta_0)d\theta'. \tag{2.13}$$

A similar analysis of the sine output of equation 2.8 yields a second measurement from the interferometer:

$$V(\theta_0)_{sin} = \int I(\theta_0 + \theta')A(\theta')\sin(2\pi L_\lambda \theta' \cos\theta_0)d\theta'. \tag{2.14}$$

Thus, the complete signal can be constructed from the cosine and sine receivers in the form:

$$V(\theta_0, L_\lambda) = V(\theta_0)_{cos} + iV(\theta_0)_{sin} = \int I(\theta' + \theta_0)A(\theta')e^{i2\pi\theta'(L_\lambda \cos\theta_0)}d\theta'. \tag{2.15}$$

$V(\theta_0, L_\lambda)$ is called the "complex visibility function" and according to equation 2.15 has a Fourier transform relationship with $I(\theta' + \theta_0)A(\theta')$.

2.1.3 The Sky in Two Dimensions

For the two-dimensional case, the normal convention of taking angular coordinates on the sky to be (l, m) has been adopted. These coordinates can be made to designate the pointing direction of the telescope and thus denote the map centre of the image produced.

Next, a plane is defined perpendicular to the vector which links the source to the observer ($\hat{k}$ on Figure 2.4). This plane is called the $u - v$ plane. The u and v coordinates are the projections of the interferometer's baseline onto the $u - v$ plane.

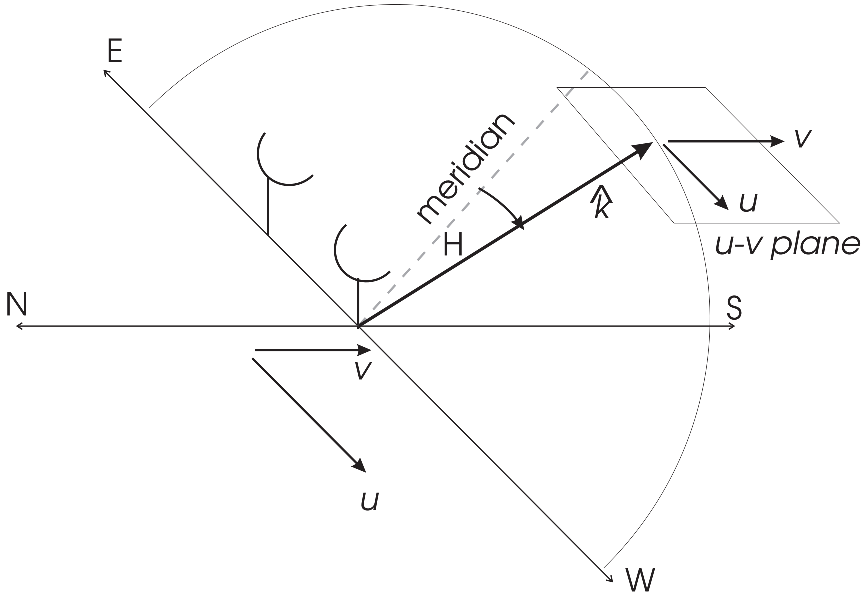

Figure 2.4: **The $u - v$ Plane on the Sky**
This image illustrates two elements of an east-west interferometer with its pointing axis along $\hat{k}$. If the source rises due east of the baseline and sets due west, at these times (for which the hour angle, H, of the source corresponds to 270° and 90° respectively), the source "sees" none of the baseline. When it crosses the celestial meridian (at 0^h), it can see the entire baseline. The $u - v$ plane is perpendicular to the vector $\hat{k}$ which denotes the pointing axes of the elements of the array.

The component u is the projection of the baseline seen by the source in the E-W direction (as illustrated in Figure 2.4). For an East-West interferometer, the amplitude of u varies with the hour angle[1] of the source. The source sees the maximum possible value of u (the length of the baseline) at the time of transit (0^h),

$$u = L_\lambda \cos H, \tag{2.16}$$

where H is the *hour angle* of the source on the sky (270° at rise and 90° at set for an equatorial source).

It can be shown that

$$v = L_\lambda \sin H \sin \delta_0. \tag{2.17}$$

where δ_0 is the declination of the pointing direction of the telescope.

Thus, the visibility function in two dimensions is

$$V(u,v) = \int_\infty^\infty \int_\infty^\infty A(l,m)I(l,m)e^{i2\pi(ul+vm)}dldm, \tag{2.18}$$

and the Fourier transform relationship takes the form

$$A(l,m)I(l,m) = \int_\infty^\infty \int_\infty^\infty V(u,v)e^{-i2\pi(ul+vm)}dudv. \tag{2.19}$$

2.1.4 Imaging

Aperture synthesis, finally, is the process by which the function $A(l,m)I(l,m)$ is constructed from the Fourier transform relationship with the observable values of $V(u,v)$ (referred to as *visibilities*). The principal difficulty now lies in the fact that it is not possible to obtain continuous visibilities out to infinity as required by equation

[1]The hour angle is the angle between the great circle through the zenith and source and the N-S meridian (great circle through north celestial pole and the zenith) as measured westward of the meridian when looking south.

2.19. In order to work around this problem, a *sampling*, or *grating function* $g(u, v)$ is introduced in the $u - v$ domain which is unity for (u, v) coordinates where data exists and zero everywhere else.

Thus, equation 2.19 becomes

$$I'(l, m) = \int_{-\infty}^{\infty} \int_{-\infty}^{\infty} V(u, v) g(u, v) e^{-i2\pi(ul+vm)} du dv \tag{2.20}$$

where $I'(l, m)$ is called a *dirty map* and differs from the product of the true sky intensity distribution with the primary beam because of the presence of the sampling function.

The convolution theorem states that multiplication of two functions in one domain is equivalent to a convolution of the Fourier transforms of those functions in the Fourier transform domain. Thus, from a telescope with finite, discrete sampling in the $u - v$ plane, the observed sky intensity distribution is actually given by the expression:

$$I'(l, m) = [A(l, m) I(l, m)] * G(l, m) \tag{2.21}$$

where $G(l, m)$ is the Fourier transform of the sampling function $g(u, v)$ and the symbol $*$ indicates a convolution.

For an unresolved source at $(l, m) = (0, 0)$, the visibility is constant, since all baselines will produce the same measurement (see equation 2.18). Since $A(0, 0) = 1$, the array's response to a point source can be obtained:

$$G(l, m) = \int_{-\infty}^{\infty} \int_{-\infty}^{\infty} g(u, v) e^{-i2\pi(ul+vm)} du dv. \tag{2.22}$$

$G(l, m)$ is the array point source response function in the image plane and is called the *synthesized beam* or the *dirty beam* of the telescope. It is the parameters of

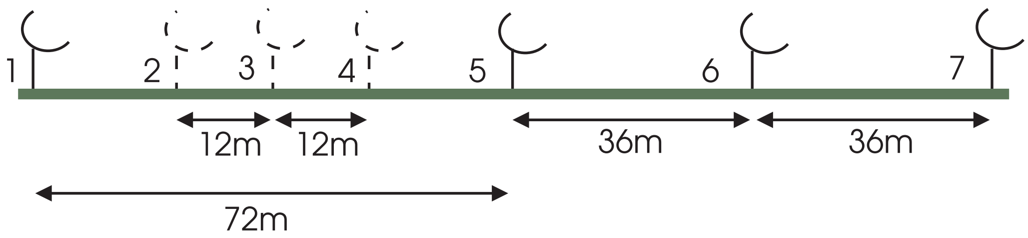

Figure 2.5: **Schematic of the DRAO Synthesis Telescope**

this function that determine the resolving power of the array in the image plane. However, this response function also contains sidelobes, as illustrated in Figure 2.3 and the beam image in Figure 2.6.

2.2 The DRAO Interferometer

The data for this investigation were obtained at the Dominion Radio Astrophysical Observatory (DRAO). The observatory is comprised of a synthesis telescope–an array of seven antennae–and a 26m single dish. Here, the features of the array are discussed.

The seven antennae ("elements") of the array are laid out on an east-west track. The second, third and fourth antennae are moveable, although they maintain a fixed spacing with respect to one another. The permanent spacings are noted on Figure 2.5. The array components are moved daily over a period of twelve days so that the entire range of possible baselines from 12.9m to 604.3m are sampled at intervals of 4.3m, resulting in 140 baselines.

On a given day, the telescope tracks a source through a range of hour angles from

18^h to 6^h (from rise to set). This means that the projected baselines trace out one half of an ellipse on the sky. Observing for the other twelve hour interval is of course impossible, but luckily, it is not necessary. Recalling equation 2.19 and expressing the exponential in terms of trigonometric functions:

$$I'(l,m) = \int_{-\infty}^{\infty}\int_{-\infty}^{\infty} V'(u,v)(\cos 2\pi(ul+vm) - i\sin 2\pi(ul+vm))dudv. \tag{2.23}$$

The left hand side must be real since the flux density is a real quantity. Thus, the imaginary part

$$\Im I'(l,m) = \int_{-\infty}^{\infty}\int_{-\infty}^{\infty} V'(u,v)\sin 2\pi(ul+vm)dudv \tag{2.24}$$

must be zero. The only way this integral can be zero is if the integrand is an odd function. Since sine is odd, then $V'(u,v)$ must be even. Therefore,

$$V'(u,v) = V'(-u,-v) \tag{2.25}$$

and the unmeasureable data can be obtained from the measureable data. Thus one day of observations provides visibility along a full elliptical track in the $u-v$ plane for each baseline.

2.2.1 Grating Rings

The dirty map contains the effects of the sampling function because it contains a convolution with the dirty beam, $G(l,m)$. The synthesized beam is "dirty" because it has ugly sidelobes which arise from the finite nature of the sampling function in the $u-v$ plane. The sampling function is a distribution of delta functions located wherever there is a visibility data point.

Since an east-west array has regular spacings between baselines, visibility coverage consists of a series of elliptical rings separated by Δu and Δv on the (u, v) axes. The Fourier transform of the regularly spaced elliptical tracks is a similar pattern of elliptical tracks in the image plane with spacings of $1/\Delta u$ on the l axis and $1/\Delta v$ on the m axis. If the spacings between the rings in the visibility plane are close enough together, then the first ring in the image plane can be made to lie outside the primary beam for a source at the centre on the map.

2.3 Deconvolution and Calibration Techniques

2.3.1 CLEANing

As shown by equation 2.21, dirty maps are simply the sky intensity distribution convolved with the synthesized beam. Deconvolution is the process of removing the "ugly" synthesized beam and replacing it with a "less-ugly" version modelled after the first. This process in radio astronomy is called CLEAN.

The dirty beam will always have sidelobes because of the truncation of the sampling function in the $u - v$ plane at the longest baseline. The true sampling function can be thought of as an infinite sampling function multiplied by a pillbox function. The Fourier transform of a pillbox is a sinc function, which can have sidelobes of significant amplitude with respect to the peak.

The first step in cleaning the data is the assumption that the true sky can be expressed as a sum of delta functions of varying amplitudes, D_i. Thus,

$$I(l, m) = \sum_{i=1}^{N} D_i \delta(l - l_i, m - m_i) + \varepsilon(l, m) \tag{2.26}$$

where (l_i, m_i) are the coordinates of the delta functions and $\varepsilon(l, m)$ represents the noise in the map.

The observed sky distribution is convolved with the synthesis beam:

$$I''(l,m) = \sum_{i=1}^{N} D_i G(l - l_i, m - m_i) + (\varepsilon(l,m) * G(l,m)). \tag{2.27}$$

The second term is called the residual map and denoted $I_R(l, m)$. Obviously, if one could find the $D_i(l, m)$ then the true sky intensity distribution could be determined.

As mentioned, the method used to determine these coefficients is called CLEAN. The basic idea is as follows:

- The maximum in the map is found and its amplitude and coordinates are recorded–$D_{max}, l_{max}, m_{max}$.

- Some fraction of the maximum value is subtracted from the dirty map, such that $I''(l,m)_{remaining} = I''(l,m) - fD_{max}G(l - l_{max}, m - m_{max})$ where f is called the "loop gain" and is typically between 0.1 and 0.2.

- The values of fD_{max}, l_{max} and m_{max} are stored as D_1, l_1 and m_1.

- The maximum in the remaining map is then found and the process is performed iteratively until $D_{max} \leq$ some preset value, or until a preset number of iterations have been completed.

This procedure results in a series of D, l and m values. These are called "clean components" and a map can be constructed from them. It will consist of single points and is a "super-resolution" map, since the effects of the beam have been completely

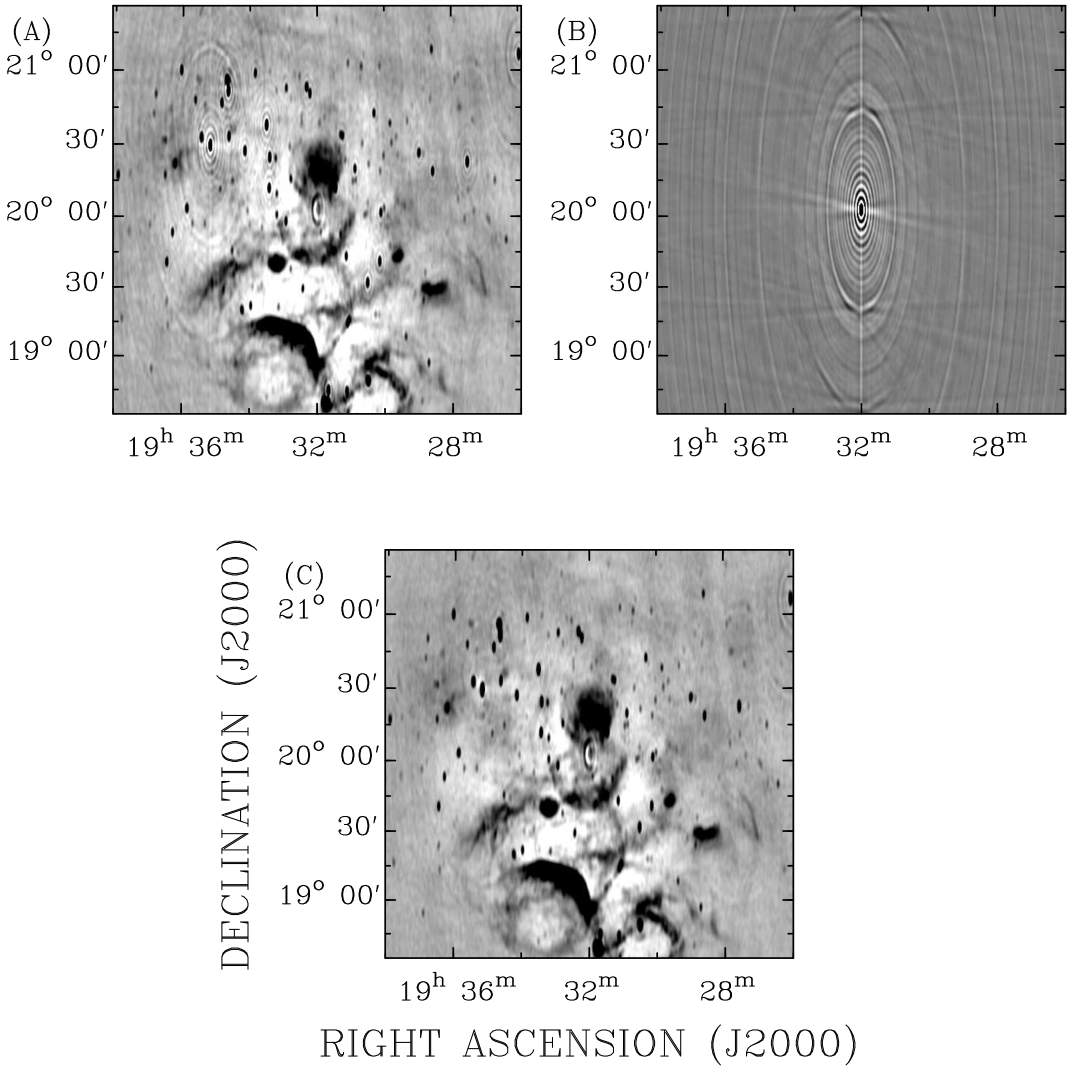

Figure 2.6: **Dirty and Clean Images at 1420MHz**

Images A and B show the dirty map and dirty beam respectively, while image C shows the clean map. Note that the grating rings, which are evident around point sources in the dirty map, have been successfully removed by the cleaning process. The greyscale limits of the maps are -5mJy/beam (white) to 5mJy/beam (black), while those of the beam are -0.01mJy/beam (white) to 0.01mJy/beam (black).

removed. This situation is remedied by the convolution of each clean component with a *clean beam* based on the dimensions of original synthesized beam.

The residual map must also be added back in, yielding:

$$I_{clean}(l,m) = \sum_{i=1}^{N} D_i G_{clean}(l - l_i, m - m_i) + I_R(l,m) \tag{2.28}$$

as the cleaned map. The resulting map is very much like the original. Its beam has the same "main" lobe (hence resolution) as the dirty beam, but no side lobes. The 1420MHz "dirty" map is contrasted with the "clean" map in Figure 2.6. Most of the ringing around the point sources has been removed, although some residuals remain around the bright source at the northwest of the map.

2.3.2 Self-Calibration Techniques

It is extremely convenient to have the means by which to calibrate data within the data themselves. For radio arrays containing more than four antennae, partial calibrations of both phase and amplitude can often be done using the data at hand. The process is called *self-calibration.*

The purpose of self-calibration is to reduce (or eliminate) the effects of calibration errors introduced by the atmosphere and electronics. This is done by creating a model of the sky brightness distribution from the data, then using that model to predict what the resulting $u-v$ data should have been. The model $u-v$ data are then used to "correct" (under certain constraints) the observed data. This process is performed iteratively until no further improvement is possible.

Recalling that the visibility, $V(u,v)$, is a complex function of a baseline (i,j), with antennae i and j at either end, it can then be expressed in terms of a visibility amplitude A_{ij} and a phase (the difference in phase between antennae i and j) θ_{ij}, such that

$$V_{ij} = A_{ij} e^{i\theta_{ij}}. \tag{2.29}$$

The visibility phase can be separated into two components, an "astronomical phase", ψ_{ij}, which is due to the offset in the position of the source from the pointing centre, and other error-based phase terms:

$$\theta_{ij} = 2\pi/\lambda[c\Delta\tau_e + c\Delta\tau_{atm}] + \psi_{ij} \tag{2.30}$$

where the first two terms (due to electronic and atmospheric effects respectively) can be combined to a single instrumental term, $\Delta\phi_{ij}$.

Similarly, the measured visibility amplitude can be expressed as

$$A_{ij} =\mid G_{ij} \mid\mid V(u_{ij}, v_{ij}) \mid \tag{2.31}$$

where G_{ij} is the complex gain of the interferometer:

$$G_{ij} =\mid G_{ij} \mid e^{i\Delta\phi_{ij}}. \tag{2.32}$$

To first order, G_{ij} is determined by observing a source of known position and flux density at the beginning and the end of the observing run. Residual errors in the gain are caused by variations over time, particularly in the phase delays due to the atmosphere.

The complex gain for baseline ij of the two antennae can be broken down to components for each individual antenna that make up the baseline, so that equation 2.32 becomes

$$G_{ij} = \sqrt{g_i g_j} e^{i(\phi_i - \phi_j)}. \tag{2.33}$$

Then the observed visibility is

$$A_{ij}e^{i\theta_{ij}} = \sqrt{g_i g_j} \mid V(u_{ij}, v_{ij}) \mid e^{i(\psi_{ij}+\phi_i-\phi_j)}. \tag{2.34}$$

If one has three antennae i, j and k, then the phase terms are

$$\theta_{ij} = \psi_{ij} + \phi_i - \phi_j \tag{2.35}$$

$$\theta_{jk} = \psi_{jk} + \phi_j - \phi_k \tag{2.36}$$

$$\theta_{ki} = \psi_{ki} + \phi_k - \phi_i \tag{2.37}$$

and the sum of the three visibility phase errors along the three different baselines gives the closure phase:

$$\chi_{ijk} = \psi_{ij} + \psi_{jk} + \psi_{ki} \tag{2.38}$$

which has no antenna based errors and is a purely astrophysical quantity!

Thus, by grouping the antennae in threes and iterating, the errors introduced by the electronics and the atmosphere can be removed from the visibility data. If some of the ψ_{ij} are known, then the closure phase can be used to derive the instrumental error terms. A similar exercise can be performed to correct for amplitude visibility errors, although a minimum of four antennae are required to define a closure amplitude.

Chapter 3

The Observations

3.1 The DRAO Data

The original data for this project were taken at DRAO in the period of 06-aug-92 to 23-sep-92. One baseline was re-observed on 07-jan-93. Continuum data at 408MHz and 1420MHz and HI spectral line data were taken using the synthesis telescope. HI data were also taken with the 26m single dish and their purpose is described in §3.3.3.

It is apropos here to discuss the differences between the HI line data and the 1420MHz (21cm) continuum. The HI line intensity is a measure of the photons released by the 21cm spin transition of the hydrogen atom and as such is a measure of the neutral hydrogen content of the ISM. The continuum data, however, are measures of all photons emitted at a continuum of energies over a broad band through thermal (free-free) or nonthermal (synchrotron) processes.

The continuum measurement at DRAO is contained in four bands centred on, but displaced on either side of, the central observing frequency. These bands are each 7.5MHz wide and are centred at ± 13.75MHz and ± 6.25MHz with respect to the central frequency, leaving a 5MHz gap about the central frequency to avoid contamination by the HI line emission of the Galaxy. The 408MHz data are taken with a single bandwidth centred on 408MHz. Some preliminary processing is done on the data by the staff at DRAO. This includes the removal of bad baselines and

Table 3.1: **DRAO Synthesis Data Specifications**

	408MHz (λ74cm)	1420MHz (λ21cm)
central frequency	408MHz	1420.406MHz
polarization	left circular	Stokes I (total intensity)
continuum bandwidth	4MHz	30MHz
system temperatures	150K	65K
field size (to 20% response)	8.1°	2.6°
synthesized beam (EW $\times$ NS)	$3.4' \times 9.8'$	$1.0' \times 2.92'$
measured rms noise	854mK(T_b)	79mK(T_b)

interference and the calibrations of flux density and phase.

Table 3.1 summarizes the specifications of the DRAO synthesis data. Estimates of the noise in the maps were performed by direct measurement of map fluctuations in a region of relatively low emission. The measured noise estimates were taken as the 1σ value for the purposes of distinguishing valid from spurious signals. The notation K(T_b) indicates that the quantity is a brightness temperature, as defined in §1.2.5.

3.2 Removal of an Artifact in the 1420MHz Continuum

Before standard processing was begun on the DRAO 1420MHz continuum data, it was necessary to address an artifact in the data which lay in an area of interest. The source of the artifact was a correlator[1] error introduced during observations. The error was unrecoverable. Figure 3.1 illustrates this artifact.

The process of removing the artifact can be summarized in three steps:

[1]The "correlator" both adds the delay τ_D appropriate to the baseline to bring the signals from two antennae into phase, and adds the cosine and sine signals together, outputting the complex visibilities.

- a model was obtained of the artifact from a second field;
- the local background was subtracted from the second field and visibilities created for the artifact; and
- a scaled version of the $u - v$ model was subtracted.

3.2.1 Obtaining an Artifact from a High-declination Field

After some discussion about how best to remove the artifact from the map, it was decided that an attempt would be made to model it using data gathered during the same epoch of a field well above the Galactic plane without a source present in the centre of the map. Because the error was baseline dependent, there was reason to believe that the resultant artifact in any image *should* have the same structure, although its flux density values would of course vary depending on whether or not there was a source at the centre of the field and how strong that source was.

The data required were obtained from DRAO archives. The field contained primarily extragalactic sources as well as the SNR DA530 and was observed between 11-sep-92 and 29-sep-92. The extragalactic field had a central position of RA $20^h 49^m 39^s$ and Dec $55°40'7''$. The field containing Casper has a declination of $20°6'0''$ at its centre. For east-west arrays, the resolution in declination (i.e. in the north-south direction) is a function of the declination, such that the resolution (EW $\times$ NS) is:

$$EW \times EW csc\delta \tag{3.1}$$

Thus, the resolution in declination of the extragalactic field was $1.22'$, a factor of 2.4 times better than the Casper data ($2.92'$).

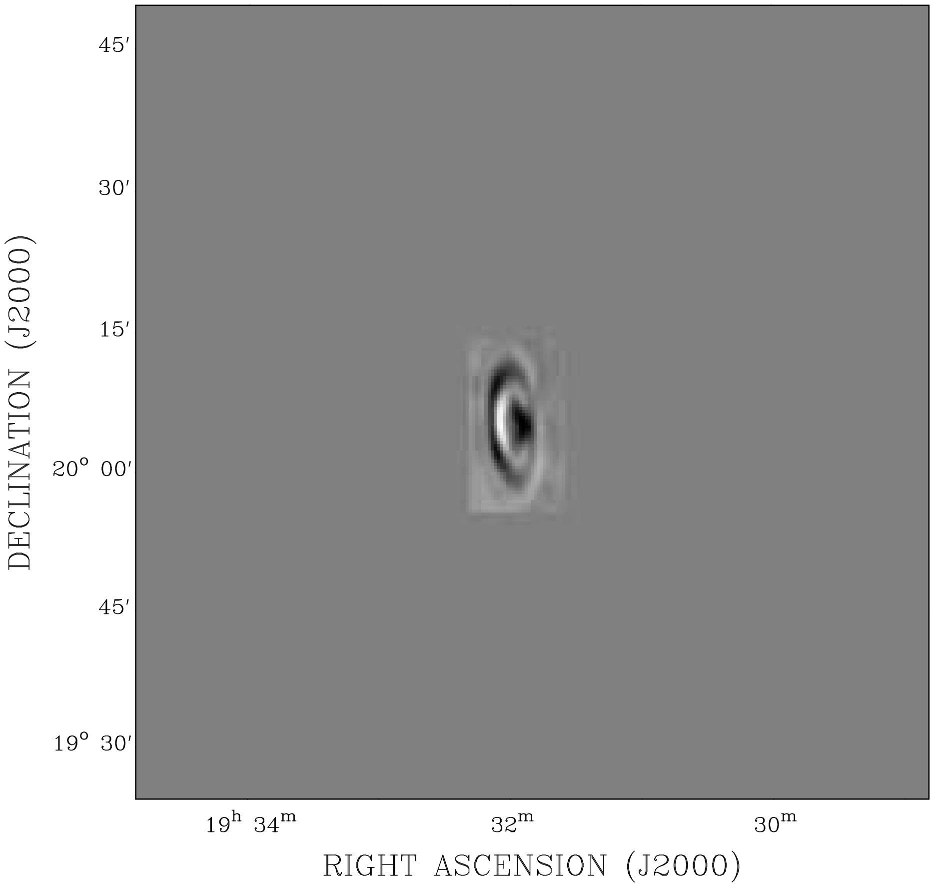

Figure 3.1: **The Model Artifact from the High-declination Field**
The artifact is visible at the centre of this map. Originally more circular in appearance, its elongation was a result of the regridding of the pixel size in declination to simulate the artifact's appearance at low declinations. This map is 256 x 256 pixels, with each pixel 20″ in size. Values below -10mJy/beam are white, while those above 10mJy/beam are black. All pixels about the central rectangle have a value of zero.

This fact meant that, initially, the artifacts in the two maps were not the same in appearance; the higher declination artifact was almost circular. Thus, it was necessary to stretch that artifact in declination. This was achieved by decreasing the pixel size in declination by a factor of 2.4. Additionally, the position angle of the artifact had to be altered by 35° from its initial value after stretching in order to make its orientation appear as much as possible like the artifact to be removed.

3.2.2 Removal of the Artifact from Casper

Although there was no source at the central position in the extragalactic map, there was background emission due to the presence of ambient radiation. In order to measure the artifact alone, a background subtraction was performed on the extragalactic map.

DRAO software exists which allows the subtraction of ambient background, which is estimated by a least-squares method fit to either the edges of a region specified by the user, or to the entire region enclosed. The background estimate is a "surface fit to a rectangular area of a map (with the sides of the rectangle parallel to the map edges) which is linear along any cut through it parallel to the X or Y axis" (Higgs, private communication).

The subtraction of the background is reasonably straightforward. Edges were defined about the adjusted bull's eye in the centre and the background was estimated according to the edges of the rectangle in Figure 3.1. From the background subtracted map, a map was created which contained only the artifact (Figure 3.1). All other pixel values outside the central rectangle were set to zero.

The intensity of the artifact varied between the two maps. Thus, to prevent over

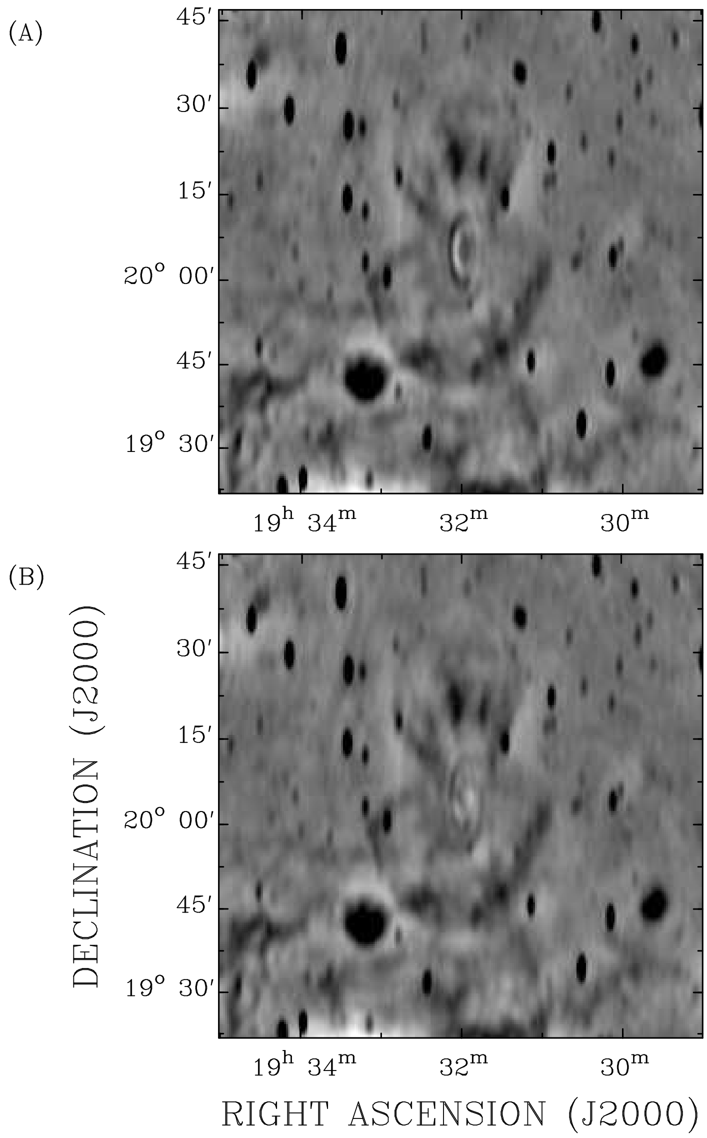

Figure 3.2: **Before and After Artifact Subtraction**
After artifact subtraction, the artifact can still be seen in map B; however, it is less obvious than in the original map, A. The maps have the same greyscale limits. The subtraction of the artifact was actually done in the $u-v$ plane. These maps are cleaned, 256 x 256 maps with grid spacings of 20″. Pixel values below -20mJy/beam appear white, while those above 15mJy/beam are black.

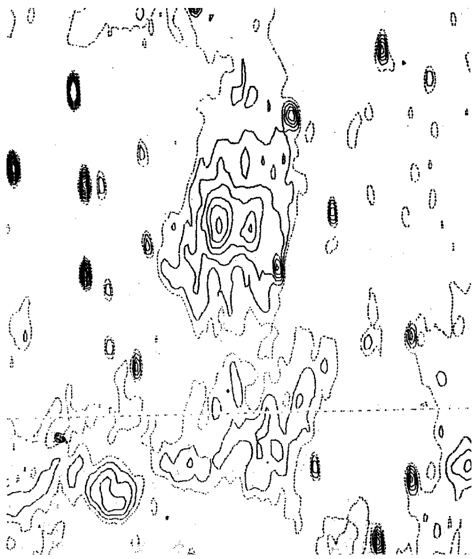

Figure 3.3: **1985 Map of Casper by J. Caswell**
This contour map is based on DRAO data of 1985, when the observatory had only four elements in its synthesis telescope. Nonetheless, the image shows that there is little emission in the region which contains the correlator error in the data used for this thesis. Thus, no major source of radio emission was being masked by the residue of the artifact. *(reproduced with permission of J. Caswell)*

or under-subtraction, intensity scaling was necessary. Visibility data were created from the model of the artifact, scaled, and subtracted from the visibilities as received from DRAO. Various values of the scaling factor were used in an attempt to find the best one. It was decided *by eye* that the removal of one fifteenth of the constructed visibilities was the most effective.

All subsequent data reductions were performed using these subtracted visibilities and maps. Figure 3.2 shows the appearance of the centre of the 1420MHz image before and after performing the subtraction.

As is evident from image B of Figure 3.2, there is a residual effect from the artifact in the subtracted map. Obviously, little reliable analysis could be performed on this region. There was some concern that the artifact could have covered a significant part of Casper. However, earlier DRAO images taken in 1985 by J. Caswell revealed that there was little structure within that region, as illustrated by Figure 3.3. However, the removal of the artifact was still a useful exercise, if only for the cosmetic improvement in the continuum map.

3.3 The Addition of DRAO Short-spacings

The data collected at DRAO have already been described above. The process of data reduction followed the same basic procedure explained in the previous chapter (i.e. the continuum synthesis data were cleaned and self-calibrated in the iterative process described in §2.3). Cleaning of the HI data is not done since the HI maps contain such weak flux densities that the first sidelobe of the dirty beam is below the noise level. Only a brief synopsis of the post-cleaning reduction follows, with exceptions regarding techniques or procedures which depart in some way from the standard practices or those which are particular to DRAO.

3.3.1 Gain Correction of the 408MHz Data

When data are taken at 408MHz at DRAO, care must be taken to account for the automatic gain correction (AGC) used by that telescope. The AGC operator system ensures that output to the detector electronics is maintained within a restricted voltage range during observations. This is necessary in order to avoid overloading the electronics when switching from observing sources to observing calibrators of typically much higher intensity.

The measures of the flux density and the system noise are typically expressed in terms of brightness temperatures. The antenna temperature, T_A, is related to the power received by the antenna in response to the flux density of the sky and the receiver temperature, T_{rec}, is the temperature which would be registered by the receiver even if it were observing a sky of temperature zero Kelvin. The power that produces T_{rec} is internal to the system, and only signals greater than T_{rec} by a significant margin can be considered detections. The AGC strives to keep

$$GAIN \times (T_A + T_{rec}) = constant. \tag{3.2}$$

For an observed field at 408MHz containing large amounts of flux density, the AGC system modifies the receiver gain between the calibrator observation and the object observation. This procedure introduces an error into the flux density scale of the derived map. A correction must be implemented to correct the flux densities to their true values.

In order to determine how much the data have been scaled by the AGC correction, some independent measure of the flux density of the sky at 408MHz must be utilized. The reference to the true sky brightness values is the low-resolution 408MHz all-sky survey of Haslam *et al.* (1983). Data are extracted from the survey to match the DRAO data for the object of interest and the calibrator(s).

Using these data, the average values over the DRAO beam map and survey image map are determined. The ratio of the averages can be used to determine what antenna temperature would have been measured by the DRAO dishes for the objects observed, had no AGC correction been applied. This yields the antenna temperature of the main beam; however, there will be power (hence some temperature) in the sidelobes of the antennae which must also be included.

The beam efficiency (ratio of the primary lobe to side lobe power) of the DRAO dishes is 0.66. Based on the average sky brightness at 408MHz of 34K (Haslam *et al.*), the temperature contained in the sidelobes of the DRAO dishes would be ~12K. Thus, the total expected antenna temperature measured at DRAO should be:

$$T_A(K) = 0.66 \times \frac{< Haslam >}{< DRAO >} + 12. \tag{3.3}$$

where the notation $<>$ indicates average sky brightness.

At the DRAO telescope, the gain has been varied to keep the output at their receiver relatively constant. Thus, the factor by which the observed data must be multiplied to correct the flux density scale is:

$$F = \frac{T_{A(source)} + T_{rec}}{T_{A(calibrator)} + T_{rec}} \tag{3.4}$$

where T_{rec} at DRAO is 90K.

3.3.2 Addition of Short-spacings in Continuum

Synthesis telescopes act as filters to large scale structure on the sky due to the omission of the smallest baselines (antennae can only be positioned so close together before accidents happen!). Only single dish antennae provide information about all the flux density from very large features on the sky. For synthesis telescopes, the value of the zero baseline flux density is zero which implies that the total flux density over the whole sky for the synthesis map must sum to zero. For this reason, maps constructed via aperture synthesis (as described in Chapter 2) will contain equal amounts of positive and negative flux density. In order to remedy this situation, data from synthesis telescopes are combined (when possible) with data from single dish telescopes in order to properly account for the large scale structure which is missing in the maps. The data provided by the single dishes are called “short-spacings”.

The short-spacings data at 1420MHz were extracted from a 1986 survey done using the Effelsberg 100m telescope (Reich *et al.*, 1986), which has resolution $9.4' \times 9.4'$. Short-spacings data at 408MHz were taken from the aforementioned all-sky survey of Haslam *et al.* (1983) of resolution $51' \times 51'$.

Since the $u-v$ coverage of the single dish short-spacing data overlaps that of the synthesis data, the maps cannot simply be added together. However, the technique for the addition of the two sets of data is reasonably straight-forward.

The short-spacings data have poorer resolution than the synthesis data. The angular resolution of the short-spacing data was used to determine the baseline for which the two maps should contribute equal weights to the final map. For example, at 1420MHz, the half-power width of the Effelsberg telescope's primary beam corresponded to a $u-v$ baseline of 34.4m. Using this information, the $u-v$ coverage was normalized to weight one everywhere to match the synthesized data (recall the nature of the sampling function discussed in §2.1.4) which required division by the Fourier transform of the short-spacings map coverage. The visibility data of the single dish were zeroed beyond baselines of 50m, and the weighting of the remaining baselines was tapered from 15m to 50m with these data contributing exactly half the flux density at 32.5m.

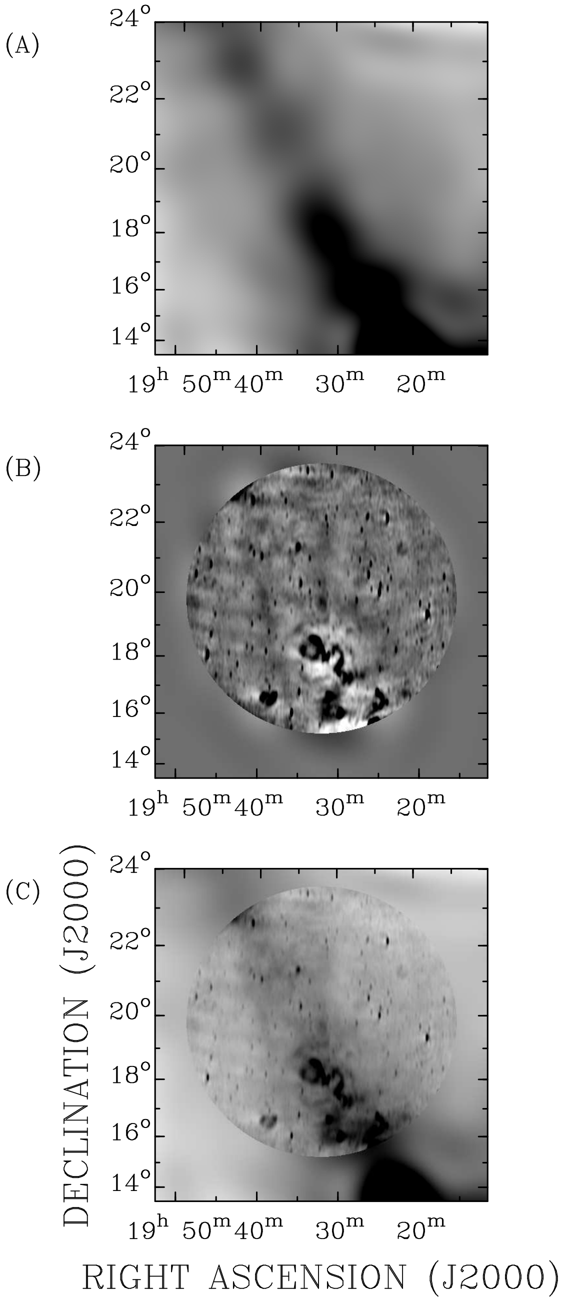

Figure 3.4: **Combination of the 408MHz Data**
Map A shows the short-spacing map extracted from the survey of Haslam *et al.* (1983). Values less than 20K(T_b) are white; values greater than 40K(T_b) are black. The Galactic plane is easily discernible in this image. Map B is the DRAO map which has value limits of -400mJy/beam and 300mJy/beam. Map C is the final combined map, with limits of 20K(T_b) and 170K(T_b). All three maps are 512 x 512, with grid spacings of $1'10''$.

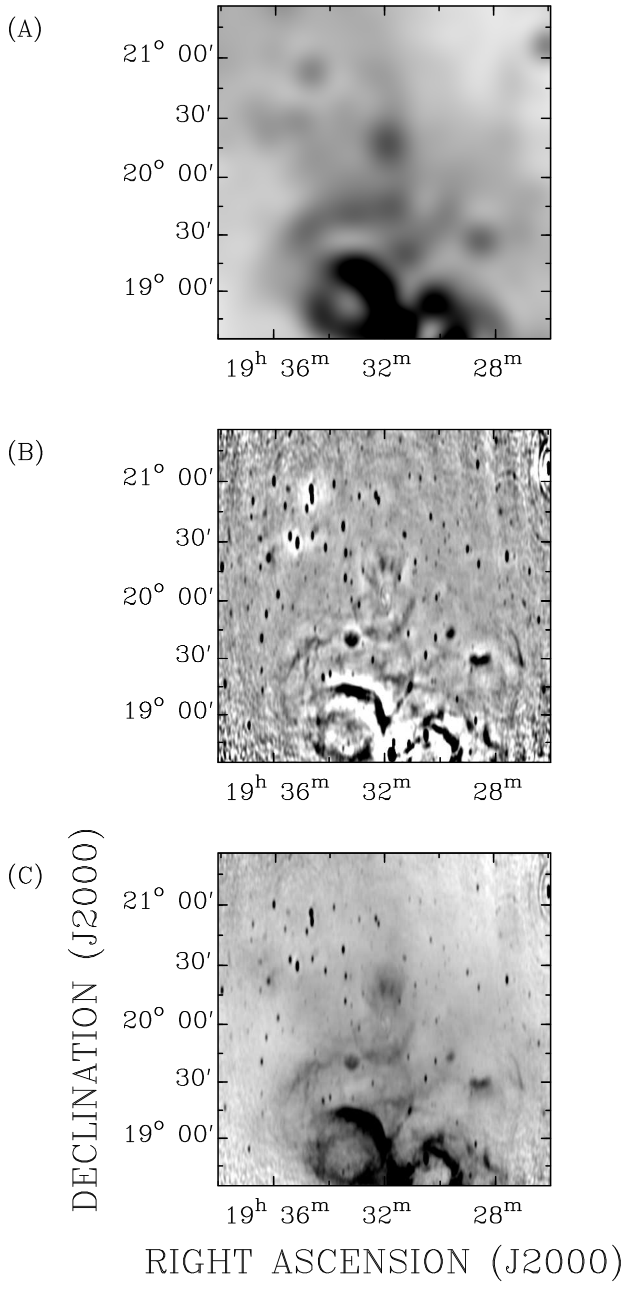

Figure 3.5: **Combination of the 1420MHz Data**
Map A shows the short-spacing map extracted from the survey of Reich *et al.* (1986). Values less than 9K(T_b) are white; values greater than 14K(T_b) are black. Map B is the DRAO map which has value limits of -10mJy/beam and 20mJy/beam. Finally, map C is the final combined map, with limits of 9K(T_b) and 15K(T_b). All three maps are 512 x 512, with grid spacings of 20″.

Before a similar exercise could be performed on the DRAO synthesis data, a correction had to performed for the attenuation of the primary beams of the elements of the array. The synthesis data visibilities all have equivalent weight (unity) due to the form of the sampling function described in §2.1.4. However, the synthesis data exhibit amplitude attenuation that increases with distance from the pointing centre. This attenuation was removed, yielding a so-called polar-corrected map. The visibility data for the polar-corrected map were then created by Fourier transformation. Baselines less than 15m were set to zero, and those greater than 50m were given weight one. At a baseline of 32.5m, the contribution of the DRAO data to the final map was exactly one half.

As a final step, the short-spacing and synthesis maps were added together. The original and final maps are shown in Figures 3.4 (408MHz) and 3.5 (1420MHz). The final maps contain no negative flux densities. The resolution of the final maps is identical to the synthesis data. The conversion factors for flux density to brightness temperatures are 62.79K(T_b)/(Jy/beam) for 1420MHz and 25.1K(T_b)/(Jy/beam).

3.3.3 The HI Line Data

Although HI line synthesis data are taken at both left and right hand polarizations, these were averaged together, since the radiation from the spin transition in the hydrogen atom has no preferential polarization. The data cube was then examined in order to single out bad channels and identify channels lacking in HI emission.

The line data reduction differed from that of the continuum, since the continuum had to be subtracted out of all the synthesis maps. The standard practice is to use the 1420MHz continuum map itself, but due to the presence of the correlator artifact, it was decided instead to construct a pseudo-continuum map from the channels at either end of the cube which were devoid of detectable HI emission. These were averaged to generate a pseudo-continuum map.

Since 18 maps were averaged together at the low end and 8 at the high end, the noise in the averaged maps was decreased by $\sqrt{18}$ and $\sqrt{8}$ respectively. Thus, the addition of two the maps to form the "pseudo-continuum" had to take into account additive coefficients:

$$pseudo - continuum = a_{18}x_{18} + a_8x_8 \tag{3.5}$$

where $a_{18} = (1+(8/18))^{-1}$, $a_8 = (1+(18/8))^{-1}$ and x_{18} and x_8 are the average maps of the 18 low end channels and 8 high end channels respectively.

The pseudo-continuum map and the true continuum map were compared in order to determine the magnitude of the scale difference in flux density known to exist between the continuum and line data. This was accomplished by examining the flux densities of six point sources. The peak value of each was measured simply by examining the map, and it was calculated that the true continuum map had larger values of flux density than the pseudo-continuum map by an average of 1.33. This meant that the subtracted HI cube had to be scaled by 1.33 to bring its flux densities into agreement with the true continuum. The resultant summed map was then subtracted from all the channels. The parameters of the HI cube are summarized in Table 3.2.

The subtracted maps were then added to the short-spacings maps in the same manner as the continuum data. The short-spacings observations were made to complement the synthesis measurements, having identical radial velocity and bandwidth

Table 3.2: **Specifications of the Synthesis HI Data Cube**

polarization	Stokes I (total intensity)
bandwidth	1MHz
field size (to 20% response)	$2.6°$
synthesized beam (EW x NS)	$1.74' \times 5.10'$
rms noise in the map centre	$1.17\mathrm{K}(T_b)$
central velocity	0 km/s
total 128 channel span	211km/s
channel separation	~1.65km/s
channel width	~2.6km/s

parameters. The short-spacings data for the HI line came from the 26m dish, meaning that the placement of the baseline limits for the combination of the synthesis and short-spacings data were different than those of the 1420MHz continuum. Only single dish data were used for baselines shorter than 7m while only synthesis data were used above 15m. The ratio of the data weighting was exactly one half at a $u-v$ baseline of 11m.

3.4 Other Frequencies

3.4.1 The Other Radio Data

Two additional frequencies of data were extracted from surveys for this analysis. The first data were those at 327MHz (discussed in §1.5.3) which reawakened the search for an SNR within Casper. A greyscale image of these data (Figure 1.2) is presented as Figure 3.6. This image has no short-spacing data, giving an upper limit of $0.45°$ on the structure which can be imaged by the 327MHz observations (Taylor *et al.*, 1992). The most important specifications of these data are summarized in Table 3.3.

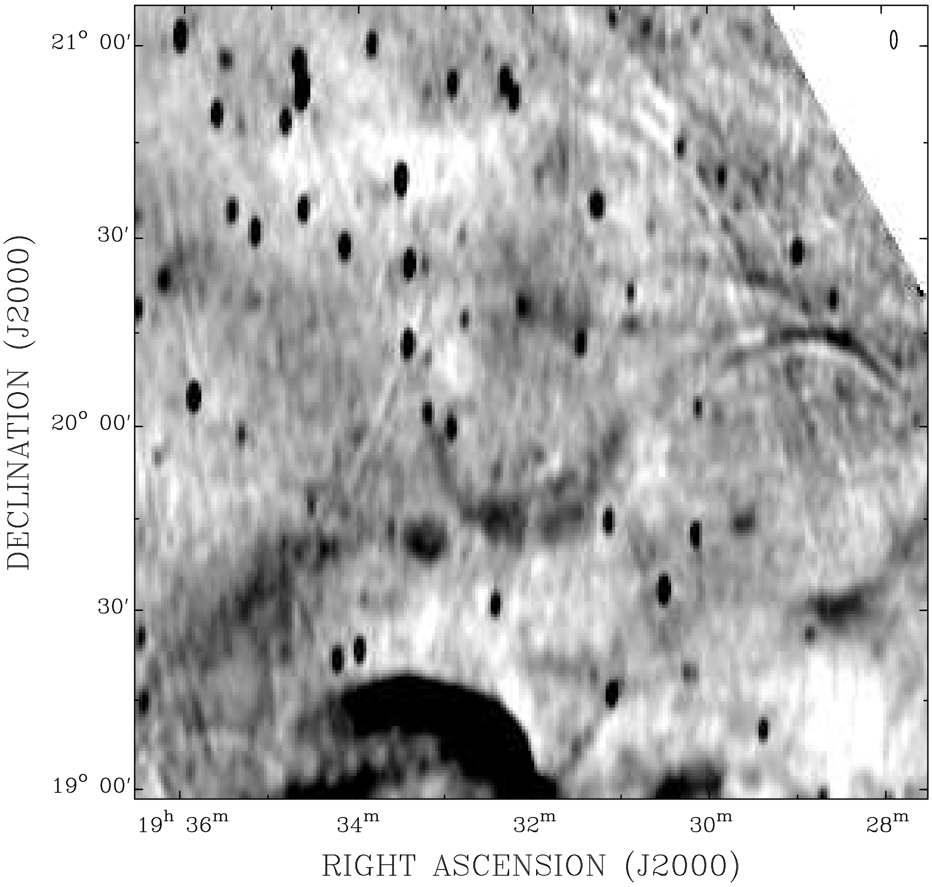

Figure 3.6: **The 327MHz Greyscale Image**

This image contains no short-spacings, so there are negative values in the map where extended structures are missing. The map is in units of brightness temperature, with values less than -20K(T_b) appearing white and values greater than 40K(T_b) appearing black. The values in the map range from ~-38K(T_b) to ~836K(T_b). Part of the SNR HC 40 stands out strongly in black at the bottom left. The beam size is represented by the ellipse in the top right corner of the image. *(Taylor* et al., *1996)*

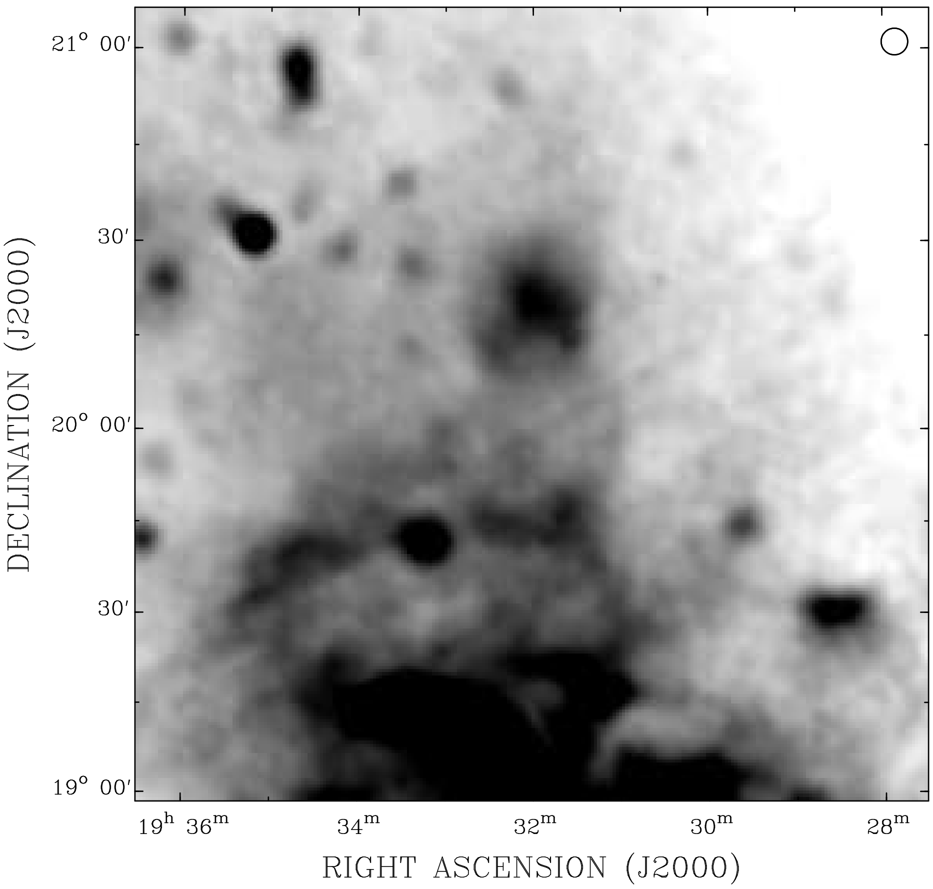

Figure 3.7: **The 2695MHz Greyscale Image**
This map was extracted from a 1984 survey done with the Effelsberg 100m telescope. Thus, it is a measure of the total flux density of the sky, and there are no negatives in the map. Values less than zero appear white and values greater than 0.6K(T_b) appear black. The map values range from zero to ~2.1K(T_b). The beam size is represented by the circle in the top right corner. *(Reich* et al., *1984)*

Table 3.3: **Specifications of Alternate Radio Frequencies**

	327MHz (λ92cm)	2695MHz (λ11cm)
central frequency	326.375 MHz	2695.0
bandwidth	2.5MHz	80MHz
resolution (EW x NS)	$1' \times 2.92'$	$4.27' \times 4.27'$
rms noise (measured)	4K(T_b))	24mK(T_b)
T_b/S_ν	1.08K/(mJy/beam)	2.57K/(Jy/beam)

The second frequency was 2695MHz. This map was obtained from the survey of Reich *et al.* (1984) As for the 327MHz data, the parameters of the data are in Table 3.3, and Figure 3.7 contains a greyscale image of the extracted region containing Casper.

3.4.2 Far Infrared Data from IRAS

The best far-infrared data available were gathered in 1983 by the Infra-Red Astronomical Satellite (IRAS) which was originally designed to detect point sources. The far-IR regime suffers greatly from atmospheric extinction; thus, space-based observations are necessary. The satellite surveyed the sky in large scans, and the amount of redundancy in the data has permitted it to be reprocessed to reveal features about extended IR emission for which it was never originally designed.

Reprocessing of the IRAS data is done primarily at the Image Processing and Analysis Centre at Caltech, using a Maximum Correlation Algorithm (Aumann *et al.*, 1990) called HiRes. HiRes enhances resolution up to 4-5 times that of the original maps for very bright sources. More typically, improvements of 2-2.5 times are obtained. The reprocessed resolutions are included in Table 3.4 as well as the

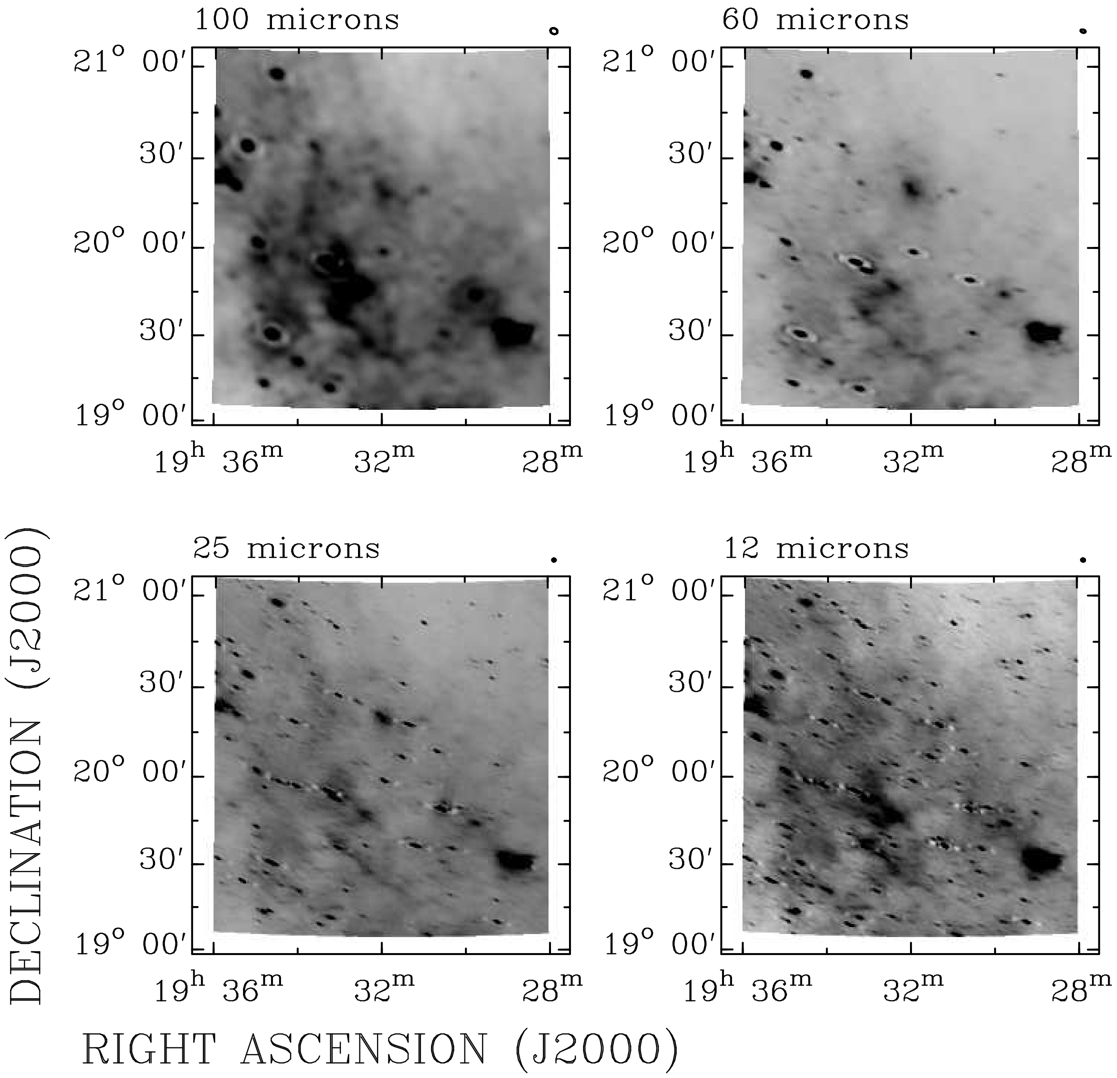

Figure 3.8: **The IRAS HiRes Data**
The four available IRAS bands were obtained. The 25μ and 12μ data have been smoothed so that all the maps could be gridded to the same pixel size while preventing undersampling. The resolutions of the data are given in Table 3.4. The beam sizes are included to the upper right of each image. The 100, 60, 25 and 12μ images have white limits below 80, 0, 40 and 25MJy/steradian and black limits above 400, 150, 65 and 40MJy/steradian.

Table 3.4: **Specifications of IRAS Data**

Band	HiRes Resolution	Smoothed Resolution	Position Angle (N of E)
100μ	$2'25'' \times 1'55''$	n/a	$335°$
60μ	$1'40'' \times 1'$	n/a	$340°$
25μ	$1' \times 30''$	$1' \times 1'$	$330°$
12μ	$1'10'' \times 30''$	$1'10'' \times 1'$	$335°$

position angles of the beams. The angles represent the angles north of east of the major axes of the beams. The beams are illustrated to the top right of the HiRes images in Figure 3.8.

The HiRes data do not have constant resolution over the entire map (50% variations in beam size are possible in all four wavelengths across disparate areas of the maps). The resolutions quoted in Table 3.4 are appropriate for the central region of the maps.

The offsets in positions from the HiRes processed data to those in the *IRAS Point Source Catalogue* are $9'' \pm 5''$ at 60μ and $8'' \pm 4''$ at 100μ, and the flux densities are estimated to be accurate to 12% at 60μ and 20% at 100μ as compared to point sources in the catalogue (Fich and Tereby, 1996). The HiRes algorithm is most successful in regions with strong signal. The flux density uncertainties are attributed mainly to difficulties in background estimation and exceed the rms noise in the maps.

An adaption to the HiRes algorithm has been developed which has eliminated most of the artifacts created by the reprocessing (Cao, 1996). The only remaining artifacts in the HiRes data are depressions created around strong point sources. These stand out in the images of Figure 3.8.

To check that the coordinate grid for the HiRes image was correct, the positions of six of the brightest point sources in the 12μ map were measured and checked against those in the *IRAS Point Source Catalogue*. The sources were located in the catalogue well within the catalogue's quoted errors.

3.4.3 The Palomar Sky Survey

The optical image (at 600THz, or 500nm) was obtained from the Palomar Sky Survey[2] done in 1950. These data have been checked for possible emission related to Casper's northern region in the past (Crovisier, 1974; Reich *et al.*, 1986) and none has been noted. However, the image is included here for completeness. The original image obtained was a $1.5^\circ \times 1.5^\circ$ image with a grid spacing of $10''$. However, it has been regridded to the same scale as the images at other frequencies in Figure 3.9.

Although there is no distinctive emission from the centre of the map where Casper is located, there is a lack of emission to the south east of Casper where there is a large complex of both radio and IRAS emission.

[2]Based on photographic data obtained using Oschin Schmidt Telescope on Palomar Mountain. The Palomar Observatory Sky Survey was funded by the National Geographic Society. The Oschin Shmidt Telescope is operated by the California Institute of Technology and Palomar Observatory. The plates were processed into the present compressed digital format with their permission. The Digitized Sky Survey was produced at the Space Telescope Science Institute (ST ScI) under U. S. Goverment grant NAG W-2166.

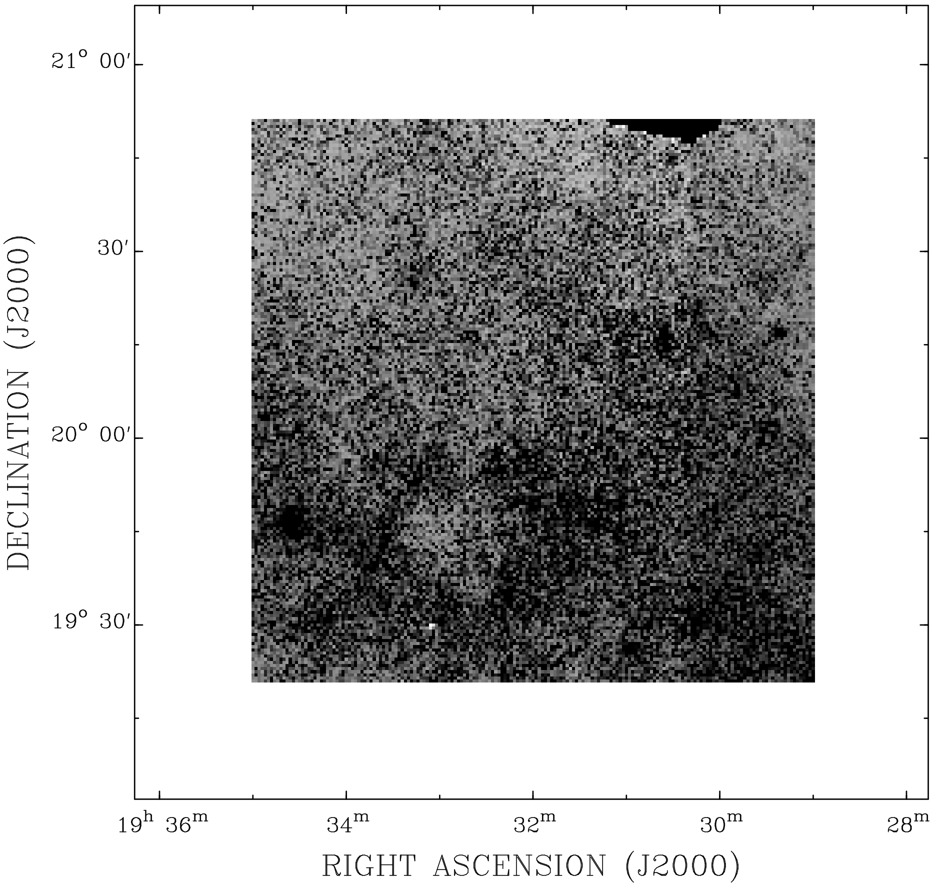

Figure 3.9: **Optical data from Palomar Sky Survey**
As for the other maps in this section, black indicates heightened emission (pixels above 4600 counts) while white indicates an absence of detected emission (less than 1500 counts). The map is 256 x 256 with a grid spacing of 30″ which is a significant degradation of the resolution of the original image. *(Digitized Sky Survey)*

Chapter 4

Analysis of the Continuum Data

As discussed in §1.2.5, the spectral index is a key factor in the identification of SNR, since all those known emit synchrotron radiation. The primary data analysis of this project was the measurement of flux densities at multiple frequencies for different components of Casper, thus identifying which are the thermal and nonthermal components of the object. Also, the IRAS data allowed us to obtain some sense of how dust is distributed throughout Casper, as well as allowing further differentiation between HII regions and SNR, which can both create strong emission in the radio regime.

4.1 Determination of Integrated Flux Densities

The radio spectral indices were determined for different regions: the left eye, right eye, both eyes (G55.6+0.7), smile and Casper as a whole (formerly G55.2+0.5). The three new regions are indicated on Figure 4.1.

Calculation of α requires that flux densities at multiple frequencies be measured. The evaluation of a region's flux density was accomplished by summing the pixel values within a polygon enclosing the region after removing background emission estimated from the map values on the polygon boundaries. Ideally, in the case of an extended feature on a uniform background, a series of larger and larger polygons could be constructed, until the flux density ceased to change. At this point, one

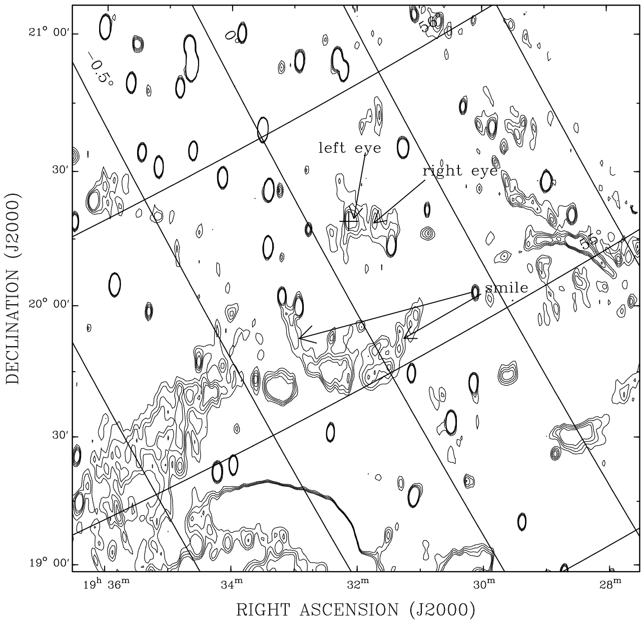

Figure 4.1: **The Components of Casper**
This 327MHz image of Casper indicates roughly the regions singled out for individual analysis. This was a prudent approach since there was no reason to believe that the regions were related to each other. The cross marks the pulsar position within the "left eye" region. The superior resolution of the 1420MHz and 327MHz data made the distinction of Casper's components possible at both frequencies. The contours of the map are 10 to 25K(T_b) in steps of 5K(T_b).

could assume that all the flux density of the object had been enclosed by the largest polygon.

The difficulty in our region is that the polygons cannot be made larger and larger without running into a disparate region of Casper. Thus, enclosure of a reasonable area had to suffice. This made the use of the same polygons at each frequency a necessity . The polygons were based on the morphology at 1420MHz, although their compatibility with the other frequency maps was checked before any calculations were performed.

4.1.1 The Removal of Compact Sources Prior to Analysis

Although all of the images presented include point sources (most of which are external to our Galaxy), for the purposes of data analysis, as many as possible within Casper were removed. Typically, the compact sources are the strongest sources of flux densities in the maps; thus, in cases where they cannot be removed, the flux densities within those regions will invariably be overestimates. Such sources were most successfully subtracted from the 1420 and 327MHz radio maps. These data had the best resolution in the radio and as such, the point sources were more distinct. At the other two radio frequencies, the larger beam sizes caused blending of point sources with one another and with extended structures. This effect made point source subtraction from the 2695 and 408MHz data infeasible, and it was not done at these frequencies.

The point source removal was done by identifying the source to be removed and defining a "source box" about the centre of the point source. A gaussian was then fit to the source identified within the box and a subtraction of all sources which could be fitted was done. For sources in close proximity to one another, one source was fit at a time until all the sources were removed satisfactorily.

The subtraction of point sources from the IRAS data presented a different problem. Since the beams of the IRAS data are not gaussian and the removal of sources is by gaussian fitting, the subtractions tend to leave residuals which scale with the brightness of the source being subtracted. For the strongest point sources, the peak residual remaining was $\sim$10% of the original flux density, while depressions (with

Table 4.1: **Contributions of Point Sources within Casper**

Frequency (MHz)		Total Flux Density (mJy)	
	Smile	Eyes (G55.6+0.7)	Casper (G55.2+0.5)
327	253 ± 8	84.0 ± 0.2	551 ± 21
408	228 ± 7	79.0 ± 0.2	480 ± 17
1420	81 ± 5	54.0 ± 0.3	193 ± 14
2695	51 ± 3	44.0 ± 0.3	132 ± 8

respect to the local background) of comparable intensity ring the residual peak. The net effect of the residuals in a summation over a polygon will be less than 10%, since the positive and negative contributions with respect to the background will cancel out somewhat. Despite the fact that the subtractions were not ideal, they did reduce the flux densities substantially, meaning that the integration over wide areas of pixels was more accurate than it would have been had the subtractions not been performed.

The total flux densities removed for the four fields are summed in Table 4.1 for the various regions of Casper. Flux densities were calculated by the gaussian fits of the subtraction process for 1420MHz and 327MHz. The sums for 2695MHz and 408MHz point sources are extrapolated from those measured at the other frequencies. The uncertainties on the extrapolated flux densities are due to the uncertainties in the flux densities at 1420MHz and 327MHz, assuming no uncertainty on the spectral index determined from those values.

Could the Eyes Be Point Sources?

The compact size of Casper's eyes at 327 and 1420MHz made an attempt to fit them as 2-dimensional gaussians a possibility. Such a fit yields an estimation of both flux density and angular size.

The software was able to fit a gaussian to the right eye at 327MHz. The value obtained was 30.1 ± 2.5mJy for a linear background subtraction. After deconvolution of the beam, the size estimate of the right eye was $3.7 \pm 0.3' \times 1.2 \pm 0.1'$ at a position angle (major axis angle north of east) of $89.7°$. The left eye could not be fit with a gaussian. This was not surprising, since it is asymmetric with respect to the peak brightness temperature, especially at 327MHz.

Both objects are resolved and therefore are not likely to be background extra-galactic radio sources, but rather part of the extended plateau of emission on which they sit.

4.1.2 Determination of the Flux Density of the Pulsar

It should be reiterated that the pulsar J1932+2020 is located within the contours of the left eye. Thus, the flux density of the pulsar will be contained in any measurement made of that region. In order to remove the contribution of the pulsar from the total flux density of the left eye, the spectrum of the pulsar had to be known. The most recent measurement of the spectrum of the pulsar was made by Lorimer *et al.* (1995) based on three years worth of data measured at three frequencies (408, 606 and 1408MHz).

Using their flux density measurement and spectral index, the flux densities at 327 and 1420MHz were extrapolated using equation 1.10, from the closest measured data value and Lorimer *et al.*'s spectral index of -2.5 ± 0.2. Table 4.2 contains the calculated values for the pulsar, as well as the values measured at the pulsar's position on our maps. Obviously, the contribution of the pulsar's flux density to the

Table 4.2: **Extrapolated and Measured Flux Densities of J1932+2020**

	S_{327} (mJy)	$T_{b(327)}$ (K)	S_{1420} (mJy)	$T_{b(1420)}$ (K)
PSR	49.6 ± 12	53.6 ± 13	1.18 ± 0.4	0.07 ± 0.02
maps	40.5	43.76	210.7	13.23

total observed is much less significant at 1420MHz than 327MHz.

Since the best fit flux density at 327MHz was actually greater than the pixel value at the position of the pulsar (this was also the local peak for the left eye) and the range of possible flux densities was substantial, it was decided to take the most conservative approach and attribute all the 327MHz flux density to the pulsar. Thus, values of 40.5mJy at 327MHz and 1.18mJy at 1420MHz were subtracted from the integrated flux densities once they had been obtained.

4.1.3 Integration over Polygons

Many polygons of different vertices were constructed for each region. This was essential to obtain independent estimates of the background. The estimation of the background is based on the edges of the polygon, which are different in each case. Since the sums above the background were occasionally less than 5% of the total sums, accurate estimates of the background were essential. The background emission was high due to the proximity to the Galactic plane. The number of polygons used for each region are included in Table 4.3.

The sums above background of the radio maps were in units of brightness temperature, which were converted to Janskys using the solid angle of the beam and the frequency of the observation per equation 1.19.

Table 4.3: **Flux Densities for Different Regions of Casper**

Region	# polygons averaged	S_{2695} (Jy)	S_{1420} (Jy)	S_{408} (Jy)	S_{327} (Jy)
left eye	13	—	0.090 ± 0.012	—	0.10 ± 0.010
left eye (no pulsar)	13	—	0.088 ± 0.012	—	0.057 ± 0.013
right eye	11	—	0.037 ± 0.005	—	0.038 ± 0.008
smile	14	0.27 ± 0.05	0.64 ± 0.11	0.25 ± 0.12	0.98 ± 0.15
eyes	7	1.0 ± 0.1	1.3 ± 0.1	1.2 ± 0.1	0.96 ± 0.12
Casper	12	1.7 ± 0.1	2.9 ± 0.3	2.4 ± 0.3	2.8 ± 0.3

Once the radio flux densities had been obtained, the averages and standard deviations of all the polygons for each region were determined. The standard deviation was taken to be the 1σ error in the flux density. Table 4.3 shows the flux densities for each region at the four radio frequencies. All values are point source subtracted. In all cases, the variations in the flux densities from the polygons far exceeds the inherent noise in the maps. Therefore, background estimation is the largest contributor to the uncertainties in the measurement of flux densities.

The subtraction of the extrapolated point source flux density of the smile at 408MHz resulted in the subtraction of approximately 50% of the total flux density. This contrasts with subtractions of up to 20% for the other frequencies. The poor resolution of the 408MHz data meant that a substantial amount of the flux density must have been excluded from the polygon. For this reason, the 408MHz measurement was not used for the analysis of the smile.

Since the flux density for the right eye had already been estimated by gaussian fitting, an independent check of the polygon method was possible. The values obtained for the right eye at 327MHz in Table 4.3 are consistent with that of the gaussian fit.

In several cases, flux densities were not measured for all of the available frequencies. In all cases, the omissions in Table 4.3 were due to an inability to reconcile the need for using the same polygons for all the frequencies with variations in the sizes of the beams. For example, the large beams of the 2695 and 408MHz made distinction of the two eyes impossible. Even if the polygons were used, a different amount of the flux density would most certainly have been measured than for the 1420 and 327MHz images, which had the same high resolution.

An additional note concerns the 327MHz flux densities of the eyes, smile and Casper regions. These integrated flux density values can be treated as lower limits owing to the lack of short-spacings in this data (see §3.4.1). This effect would be most relevant to the measurements of Casper as a whole, since the polygons which enclose it are on the order of $0.5° \times 1°$ in size.

Here, it is noted that a previous measurement of the flux density of Casper yielded a value of 5.8Jy at 327MHz (Taylor *et al.*, 1992), while the total flux density measured in this analysis yielded $\sim$2.8Jy. Since the sum of all the point sources noted within the Casper region is only $\sim$0.5Jy, the discrepency cannot be due to an inclusion of a point source in the former measurement. Additionally, the polygons seem to have been taken over roughly the same region. It is most likely that the difference arises from the effectiveness of the methods used for background subtraction. The 1992 background estimation was not performed by fitting to a series of polygons. The background was estimated off source and restricted to a fit on a rectangular contour. Given the variations in the Galactic background, this method is not as effective as that used for this study (Wallace, private communication).

Table 4.4: **Spectral Indices for Different Regions of Casper**

Region	α
left eye (with pulsar)	-0.82 ± 0.13
left eye (without pulsar)	0.30 ± 0.13
right eye	-0.013 ± 0.12
smile	-0.53 ± 0.26
eyes	0.041 ± 0.09
Casper	-0.22 ± 0.10

4.2 Calculations of Spectral Indices

4.2.1 Mean Spectral Indices

Based on equation 1.10, the mean spectral indices over the independent regions of Casper were determined by a weighted linear regression on the applicable integrated flux densities as given in Table 4.3. The error estimates are 1σ. Plots of flux density versus frequency are shown in Figures 4.2, 4.3 and 4.4. Since the spectral indices of the individual eyes were based on only two data points, no plots were generated for these two regions.

Note that the 408MHz flux density is not included in Figure 4.2. The omission was based on the fact that relevant flux density was excluded from the polygons contructed for this region due to the large size of the beam. The beam at 408MHz was by far the poorest in our data sample (see Table 3.1), and this led to blending of several features in the region of the smile, particularly between the smile region and the circular region to the southeast of Casper. Defining a larger polygon would have further corrupted the measurements, while defining a smaller one would have meant knowingly neglecting even more flux density. In the interests of establishing

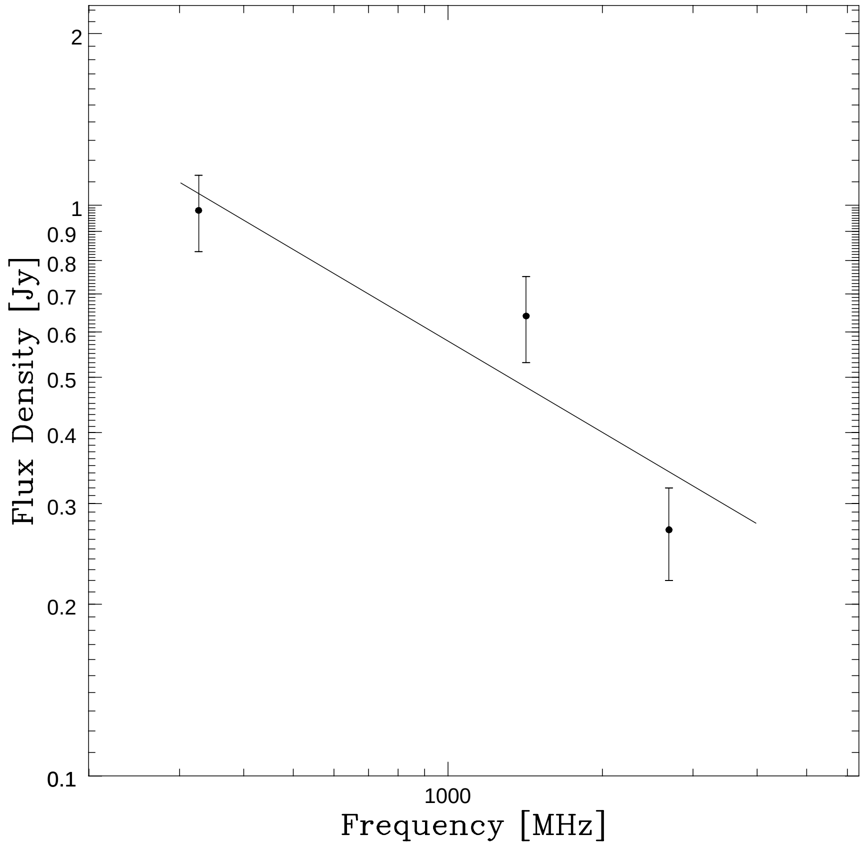

Figure 4.2: **Spectral Index of the Smile**

The spectral index plot shows the average flux density values after all point source subtractions with the error bars indicating the standard deviation. The line indicates a spectral index value of -0.53. A weighted linear regression on the plotted values yields an uncertainty in the spectral index of 0.26.

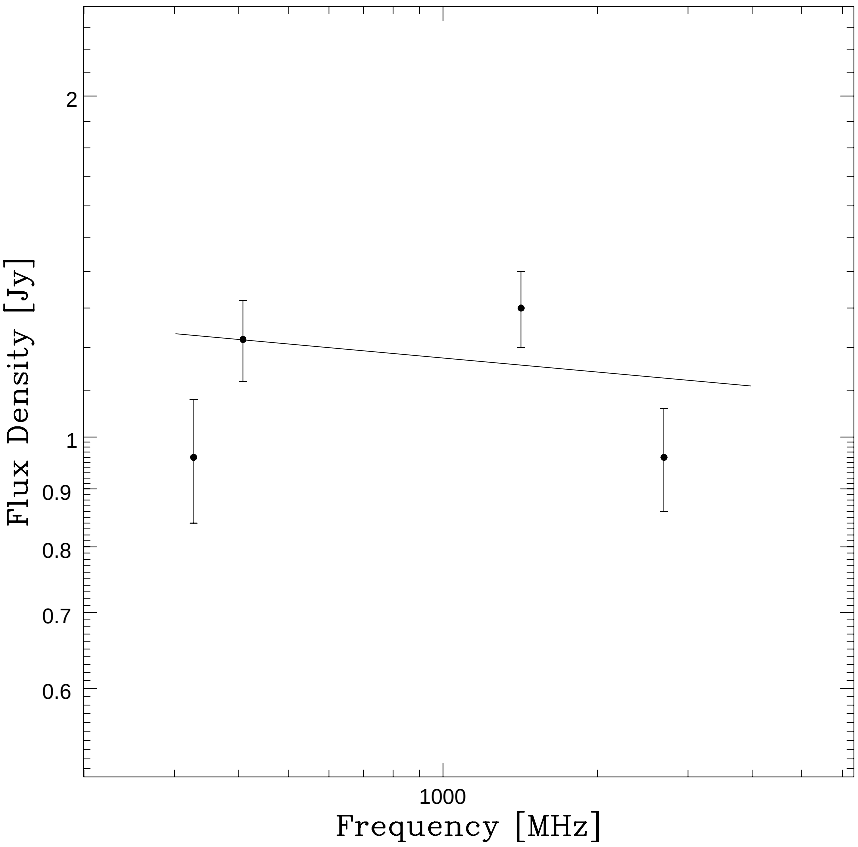

Figure 4.3: **Spectral Index of the Eyes (G55.6+0.7)**
The spectral index plot shows the average flux density values after all point source subtractions with the error bars indicating the standard deviation. The linear fit indicates a spectral index value of -0.041. A weighted linear regression on the plotted values indicates an uncertainty in the spectral index of 0.09.

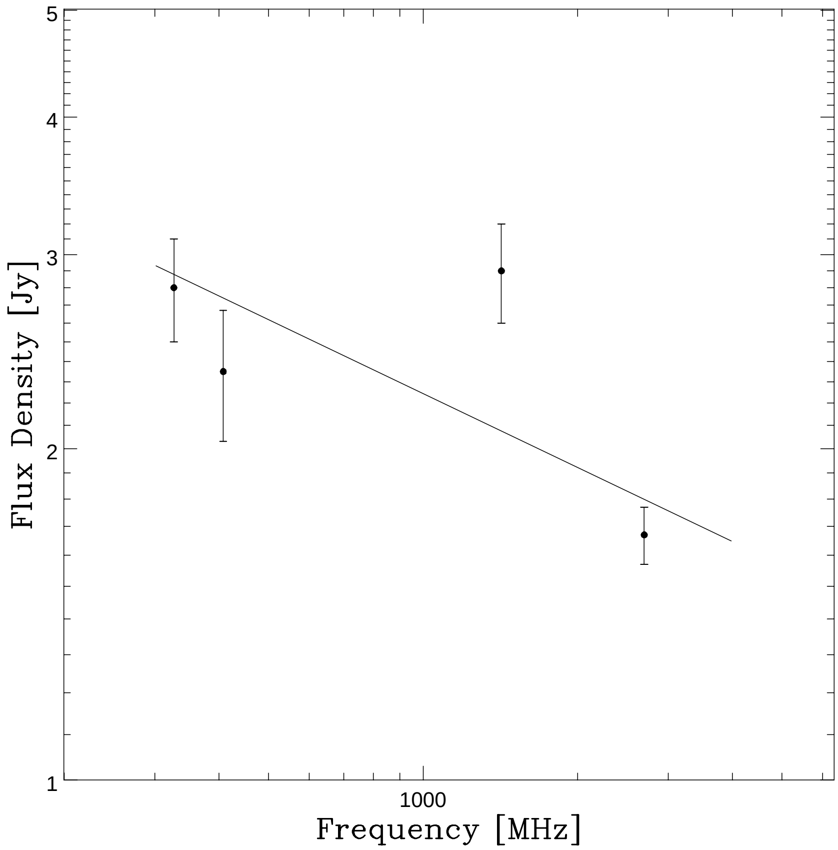

Figure 4.4: **Spectral index of Casper (G55.2+0.5)**
The spectral index plot shows the average flux density values after all point source subtractions with the error bars indicating the standard deviations. The linear fit indicates a spectral index value of -0.22. A weighted linear regression on the plotted values indicates an uncertainty in the spectral index of 0.10.

the flux density of the smile alone, the 408MHz measurement was discarded. The remaining flux densities were used to determine the spectral index of the smile to be -0.53 ± 0.26 which is approximately the average spectral index of a shell-type SNR (see Table 1.1).

All of the frequencies were used for the calculations of the spectral indices of the eyes and Casper as a whole. These regions are worthy of examination since they are the regions most comparable to regions defined in previous studies. As shown in Table 4.4, the analysis of the integrated flux densities has yielded a nonthermal ($\alpha < -0.1$) spectral index for the smile of Casper. Casper as a whole also has a nonthermal spectral index. Since this region is more than just the eyes and the smile, this suggests there could be an underlying diffuse component of nonthermal emission. The suggestion of a nonthermal spectral index for the left eye is removed with the pulsar, leaving a spectral index which could be either thermal or nonthermal.

These results are consistent with those of Reich *et al.* (1986) regarding the northern region of Casper. The spectral index, although ambiguous with respect to the nonthermal bound of -0.1, is approximately flat and agrees within 1σ with their value of $\alpha = 0$. The spectral index is consistent with that of an optically-thin thermal emission nebula (see §1.2.5). The measurement of a nonthermal spectral index for the entire region of Casper, $\alpha = -0.22 \pm 0.10$, is consistent with the tentative conclusions of Taylor *et al.* (1992) who suggested a spectral index of -1.49 ± 0.49 based on the measurements summarized in §1.5.3. The measurement of the flux density at 327MHz is an underestimate as discussed in the previous section. Thus, the true spectral index could in fact be more nonthermal than the calculated value.

While this analysis shows that the emission observed from the smile cannot be originating from a thermal source, the integration process gives a result that is "averaged" over the region. A more detailed analysis of the spectral indices is justified in order to determine how the spectral index varies over the smile.

4.2.2 Spectral Index Maps

A spectral index map differs from the analysis above in that it yields a pixel by pixel analysis of a given region or an entire map. It is essentially a ratio map generated with the logarithms of two flux densities to produce an estimate of α according to equation 1.10. The long and short wavelength maps used were the 327MHz (92cm) and the 1420MHz (21cm) respectively .

Unlike the calculation of the flux densities from the integrated polygons, this method did not include any background subtraction in the software. Thus, background subtraction was done on the maps before the ratios were taken. The background subtractions were done based on two separate regions: the eyes and the smile. The subtraction method described in §3.2.2 was applied to rectangular polygons enclosing each region separately. This produced different background maps and background subtracted maps for each feature.

The removal of the pulsar's flux density from the region of the left eye was not as straight forward from the maps as it was from the integrated flux density values. The pulsar's flux density had to be convolved with the beam in order to give a true representation of how it would appear on the image. This was done by creating maps with a gaussian the size of the beam centred on the location of the pulsar with a peak value appropriate to either the 1420 or 327MHz flux density. The same values were used as for the integrated flux densities: the peak in the map for the 327MHz map and the extrapolated flux density of the pulsar at 1420MHz. Once the pulsar subtracted maps were made, the spectral index maps were generated.

Since a spectral index is derived from the ratio of two images, regions of the 327MHz image with no or low signal will produce spurious signals of potentially very large amplitudes. In order to avoid such regions in our spectral index maps, spectral indices were calculated only for pixels with values greater than 12K(T_b) in the 327MHz map, which is the 3σ detection limit.

The input maps were in units of brightness temperature; therefore, the boundary values of the spectral indices are different from those calculated using flux densities. As discussed in §1.2.5 with respect to brightness temperature spectral index, values greater than 2.1 indicate a nonthermal source of emission for $T_b \propto \nu^{-\alpha}$. Figures 4.5 and 4.6 are the spectral index maps for the eyes and smile, respectively.

The spectral index maps illustrate how the nonthermal emission is distributed across Casper's eyes and smile. They confirm the results of the average spectral indices calculated in the previous section. The eyes can be dismissed as a source of nonthermal emission. The previous measurements of a nonthermal spectral index by Crovisier (1974) were dependent on a 4850MHz data value which was measured with such a large beam that some flux density could have been included from the southern component of Casper. *These data establish that the smile is the only clear source of nonthermal emission within Casper.*

The fact that the spectral indices vary across the smile could imply that different mechanisms are responsible for the radio emission at the different positions (i.e. thermal versus nonthermal). However, the entire smile could be nonthermal as well, since equation 1.9 does not place any constraints on the spectral index observable from a

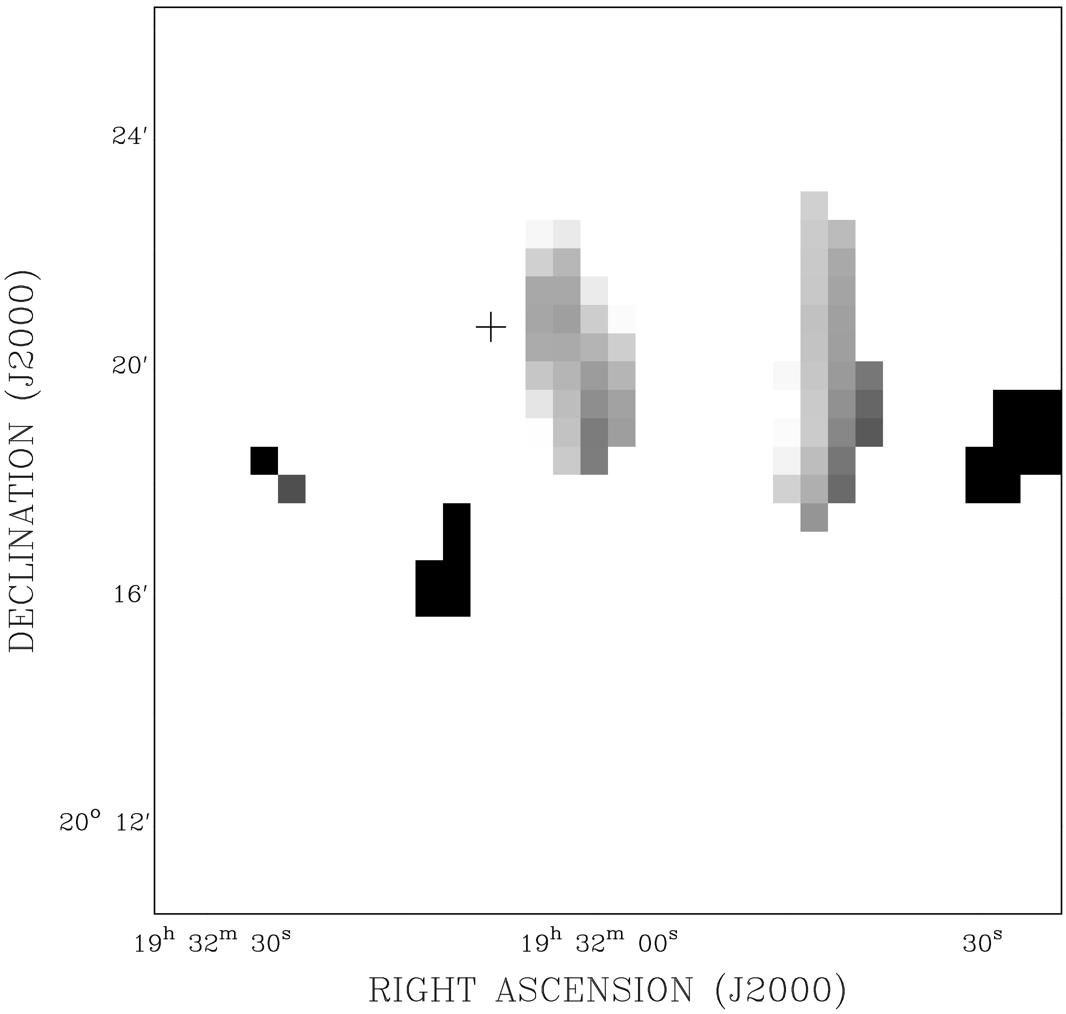

Figure 4.5: **Spectral Index Map of Casper's Eyes**
This greyscale map illustrates that no regions of the eyes showed a nonthermal spectral index following the subtraction of the pulsar. Pixels with spectral index values less than 1.7 appear white while those above 2.2 (distinctly nonthermal) appear black. The only nonthermal values are believed to be artifacts arising from the background subtractions of the maps. The subtraction of the pulsar meant that no pixels surrounding the pulsar position (+) had sufficient brightness temperature ($> 12\mathrm{K}(T_b)$) that a spectral index was calculated (see text).

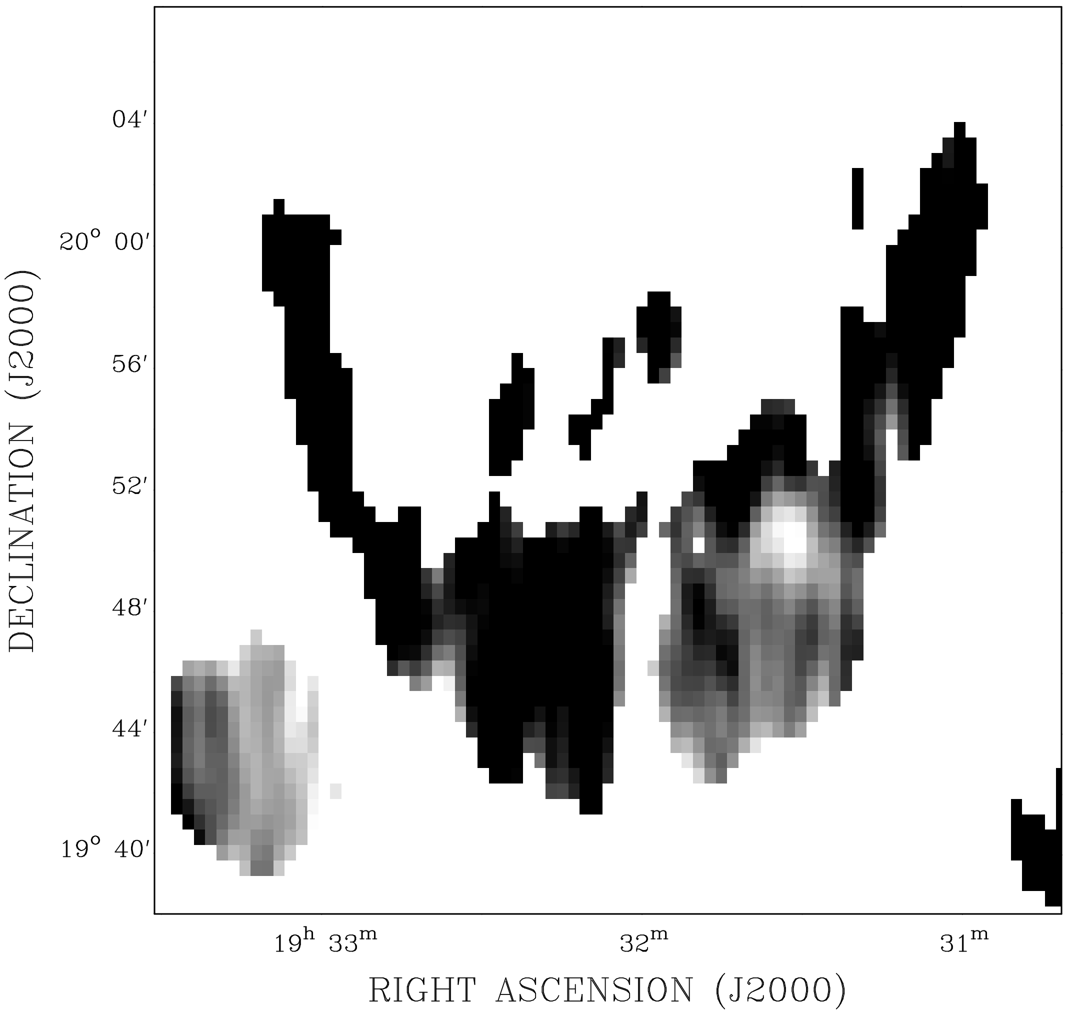

Figure 4.6: **Spectral Index Map of Casper's Smile**
Not all of the smile revealed a nonthermal spectral index. One large section in particular shows a spectral index that could be thermal. As for the spectral index map of the eyes, spectral indices less than 1.7 appear white, while those greater than 2.2 (nonthermal) are black.

nonthermal source. Although $\alpha < -0.1$ rules out thermal sources, $\alpha > -0.1$ does not rule out nonthermal sources.

4.3 Analysis of the IRAS Data

More than any other wavelength regime, the IR traces out the presence of dust in the ISM. Dust is heated by higher energy photons and re-radiates the energy in the IR. About one third of SNR show appreciable emission in the IR (Arendt, 1989). Saken *et al.* (1992) report clear IR emission from 35 of 161 known remnants. However, they note that their detections are highest toward the Galactic anticentre where confusion due to bright emission from the dust in the Galactic plane is minimized. Since Casper is located in the thick of the Galactic plane, its emission could be indiscernible as such. However, IR data were examined to see if anything more could be learned about the region.

While IR observations can provide an aid to the identification of SNR, they are insufficient to do so alone. HII regions and compact planetary nebula share characteristics with SNR in this regime, making classification by IR emission alone impossible (Saken *et al.*, 1992). S89 note that some old remnants may be weak in radio, optical and X-ray emissions due to low shock velocities, yet be extremely bright in the IR. However, Arendt notes that faint radio remnants (eg. 3C 58, G152.2-1.2, G261.9+5.5) have not been detected in the IR (1989).

The ratio of $60\mu/100\mu$ IRAS maps is often used as an indirect indictor of dust and temperature. Objects of higher temperature will have higher flux densities at 60μ than at 100μ. Also, ratios of IR to radio flux densities are a means of distinguishing

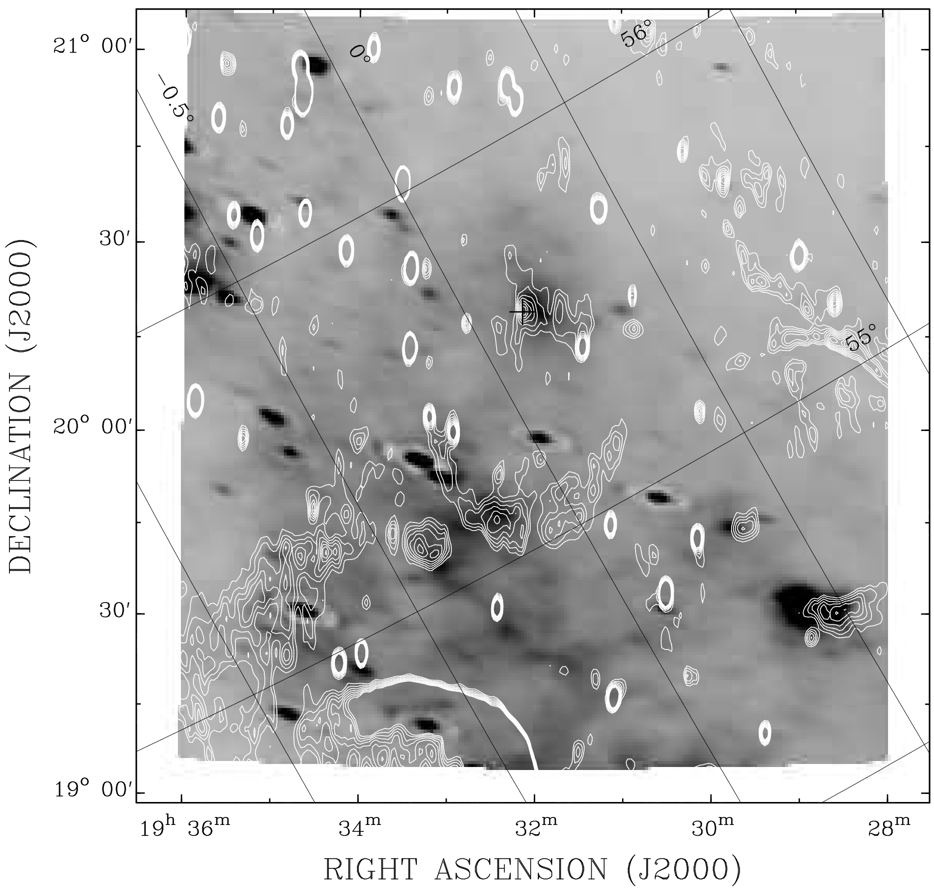

Figure 4.7: **Infrared versus Radio Emission in Casper**
The greyscale shows the distribution of infrared emission at 60μ. Black indicates emission greater than 150MJy/sr, while white indicates emission below zero. The overlain contours at 327MHz have values: 10, 15, 20, 30, 40, 50, 70, 110K(T_b). Note that there is a source of IRAS emission coincident with the eyes in the radio; however, the smile has no such counterpart, containing only a somewhat compact IR source near the bottom of the smile. Some IR point sources were subtracted from the maps for the determination of flux densities using polygons.

between HII regions and SNR. Figure 4.7 compares the distribution of IR emission at 60μ to the radio emission at 327MHz.

4.3.1 IRAS Colour Ratios

Ratios of IRAS $60\mu/100\mu$ are called IRAS colour maps, and the values of this ratio are indicators of dust presence and temperature variation. The IRAS 60μ and 100μ images had different beam sizes (see Table 3.4). Thus, it was necessary to degrade the resolution of the 60μ image to equal that of the 100μ image by convolution before a ratio map could be made.

Once both maps had the same resolution, background subtractions were performed on each based on values near the edges of the maps. The uniform background of these maps made this possible and saved the need for performing separate background subtractions for the eyes and smile of Casper.

As for the radio spectral indices, the mean values for the IRAS colours over the regions of Casper have been measured using integrated flux densities. The colour maps were examined to reveal how the ratio varied pixel to pixel.

Integrations at IRAS wavelengths were performed using the same polygons as those of the radio data. This enabled comparisons of the average flux densities of the regions. Since the polygons were generated with primary reference to the radio morphologies in the region, *they do not denote distinct regions of IRAS emission.* The exception is the region of Casper's eyes, where there is a source which stands out above the Galactic background (see Figure 4.7). In the interests of determining the flux density of that region, one new set of polygons was created to fit that source specifically ("IRAS source").

Table 4.5: **Integrated IRAS Flux Densities**

Region	# polygons	$S_{60\mu}$ (Jy)	$S_{100\mu}$ (Jy)	$S_{60\mu}/S_{100\mu}$
left eye	13	60 ± 15	82 ± 22	0.73 ± 0.3
right eye	11	9 ± 4	18 ± 7	0.50 ± 0.4
smile	14	152 ± 27	500 ± 101	0.3 ± 0.1
eyes	7	460 ± 52	584 ± 116	0.8 ± 0.2
IRAS source at eyes	8	233 ± 19	370 ± 38	0.63 ± 0.1
Casper	12	759 ± 78	1538 ± 160	0.5 ± 0.1

The flux densities obtained by the polygon integrations are shown in Table 4.5. As for the radio polygons, the errors quoted are the standard deviations of the averaged polygons. The large errors on the individual eyes are indicative of the fact that these objects were not distinct in the IRAS images. This means that the background estimates were extremely sensitive to the different polygons. The smaller errors on the combined eyes and the polygons fitted specifically to the IRAS source are indicative of the fact that the backgrounds were fit much better for these.

The ratio images in Figure 4.8 do show variations in the dust temperature in the eye region. The presence of dust as well as that of ionized gas traced by the 1420MHz continuum emission lend more support to the proposal that the radio source G55.6+0.7 is an HII region. There is no distinct emission from the smile in either the 60μ or the 100μ images. However, there is a small source contained in the polygon which contributes flux density in that series of polygons. This source may or may not be related to the radio smile.

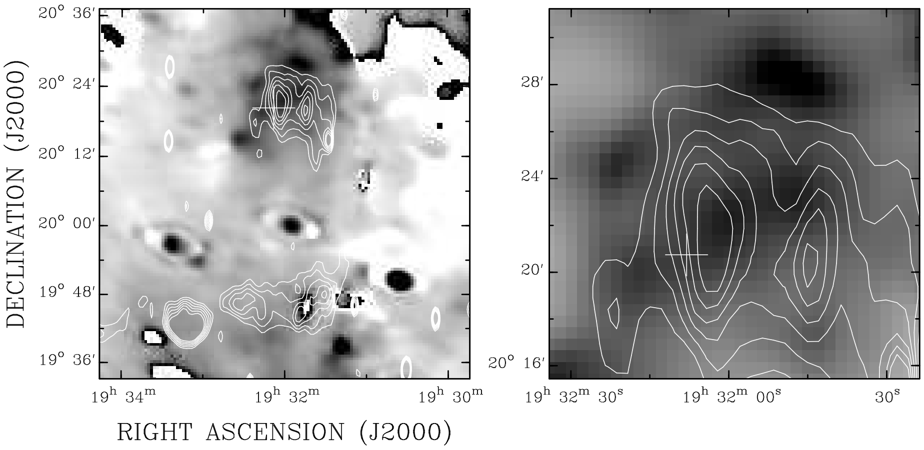

Figure 4.8: **IRAS Colour Map of Casper**
The map on the left shows the IRAS colour map for all of Casper; that on the right shows a closeup of the northern region, where IRAS emission is noted in the individual 60μ and 100μ maps. The greyscale limits are zero (white) and 0.8 (black). Higher ratios indicate regions of higher temperatures. The 1420MHz contours are overlain with values of 11.6K(T_b) to 13.6K(T_b) in increments of 0.4K(T_b). The radio continuum is an indicator of the presence of ionized hydrogen and therefore of HII regions.

4.3.2 IR/Radio Ratios

Ratios of IRAS to radio flux densities were also calculated. The majority of SNR exhibit a 60μ/1GHz ratio less than 100 while HII regions typically have ratios of several hundred (Wallace, 1991). For ratios of 60μ/327MHz, Taylor *et al.* (1996) have designated values below 200 to be indications of nonthermal sources.

Table 4.6: **IR/Radio Integrated Density Ratios**

Region	$S_{60\mu}/S_{1\mathrm{GHz}}$	$S_{60\mu}/S_{327\mathrm{MHz}}$
left eye	763 ± 3547	1063 ± 361
right eye	240 ± 2292	237 ± 155
smile	252 ± 103	155 ± 53
eyes	399 ± 72	503 ± 121
Casper	314 ± 56	275 ± 60

Taylor *et al.* (1992) used a $60\mu/1$GHz ratio of 100 to discriminate between SNR and HII regions, where SNR had ratios below 100. Close inspection of an analysis done by Wallace (1991) shows that the boundary is not sharp. Using HII regions of Lockman (1989), Wallace's data show that the ratio for known HII regions ranges from 0 to 900, with a concentration between 300 and 800. A similar analysis done with data from Green (1988) and Arendt (1989) revealed a strong peak in SNR below 100, although values up to 300 were obtained.

Based on the values of Table 4.6, it is evident that the $60\mu/1$GHz ratios for the individual eyes are meaningless, due to the large errors in extrapolating the 1GHz flux densities. The smile does have a value that is consistent with the range of values calculated for SNR by Wallace (1991), but it is also consistent with the range for HII regions. Casper's value is also ambiguous. The values obtained for the eyes are consistent with the range for HII regions in the same work.

The ratios obtained for the $60\mu/327$MHz data are more informative. Taylor *et al.*'s (1996) cutoff for nonthermal emission is a ratio below 200, which is consistent again with that of the smile. The right eye also has a ratio which is suggestive of a nonthermal source, given the errors. However, the difficulty with the background estimation of the right eye in the IRAS data has already been noted. The data for the other three regions do not suggest the presence of nonthermal emission.

Although the IRAS data on their own cannot reveal the nature of the objects of Casper, used in conjunction with the radio data, the IR images have been examined in an attempt to discriminate between possible sources of IR emission. The IRAS colour maps reveal the presence of dust and ionized gas at the position of the eyes. Additionally, the $60\mu/1$GHz and $60\mu/327$MHz ratios for the eyes are consistent with those of HII regions, and inconsistent with those of SNR.

The IRAS colour map does not reveal any obvious hot dust coincident with the smile which could indicate the presence of a shock. The $60\mu/1$GHz ratio for that region lies within the bounds for both HII regions and SNR as reported by Wallace (1991). The $60\mu/327$MHz ratio is less ambiguous, suggesting that the smile is an SNR.

Analyses of the radio continuum and IRAS data have revealed that the northern part of Casper does not have a spectral index indicative of a nonthermal object, but that of an optically-thin HII region. Its appearance in the IRAS colour map and the IR/radio ratios are also consistent with those of an HII region. On the other hand, the southern region of Casper has a nonthermal index equal to the average values for shell-type SNR and an IR/radio ratio suggestive of an SNR.

Chapter 5

The SNR G55.0+0.3

The analysis of the preceding chapter reveals that there is no evidence of nonthermal emission in the northern portion (eyes) of Casper. Furthermore, the IRAS data are consistent with that expected for an HII region. Thus, the conclusions of Reich *et al.* (1986) are supported by this work. Since the object of this search is SNR, the discussion will now focus on the southern smile region.

It is no longer assumed that all shells visible in radio emission are SNR. Other objects have been observed which share this morphology, namely stellar wind bubbles and so-called superbubbles. The former objects are the product of the powerful winds of early-type stars (classes O and B). These are the same massive stars which end their lives as SNe. They are now known to have strong influence on the structure of the ISM and can inject as much energy to the ISM during their lifetimes via their winds as they do during their deaths as SNe (Kulkarni and Heiles, 1988). The holes, called bubbles, blown in the ISM are of lower density than the ISM and shells form where the winds interact with the ISM. Superbubbles are a similar phenomenon, but on a much larger scale. These irregular bubbles are believed to be blown in the ISM by clusters of SNe. Since stars are born in clusters, and the progenitors of SNe typically evolve very quickly, SNe and SNR "clusters" should not be uncommon.

The morphology of Casper's smile (a complete half-shell) suggests that the shell has been formed by a single object (i.e. an injection of energy from a single location), which does not support the theory of a superbubble. Also, supershells in the

Magellanic Clouds have not been identified as nonthermal emitters in the Parkes radio survey, nor is there any evidence of nonthermal emission from the over 100 supershells identified in M31 (Wendker, private communication).

Based on its radio morphology alone, Casper's smile could be either an SNR or the result of the stellar wind of a massive star. The discrimination of the two objects can be done using the spectral index. The known Galactic wind bubbles (and superbubbles for that matter) which have been identified do not show signs of nonthermal emission (Wendker, private communication).

In summary, based on its morphology (an extended radio shell) and its spectral index, the smile is concluded to be a shell-type SNR. Based on this interpretation, the designation of G55.0+0.3 will be used hereafter. This position is roughly the centre of the half-shell of radio emission.

5.1 Surface Brightness of G55.0+0.3

The surface brightness of SNR is assumed to fade over time as an SNR expands. Older remnants are thought to be larger and fainter than young ones. The surface brightness, Σ, is a measure of the average flux density per unit solid angle of the remnant:

$$\Sigma_\nu = \frac{S_\nu}{\Omega} \tag{5.1}$$

where Ω is measured in steradians. S_ν is the total flux density of the remnant (usually at 1GHz). Note that it is a quantity which is independent of distance! Surface brightness at 1GHz has been catalogued for known remnants by Green (1995).

For G55.0+0.3, $S_{1\mathrm{GHz}} = 0.60 \pm 0.14$Jy. Based on its angular size (discussed

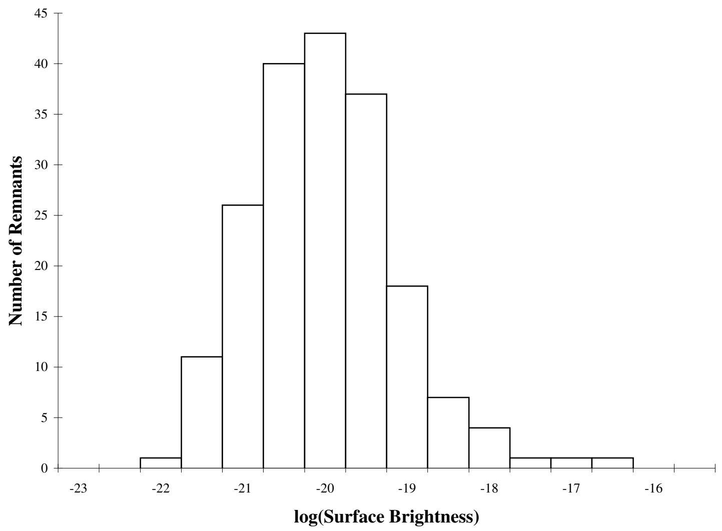

Figure 5.1: **Surface Brightnesses of Known SNR**
This histogram has been plotted using the information in Green's catalogue (1995). Were G55.0+0.3 plotted as well, it would be one of only two SNR with surface brightness on the order of 10^{-22}Jy/sr.

below), this SNR yields a surface brightness of $(9.8 \pm 2.3) \times 10^{-23}$ W m^{-2} Hz^{-1} sr^{-1}. Figure 5.1 is a histogram showing all known remnants of known or estimated surface brightness as given in Green (1995). There is only one other remnant with so low a value, G156.2+5.7, which exhibits shell-type morphology in both the radio and X-ray regimes. That remnant has an angular size of $110'$.

The extremely low value of its surface brightness suggests that G55.0+0.3 is a highly evolved remnant.

5.2 The Importance of Distance Measurement

Classification of astrophysical objects is only the first step to understanding their natures. Their physical properties (eg. age, size, mass) must be determined to construct and test models which can explain their origin and evolution. The same is true for

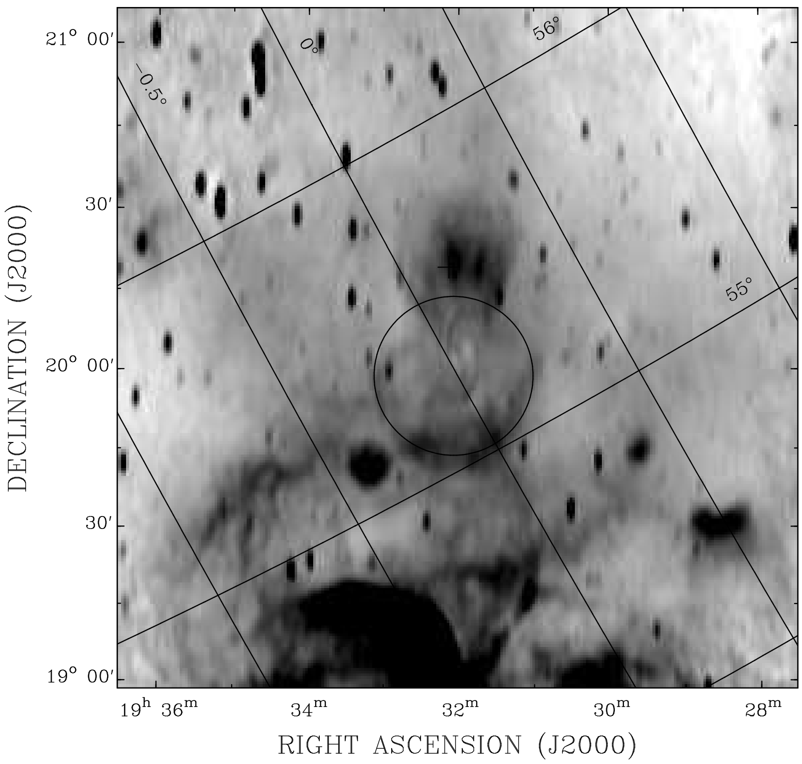

Figure 5.2: **Defining the Size of SNR G55.0+0.3**
A circle of diameter 30′ fits Casper's shell well. The greyscales of this 1420MHz image are 9.5K(T_b)(white) to 13K(T_b) (black).

SNR; however, with SNR, the origins are believed to be understood. Observations serve to test these theories.

5.2.1 Size

G55.0+0.3 is semi-circular in shape in the radio; therefore the size of the radio shell was estimated by a circle which roughly fit its radio morphology (see Figure 5.2). The angular radius of the shell is thus estimated to be 15′. The full circle covers a solid angle of 6×10^{-5}sr on the sky.

The physical size of objects cannot be estimated unless a distance is known (or in astronomy, more likely estimated with several assumptions!). However, if one has a distance estimate, then the physical dimensions can be estimated, since, for objects of small angular size, the angular size is simply a ratio of diameter to distance.

The radius in parsecs (R) is given by the relation:

$$R = 0.147D \cdot \theta \tag{5.2}$$

where D is the distance to the object in kiloparsecs, and θ is the angular diameter in arcminutes. From the angular size of G55.0+0.3, the radius is

$$R_G = 4.4D \quad \text{(pc)}. \tag{5.3}$$

In the remainder of this chapter, those equations specific to G55.0+0.3 will be indicated by the "G" subscript.

5.2.2 Swept-up Mass

Once a remnant has passed the free expansion stage, it has swept up a mass of the ISM that is comparable to the original mass of the ejecta. Beyond these times, the mass of the ejecta becomes negligible. The swept-up mass is then determined by the volume of the ISM that has been "swept-up" and what its density is. Since mass is simply density times volume, it is easily shown that, at such times,

$$M_{sw} = 0.1 n_0 R^3 \quad (M_\odot) \tag{5.4}$$

where M_{sw} is in units of solar masses ($M_\odot = 2 \times 10^{33}$ g), n_0 is in cm^{-3} and R is in parsecs. Substituting for R, equation 5.3 yields a specific mass dependence on D:

$$M_G = 8.5 n_0 D^3 \quad (M_\odot). \tag{5.5}$$

5.2.3 Age

It is not possible to write down a single expression for the age, since its estimation is dependent on the phase of the SNR. However, the equations of §1.3 can be used to express the age of G55.0+0.3 for each phase.

Based on equations 1.22 and 5.3, the age of G55.0+0.3 in Phase I (free expansion) would be given by the expression:

$$t_G^I = (4.3 \times 10^6) D/v_0 \quad \text{(yr)} \tag{5.6}$$

where v_0 is the initial velocity of the ejecta in km/s.

The free expansion phase lasts until several stellar masses have been swept up. A massive O star could produce an ejecta with a mass of $\sim 10 M_\odot$. Assuming the free expansion phase ends when a mass equal to that of the ejecta has been swept up, equation 5.5 predicts that G55.0+0.3's distance would be $\leq$ 1kpc for an ISM density of 1cm^{-3}. For an initial expansion velocity of 10,000km/s, this occurs at an age of $\sim$450yr.

The low Σ argues against G55.0+0.3 being such a young SNR; therefore, the remnant is likely to be in Phase II (adiabatic expansion) or Phase III (radiative expansion) and at a distance greater than the $\sim$1kpc limit for the free expansion phase.

During the adiabatic phase, the equations 1.23 and 5.3 predict an age of:

$$t_G^{II} = (7.3 \times 10^2) n_0^{1/2} E_{51}^{-1/2} D^{5/2} \quad \text{(yr)}. \tag{5.7}$$

A similar exercise for the radiative phase based on equations 1.25 and 5.3 produces

$$t_G^{III} = (2.1 \times 10^2) n_0^{0.857} E_{51}^{-0.757} D^{3.3} \quad \text{(yr)} \tag{5.8}$$

if the metallicity in equation 1.25 is assumed to be solar (unity).

Assuming that G55.0+0.3 is just past the free expansion phase, the lower limits on D, R and age are $\sim$1kpc, 4.8pc and 450yr for the assumptions outlined above. Assuming a Galactic radius of 25kpc, the maximum distance an object of longitude 55° could have if it were Galactic is $\sim$30kpc. At this distance, G55.0+0.3 would have a radius of $\sim$128pc and an age greater than 5×10^6yr in either Phase II or III. These upper and lower bounds are not very tightly constrained! Thus, it is evident that a measure of distance is essential to the determination of the physical properties of G55.0+0.3.

5.3 Measuring Distances of SNR

The distances to most SNR are not well known since the difficulties involved in their measurement are considerable. Only those which are associating with another object of established distance (i.e. a pulsar or HII region) are reasonably reliable, such as CTB 80 which has been shown to be interacting with a pulsar (S89). However, the distance to the associated object may be no more certain. The methods of pulsar distance measurement have been scrutinized by Frail and Weisberg (1990), for example.

Another method of establishing SNR distances is the *kinematic method* which uses the rotation curve of the Galaxy to convert Doppler shifted velocities of neutral hydrogen to distances. It is based on the fact that all objects in the Galaxy are known to orbit about the Galactic centre. A "rotation curve" relates the rate of an object's circular velocity to its distance from the Galactic centre. The Doppler

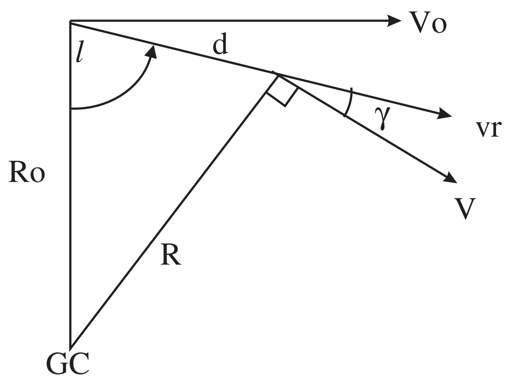

Figure 5.3: **Galactic Rotation Geometry**

shifted velocity measured at Earth is a result of the difference in relative velocities of objects at different distances from the Galactic centre. The uncertainty associated with the kinematic velocities due to the assumption of circular motion is on the order of 10% (Burton, 1988).

The situation is illustrated in Figure 5.3. R_0 and R are the distances of the Sun and that of the object of interest from the Galactic centre. V_0 and V are the corresponding linear velocities of the (assumed) circular orbits about the Galactic centre. The relative radial velocity between the objects, v_r, is therefore:

$$v_r = V \cos\gamma - V_0 \cos(90 - l) \tag{5.9}$$

where l is the Galactic longitude of the object. The sine law yields the relation

$$\frac{\sin l}{R} = \frac{\sin(90+\gamma)}{R_0} = \frac{\cos\gamma}{R_0}. \tag{5.10}$$

Substituting in equation 5.9 for $\cos\gamma$ yields:

$$v_r = R_0(\omega - \omega_0)\sin l \tag{5.11}$$

where ω is the angular rotation rate of the Galaxy at R (i.e. V/R).

From Figure 5.3, the distance from the Sun to the object, d, can be expressed as

$$R^2 = R_0^2 + d^2 - 2R_0 d\cos l \tag{5.12}$$

using the cosine law. Equations 5.11 and 5.12 can be combined to relate v_r and d, thereby providing a means of determining the distance to the object, if the Galactic rotation curve $V(R)$ is known:

$$R^2 = d^2 - \frac{2v_r \cot l}{\omega - \omega_0}d + \frac{v_r^2\csc^2 l}{(\omega - \omega_0)^2}. \tag{5.13}$$

In order to use the Galactic rotation curve to determine distances to other sources, the distance and linear velocity of the Sun with respect to the Galactic centre must be known (or assumed). The standards are currently $R_0 = 8.5$kpc and $V_0 = 220$km/s. These values have been used to determine the kinematic distances of the features of G55.0+0.3.

Velocities of interstellar gas are measured with respect to the Local Standard of Rest (LSR). The LSR is a dynamical reference system based upon the rotational dynamics of the Galaxy. This system is instantaneously centred upon the Sun, which is assumed to move in a circular orbit about the Galactic centre according to the standards given above. Deviations from the circular orbit are apparent in stars within the solar neighbourhood.

To establish distances to SNR using the rotation curve, one looks at the ISM in the direction of the SNR for evidence of an interaction. By imaging the neutral atomic hydrogen as a function of radial velocities in the direction of the SNR, features corresponding to the morphology seen in continuum can be observed in the gas. Since each channel represents a finite range of possible velocities, the detection of an object in an HI channel (or better still, a range of channels), places velocity and hence distance limits on the object.

5.3.1 Distance of G55.0+0.3 from HI Observations

Examination of the HI line maps was done to search for features corresponding to the shell structure of G55.0+0.3. Since the SNR will sweep up the ISM as it expands, it will create a void in the neutral atomic ISM. However, the presence of a void alone is not sufficient to establish a relation. A correlation between the continuum contours and the HI structure are essential to attribute a velocity to the object, since the HI interstellar medium contains plentiful voids.

The search was carried out by overlaying contours from continuum data, i.e. 327MHz and 1420MHz data, on each HI channel map. This ensured that features which resembled regions of heightened emission in the radio would be apparent in the HI. The average value of each HI channel was subtracted to create “bias-subtracted” maps which make comparison easier, since variations in average intensity across channels are removed.

The best case for HI correlation with G55.0+0.3’s continuum emission is a void located across nine channels, ranging in velocities from -39.6 to -52.8km/s (see Figure 5.4) and centred at -46.2km/s (see Figure 5.5). The central channel is singled out since it should yield the best estimate of the relative radial velocity of a spherically symmetric, expanding object. Using a Galactic rotation model as described in the

Table 5.1: **Kinematic Distances and Radii**

v_r (km/s)	D (kpc)	R (pc)
-46.2	14.0±0.6	62

previous section yielded a distance of 14kpc to the central channel. The distance of G55.0+0.3 from the Galactic centre would then be 11.4kpc, and its height above the Galactic plane, z, would be roughly 73pc.

From Figures 5.4 and 5.5, the crescent-shaped void is seen to persist through nine velocity channels, and the enlarged central channel shows that the morphologies of the outer shell edge in continuum to the southeast is reasonably matched in the HI (east is to the left on the maps). The fact that the continuum emission matches the HI central channel void best supports the notion that the void is related to the SNR. The continuum shell seems to have reached a void in the HI to the southwest, which could explain why that part of the shell did not appear distinctly nonthermal (recall Figure 4.6). Nonthermal emission is dependent on having an ambient medium with which the shock can collide. Variations in the ISM will then show up as variations in the levels of synchrotron emission.

The "empty" channels of the HI cube were examined for evidence of high velocity HI related to the SNR which could appear due to systematic velocities of the object itself, independent of the kinematic velocities within the cube which are due to the Galactic rotation. None was noted.

The kinematic distance of 14kpc in Table 5.1 infers a radius of 62pc for G55.0+0.3 from equation 5.3. This size is large, but not without precedent. One of the largest

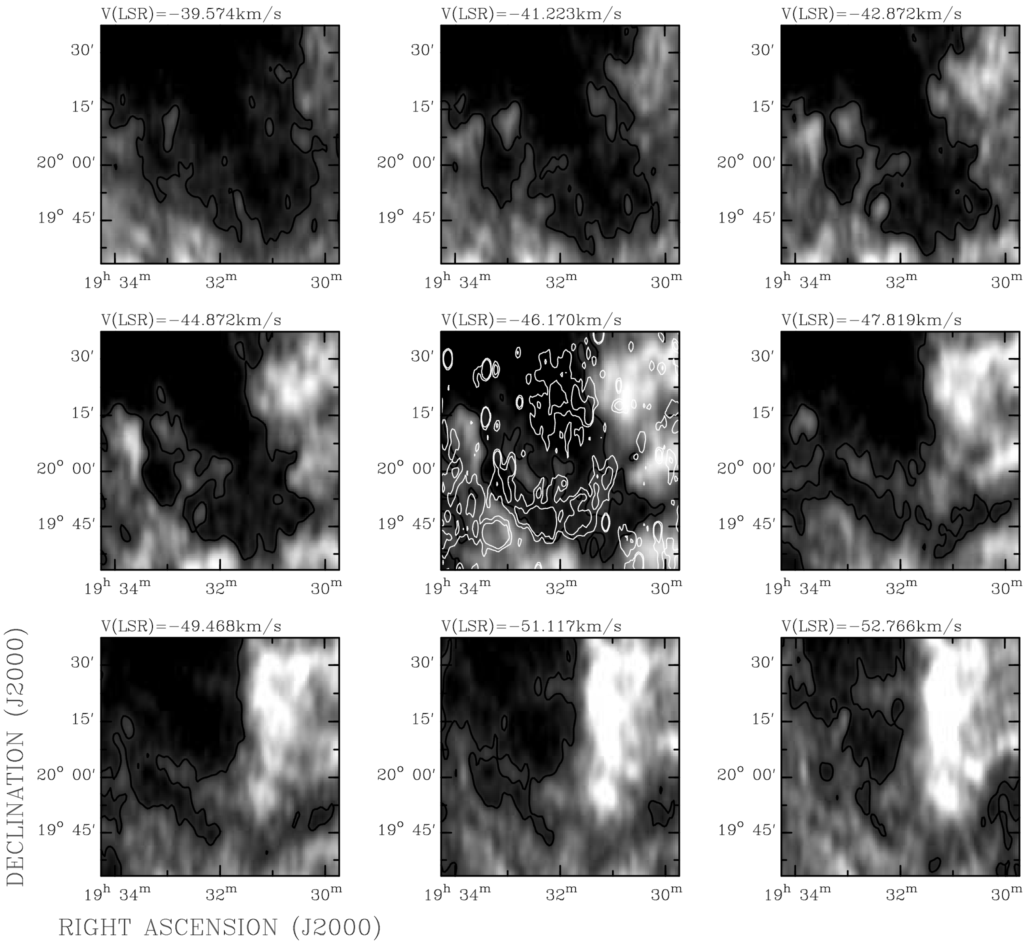

Figure 5.4: **HI Velocity Channels, -39.6 to -52.8km/s**

These bias subtracted maps have limits of -15K(T_b) (black) and 21K(T_b). The contours of the 327MHz overlay are 10 and 30K(T_b). A single black contour is included at -5K(T_b). The continuum contours were placed on only one image, since they tend to obscure the HI below. A larger image of the central channel is shown in Figure 5.5.

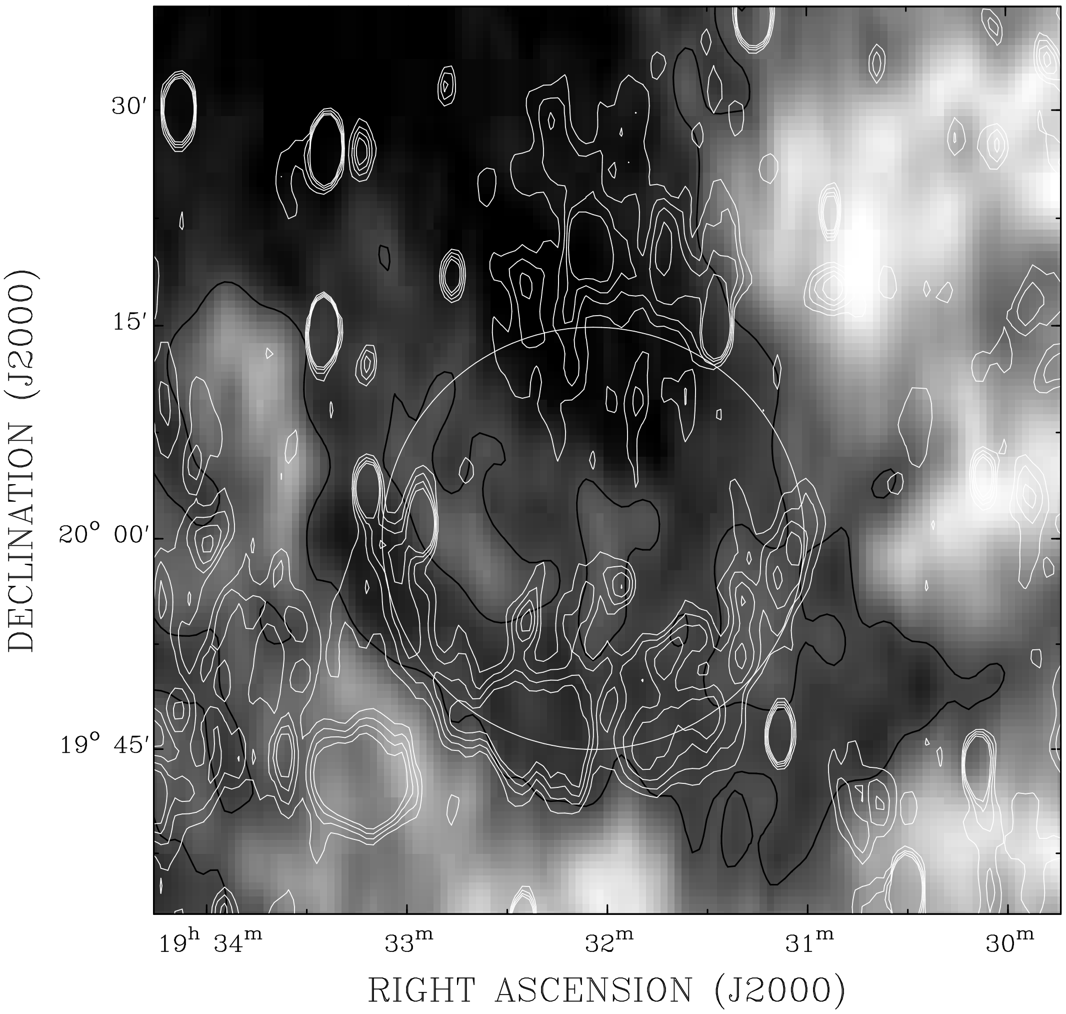

Figure 5.5: **Central HI map for V(LSR)=-46.2km/s**
The shell at 327MHz in white contours (5, 10, 15 and 20K(T_b)) is matched well by the HI greyscale void at -46.2km/s. Many of the variations in the continuum are echoed in the shell, especially to the southeast. The greyscale limits on the HI are 21K(T_b) (white) and -15K(T_b) (black). The single black contour in HI is placed at -5K(T_b).

Table 5.2: **Parameters for G55.0+0.3 for $D = 14$kpc**

n_0 cm^{-3}	M_{sw} $(M_\odot)$	t_{II} $(10^5\mathrm{yr})$	t_{III} $(10^5\mathrm{yr})$
1	2.3×10^4	5.4	13
0.1	2.3×10^3	1.7	1.8

known remnants is OA 184 (G166.2+2.5) which has an angular size of $90' \times 70'$ at a distance of 8kpc (Routledge *et al.*, 1986) which corresponds to an average radius of about 94pc. No distance estimate exists for the aforementioned low surface brightness remnant G156.2+5.7; however, placing it at the reasonable (but arbitrary) distance of 5kpc yields a radius of 81pc!

Table 5.2 contains calculated masses and ages for various ambient densities of the ISM. Based on these ages, the remnant is most likely highly evolved. Its large size and faintness is another indication that it is old. If the age is in fact $\sim 10^6$yr, this would be the oldest established age for an SNR.

5.3.2 Evolutionary Stage

The evolution models described in §1.3 can be used to set reasonable limits on how old and how large a shell can be at the transition times between phases. These calculations can be used to establish, for a given distance, the evolutionary phase of the SNR. The arguments previously presented suggest that G55.0+0.3 is in either Phase II or III of its evolution.

The time for the transition from the adiabatic to the snowplow phase of a shell-type SNR is given by equation 1.24. Assuming $E_{51} = 1$ and a solar metallicity

Table 5.3: **Theoretical Transition Ages and Radii**

n_0 (cm^{-3})	t_{rad} (10^5yr)	R_{rad} (pc)	$t_{dis}(m=1)$ (10^5yr)	$R_{dis}(m=1)$ (pc)
1	0.13	14.0	28.6	76.3
0.1	0.21	37.6	67.0	178

abundance ($\xi_m = 1$), the time at which the remnant will enter the radiative phase is

$$t_{rad} = (1.33 \times 10^4) n_0^{-4/7} \quad (\mathrm{yr}) \tag{5.14}$$

and the shell's radius at that time is given by

$$R_{rad} = (14.0) n_0^{-3/7} \quad (\mathrm{pc}). \tag{5.15}$$

The maximum time in which a remnant can remain in adiabatic expansion and the maximum size it can reach in that phase are listed for two values of the ambient ISM density in Table 5.3.

The radiative lifetime of a remnant ends when the remnant merges with the surrounding ISM. This time can also be easily estimated. The time of the merger (dissipation) will be here defined to be that at which the shock has slowed to 8km/s, the speed of macroscopic turbulence in the ISM (Spitzer, 1978). At this time, the remnant's structure is disrupted by the ISM. The expression for the radius of the SNR in the radiative phase is given by equation 1.25. Thus, differentiating equation 1.25 with respect to time and setting the result equal to the turbulence speed yields the merger times of the remnant and ISM.

The assumed value for the ambient density of the ISM is a quantity about which there is much debate, thus it is wisest again to leave it as a variable. Making the same assumptions as for the adiabatic case yields an expression for the time at which the remnant starts to dissipate:

$$t_{dis} = (28.6 \times 10^5) n_0^{-0.37} m^{-1.43} \quad \text{(yr)}, \tag{5.16}$$

at a shell radius of

$$R_{dis} = (76.3) n_0^{-0.368} m^{-0.429} \quad \text{(pc)} \tag{5.17}$$

where m is the local sound speed in units of 8km/s (8km/s = 0.8pc/10^5yr). Table 5.3 evaluates the merger time for two values of n_0. The variation in values of Table 5.3 emphasizes how dependent SNR evolution is on the characteristics of the surrounding ISM. Note that the ages in Table 5.2 are all larger than t_{rad}; therefore, if the remnant is at 14kpc, it is currently in the radiative expansion phase.

5.4 An Association Based Estimate of Age

The presence of the pulsar near the SNR has not yet been addressed in this discussion. However, the proximity of J1932+2020 to G55.0+0.3 begs the question as to whether or not these objects are related. The question is not an easy one to answer, but several factors establish the association as reasonable.

Gaensler and Johnston (1995a,b) identified possible pulsar/SNR associations based on a quantity β, which was the ratio of the angular distance of the pulsar to the average angular radius of the remnant. Associations were considered possible for $\beta < 2$.

Using the position of the pulsar J1932+2020 in Table 1.3 and a blast position of 19:32:4.2 in RA and 19:58:59 in Dec (the centre of the circle in Figure 5.2 and 5.5), the pulsar's current position is $\sim 21.8'$ from the position of the SN which created G55.0+0.3. This yields a β value of 1.5.

As pointed out in §1.4, $\beta \leq 2$ is a necessary but not sufficient criterion for an association. Coincidence of distance and age must also be established between the pulsar and the remnant.

§1.5.1 contains two distance estimates for J1932+2020. From the dispersion measure, the distance has been estimated to be approximately 9kpc, with an uncertainty of 25% (Taylor and Cordes, 1993). Determinations of lower and upper limits on the kinematic distance from HI absorption spectra yielded limits of 4.8±1.8kpc and 14.9±0.9kpc, respectively (Frail and Weisberg, 1990). Only the kinematic method has been used to estimate the distance to the SNR; however, the inferred distance of 14kpc is consistent with the kinematic distance estimate to the pulsar and reasonably close to the DM distance given the uncertainties in both values.

The characteristic age (see equation 1.4) of pulsars is independent of their distance. As calculated in §1.5.1, the characteristic age of J1932+2020 is 1.1×10^6yr. For a distance of 14kpc and $n_0 = 1\text{cm}^{-3}$, G55.0+0.3 is in the snowplow phase, and its age is 1.3×10^6yr, a very good match to that of the pulsar (Table 5.2).

Many associations which have been proposed in the literature have been questioned due to the high velocities needed by the pulsars to have reached their positions with respect to the remnants. Based on equation 1.30, the velocity required by the pulsar can be calculated. The age of G55.0+0.3 requires pulsar velocities of 54km/s and 269km/s for ambient ISM densities of 1cm^{-3} and 0.1cm^{-3}. Cordes (1986) derives the mean velocity of pulsars to be 100km/s, using measurements of Harrison and Lyne (1993). Lyne and Lorimer (1994) have estimated the mean pulsar birth velocity to be 450$\pm$90km/s. Thus, the velocities required by J1932+2020 are not excessive. It should be pointed out that there has been no measure of proper motion for this pulsar. Its observation would provide a direct measure of the pulsar's velocity and a further test of the validity of the proposed association.

The compatibility of the distance and age estimates of the pulsar and the remnant provides evidence that the two are associated and were formed by the same SN event. The association would firmly establish the age of the SNR to be $> 10^6$yr, the oldest known age for such an object.

This then has implications for the radiative lifetimes of SNR which have been previously thought to be much smaller. Current thinking is that SNR should cease to be observable about the age of 1-2$\times 10^5$yr. If associated with the pulsar, G55.0+0.3 is older than this proposed limit. If so, the SNR could just one member of a population of faint, old remnants not currently detectable. It will be interesting to see whether the next generation of radio telescopes detects more such remnants.

Finally, as discussed in §1.4, most of the associations which have been proposed are for the youngest known pulsars. Only one, CTB 80, has an age on the order of 10^5yr. Most are $\sim$20,000yr. This is not surprising, since most have been found by focussed searches for associated SNR about young pulsars. This association is the oldest ever proposed and suggests that targeted searches should not be restricted by pulsars' characteristic ages.

Chapter 6

Summary and Future Work

Within this thesis, a new, ancient SNR, G55.0+0.3, has been identified based on new 1420MHz data of comparable resolution to the 327MHz data which were the catalysts for this work. These data conclusively identify G55.0+0.3 to be a source of nonthermal emission currently consistent only with a shell-type SNR. The low IRAS flux density present in the region supports this conclusion.

In addition, the argument that the remnant is associated with the nearby pulsar, J1932+2020, is compelling. The remnant and pulsar fit the criterion of an association as described by Gaensler and Johnston (1995b) and have comparable estimates of age (for an assumed ambient density of $1\mathrm{cm}^{-3}$) and distance. If valid, the association would establish the age of the SNR to be greater than one million years.

The results of this thesis could call into question two current beliefs, both related to the observable lifetime of SNR. The conventional wisdom in the literature is that SNR ought not be observable past the age of 1-2 $\times 10^5$yr; in some cases, much lower limits are proposed. G55.0+0.3 appears to be a more evolved SNR, currently undergoing radiative expansion.

G55.0+0.3 is also one of the faintest SNR known. If a significant fraction of SNR in fact survive to 10^6yr, further imaging of the Galactic plane with high surface brightness sensitivity and high angular resolution should reveal more ancient SNRs.

It has been the practice to treat young pulsars as the best candidates for targeted searches for the associated SNR. Thus, the current associations are young. The oldest proposed is CTB 80 with an age of 10^5yr, but the more typical age is ~60,000yr. The age of an association of G55.0+0.3 and J1932+2020 would imply that there may be many associations of intermediate age which simply have not been targeted for searches in the past.

This thesis has answered the question as to whether or not there is an SNR within the region denoted as Casper; however, this discovery makes further investigation of the region imperative. The unique age estimates of the SNR make it especially worthy of deeper study. For instance, the distance derived independently of the pulsar is prone to large uncertainty.

There exist no surveys of carbon monoxide (CO) which include Casper and have resolution better than half a degree. Observations of the molecular composition about G55.0+0.3 is warranted, since the presence of molecular clouds in the region could explain why so ancient a remnant can be seen so near the Galactic plane. Dense molecular clouds would both decelerate the shocks created by expanding ejecta and create a shell of clumpy appearance, as has been observed for this SNR.

In order to obtain information about the molecular composition about G55.0+0.3, plans are afoot to submit an observing proposal to Five Colleges Radio Astrophysical Observatory to obtain maps of this region in CO. It is unfortunate that a current survey underway there stops short of G55.0+0.3's location.

As mentioned in the text of the previous chapter, a measurement of the proper motion of the pulsar could definitively settle the question about the presence of an SNR/pulsar association. The pulsar's velocity estimate of 54km/s and distance of 14kpc imply that its angular motion is ~0.8 milliarcseconds/yr. The best instrument to measure such a proper motion is the Very Long Baseline Array (VLBA) which has a resolution of a few milliarcseconds. Measurements over a period of several years would reveal the motion of the pulsar with respect to background sources. A positive result from such an observation would confirm G55.0+0.3 to be the oldest known SNR.

Bibliography

[1] Altenhoff, W. J., Downes, D., Goad, L., Maxwell, A., Rinehart, R. 1970, *Astron. Astrophys. Suppl. Ser.* **1**, 319.

[2] Altenhoff, W., Mezger, P. G., Wendker, H., Westerhout, G. 1960, *Veröff. Sternwärte, Bonn* **59**, 48.

[3] Arendt, R. G. 1989, *Astrophys. J. Suppl. Ser.* **70**, 181.

[4] Arzoumanian, Z., Nice, D. J., Taylor, J. H. 1994, *Astrophys. J.* **422**, 671.

[5] Aumann, H. H., Fowler, J. W., Melnyk, M. 1990. *Astron. J.* **99**, 1674.

[6] Baade, W., Zwicky, F. 1934a, *Proc. Natl. Acad. Sci. USA* **20**, 254, 259.

[7] Baade, W., Zwicky, F. 1934b. *Phys. Rev.* **46**, 76.

[8] Backer, D. C. 1988 in *Galactic and Extragalactic Radio Astronomy*, eds. G. L. Vershuur, K. I. Kellerman, (New York: Springer-Verlag), Chapter 11.

[9] Bhattacharya, D. 1990, *J. Astrophys. Astr.* **11**, 125

[10] Braun, R., Goss, W. M., Lyne, A. G. 1989, *Astrophys. J.* **340**, 355.

[11] Burton, W. B. 1988 in *Galactic and Extragalactic Radio Astronomy*, ed. G. L. Vershuur, K. I. Kellerman, (New York: Springer-Verlag), Chapter 7.

[12] Cao, Y., Prince, T. A., Tereby, S., Beichman, C. A. 1996, *Publ. Astron. Soc. Pacific* **108**, 535.

[13] Caraveo, P. A. 1995, in *The Lives of Neutron Stars*, eds. M. A. Alpar *et al.*, (Netherlands : Kluwer Academic Publishers).

[14] Caswell, J. L., Kesteven, M. J., Komesaroff, M. M., Haynes, R., Milne, D. K., Stewart, R. T., Wilson, S. G. 1987, *Monthly Notices Roy. Astr. Soc.* **225**, 329.

[15] Caswell, J. L., Kesteven, M. J., Stewart, R. T., Milne, D. K., Haynes, R. 1992, *Astrophys. J.* **399**, L151.

[16] Cioffi, D. F., McKee, C. F., Bertschinger, E. 1988, *Astrophys. J.* **334**, 252.

[17] Condon, J. J., Broderick, J. J., Seielstad, G. A. 1989, *Astron. J.* **97**, 1064.

[18] Cordes, J. M. 1986, *Astrophys. J.* **311**, 183.

[19] Crovisier, J. 1974, *Astron. Astrophys.* **37**, 189.

[20] Dombrovski, V. A. 1954, *Dokl. Akad. Nauk. S. S. S. R.* **94**, 1021.

[21] Fich, M., Tereby, S. 1996, *Astrophys. J.* , *in press.*

[22] Frail, D. A., Goss, W. M. and Whiteoak, J. B. Z., 1994a, *Astrophys. J.* **437**, 781.

[23] Frail, D. A., Kassim, N. E., Weiler, K. W., 1994b, *Astron. J.* **107**, 1120.

[24] Frail, D. A., Weisberg, J. M. 1990, *Astron. J.* **100**, 743.

[25] Frail, D. A., Cordes, J. M., Hankins, T. H., Weisberg, J. M. 1991, *Astrophys. J.* **382**, 168.

[26] Fürst, E., Reich. W., Sofue, Y., 1987, *Astron. Astrophys. Suppl. Ser.* **71**, 63.

[27] Gaensler, B.M. and Johnston, S., 1995a, *Monthly Notices Roy. Astr. Soc.* **275**, L73.

[28] Gaensler, B.M. and Johnston, S., 1995b, *Monthly Notices Roy. Astr. Soc.* **277**, 1243.

[29] Ginzburg, V. L. 1953, *Usp. Fiz. Nauk.* **51**, 343.

[30] Goldreich, P., Julian, W. H. 1969, *Astrophys. J.* **157**, 869.

[31] Gordon. 1954, *Dokl. Akad. Nauk. S. S. S. R.* **94**, 413.
148, 3.

[32] Green, D. 1988, *Ap. Space Sci.* **148**, 3.

[33] Green, D. 1995, *A Catalogue of Galactic Supernova Remnants* (Cambridge : Mullard Radio Astronomy Observatory).

[34] Gull, S. F. 1973, *Monthly Notices Roy. Astr. Soc.* **161**, 47.

[35] Gullahorn, G. E., Rankin, J. M. 1978, *Astron. J.* **83**, 1219.

[36] Hankins, T. H. 1987, *Astrophys. J.* **312**, 276.

[37] Harrison, P. A., Lyne, A. G. 1993, *Monthly Notices Roy. Astr. Soc.* **265**, 778.

[38] Haslam, C. G. T., Salter, C. J., Stoffel, H., Wilson, W. E. 1983, *Astron. Astrophys. Suppl. Ser.* **47**, 1.

[39] Helfand, D. J., Becker, R. H. 1984, *Nature* **307**, 215.

[40] Helfand, D. J., Becker, R. H. 1987, *Astrophys. J.* **314**, 203.

[41] Higgs, L. May, 1996, *private communication.*

[42] Hulse, R. A., Taylor, J. H. 1974, *Astrophys. J.* **191**, L59.

[43] Hulse, R. A., Taylor, J. H. 1975, *Astrophys. J.* **201**, L55.

[44] Janka, H. T., Müller, E. 1994, *Astron. Astrophys.* **290**, 496.

[45] Joint IRAS Science Working Group 1988, *Infrared Astronomical Satellite (IRAS) Catalogs and Atlases: Volume 3 (The Point Source Catalog Declination Range* $30° > \delta > 0°$*)* (NASA).

[46] Kassim, N., Weiler, K. 1990, *Nature* **343**, 146. *Astrophys. J. Suppl. Ser.* **68**, 715.

[47] Kellermann, K. J., Owen, F. N. 1988, in *Galactic and Extragalactic Radio Astronomy*, eds. G.L. Vershuur, K.I. Kellerman, (New York: Springer-Verlag), Chapter 13.

[48] Kulkarni, S. R., Clifton, T. C., Backer, D. C., Foster, R. S., Fruchter, A. S., Taylor, J. H. 1988, *Nature* **331**, 50.

[49] Kulkarni, S. R., Heiles, C. 1988, in *Galactic and Extragalactic Radio Astronomy*, eds. G. L. Vershuur, K. I. Kellerman, (New York: Springer-Verlag), Chapter 3.

[50] Large, M. I., Vaughan, A. E., Mills, B. Y. 1968, *Nature* **220**, 340.

[51] Lang, K. R. 1980, *Astrophysical Formulae* (New York : Springer-Verlag).

[52] Leahy, D. A., Wu, X. 1989, *Publ. Astron. Soc. Pacific* **101**, 607.

[53] Lorimer, D. R., Bailes, M., Dewey, R. J., Harrison, P. A. 1993, *Monthly Notices Roy. Astr. Soc.* **263**, 403.

[54] Lorimer, D. R., Yates, J. A., Lyne, A.G., Gould, D. M. 1995, *Monthly Notices Roy. Astr. Soc.* **273**, 411.

[55] Lyne, A. G. 1995, in *The Lives of Neutron Stars*, eds. M. A. Alpar *et al.*, (Netherlands : Kluwer Academic Publishers).

[56] Lyne, A. G., Anderson, B., Salter, C. J. 1982 *Monthly Notices Roy. Astr. Soc.* **201**, 503.

[57] Lyne, A. G., Lorimer, D. R. 1994, *Nature* **369**, 127.

[58] Lyne, A. G., Manchester, R. N., Taylor, J. H. 1985, *Monthly Notices Roy. Astr. Soc.* **213**, 613.

[59] Manchester, R. N., Taylor, J. H. 1991, *Astron. J.* **86**, 1953.

[60] McKee, C. F., Ostriker, J. P. 1977, *Astrophys. J.* **218**, 148.

[61] Minkowski, R. 1941, *Publ. Astron. Soc. Pacific* **53**, 224.

[62] Narayan, R., Schaudt, K. J. 1988, *Astrophys. J.* **325**, L43.

[63] Oört, J. H., Walraven, T. 1956, *Bull. Astron. Inst. Ned.* **12**, 285.

[64] Pacholczyk, A. G. 1970 *Radio Astrophysics*, (San Francisco : W.H. Freeman).

[65] Reich, W., Fürst, E., Steffer, P., Reif. K., Haslam, G. G. T. 1984, *Astron. Astrophys. Suppl. Ser.* **58**, 197.

[66] Reich, W., Fürst, E., Reich. P., Sofue, Y., Handa, T. 1986, *Astron. Astrophys.* **155**, 185.

[67] Reynolds, R.J., 1988, in *Galactic and Extragalactic Radio Astronomy*, eds. G. L. Vershuur, K. I. Kellerman, (New York : Springer Verlag), Chapter 10.

[68] Rohlfs, K. 1986, *Tools of Radio Astronomy*, (New York : Springer-Verlag).

[69] Routledge, D., Landecker, T. L., Vaneldik, J. F. 1988, *Monthly Notices Roy. Astr. Soc.* **221**, 809.

[70] Rybicki, G. B., Lightman, A. P. 1979, *Radiative Processes in Astrophysics*, (New York : Wiley).

[71] Saken, J. M., Fesen, R. A., Shull, J. M. 1992, *Astrophys. J. Suppl. Ser.* **81**, 715.

[72] Sedov, L. I. 1959, *Similarity and Dimensional Methods in Mechanics*, (New York : Academic Press).

[73] Shkovski, I. S. 1953, *Dokl. Akad. Nauk. S. S. .S. R.* **90**, 983.

[74] Shu, F. 1991, *The Physics of Astrophysics, Vol. I: Radiation*, (Mill Valley : University Science Books).

[75] Shull, J. M., Fesen, R. A., Saken, J. M. 1989, *Astrophys. J.* **346**, 860.

[76] Spitzer, L. Jr. 1978, *Physical Processes in the Interstellar Medium*, (New York : John Wiley and Sons, Inc.).

[77] Srinivasan, G., Bhattacharya, D., Dwarakanath, K. S. 1984, *J. Astrophys. Astr.* **5**, 403.

[78] Staelin, D. H., Reifenstein III, E. C. 1968, *Science* **162**, 1481.

[79] Steward, F. D., Harnden, F. R. 1982, *Astrophys. J.* **253**, L45.

[80] Steward, F. D., Harnden, F. R., Helfand, D. J. 1984, *Astrophys. J.* **287**, L19.

[81] Taummann, G. A., Löffler, W., Schroder, A. 1994, *Astrophys. J. Suppl. Ser.* **92**, 487.

[82] Taylor, J. H., Cordes, J. M. 1993, *Astrophys. J.* **411**, 674.

[83] Taylor, A. R., Goss, W. M., Coleman, P. H., van Leeuwan, J., Wallace, B. J. 1996, *in press.*

[84] Taylor, J. H., Stinebring, D. R. 1986 *Ann. Rev. Astron. Astrophys.* **24**, 285.

[85] Taylor, A. R., Wallace, B. J., Goss, W. M. 1992, *Astron. J.* **103**, 931.

[86] van der Bergh, S., McClure, R. D., Evans, R. 1987, *Astrophys. J.* **323**, 44.

[87] Wakatsuki, S., Hikita, A., Sato, N., Itoh, N. 1992, *Astrophys. J.* **392**, 628.

[88] Wallace, B. J. 1991, *Supernova Remnants in the Westerbork 327MHz Galactic Plane Survey* (University of Calgary : PhD thesis).

[89] Wallace, B. J. June, 1996, *private communication.*

[90] Wendker, H. J. 1968, *Astron. J.* **73**, 644.

[91] Wendker, H. J. July, 1996, *private communication.*

[92] Woltjer, L., 1972, *Ann. Rev. Astron. Astrophys.* **10**, 129.